An Examination of the Temporal and Spatial Evolution of a Small Permanent Focal Ischemic Lesion

A Thesis Submitted to the College of
Graduate Studies and Research
in Partial Fulfillment of the Requirements for the
Degree of Doctor of Philosophy
in the Department of Anatomy and Cell Biology
University of Saskatchewan
Saskatoon

By

Brenda Lynn Bartnik

Spring 2003

Permission to Use

In presenting this thesis in partial fulfillment of the requirements for a Postgraduate degree from the University of Saskatchewan, I agree that the Libraries of this University may make it freely available for inspection. I further agree that permission for copying of this thesis in any manner, in whole or in part, for scholarly purposes may be granted by the professor or professors who supervised my thesis work or, in their absence, by the Head of the Department or the Dean of the College in which my thesis work was done. It is understood that any copying or publication or use of this thesis or parts thereof for financial gain shall not be allowed without my written permission. It is also understood that due recognition shall be given to me and to the University of Saskatchewan in any scholarly use which may be made of any material in my thesis.

Requests for permission to copy or to make other use of material in this thesis in whole or part should be addressed to:

Head of the Department of Anatomy and Cell Biology
College of Medicine
107 Wiggins Road
University of Saskatchewan
Saskatoon, Saskatchewan
S7N 5E5

Abstract

The research reported here was designed to validate our hypothesis that non-invasive imaging could delineate the evolution of a small ischemic infarct. Furthermore, the alterations observed by MR were correlated to histological and inflammatory markers. Finally, intervention with a calcium buffering agent was hypothesized to prevent many of these changes.

The first part of this study investigated the development of a small focal cortical lesion produced as a result of a cortical devascularization injury. Diffusion-weighted images (DWI) were collected before injury and at 12, 24, 48 hours and 3, 5, 7 and 14 days after injury and apparent diffusion coefficient (ADC) maps were calculated from the DW images to quantify lesion development. As a second measure of injury, tissue morphology was analyzed using cresyl violet histochemistry. Results indicated a significant reduction in ADC values within the lesion cortex that first appeared at 12 hours after injury and then recovered to control levels by 14 days. ADC changes were also observed in the contralateral cortex. This type of injury also resulted in the progressive but relatively slow formation of a pan-necrotic infarct. Both astrocyte and microglia activation occurred early and were present in both hemispheres, however inflammatory cell infiltration was delayed until 48 hours after the injury. Many of these inflammatory cells were tumor necrosis factor α (TNF-α) and interferon γ (IFN-γ) immunoreactive. Overall, the quantitative and histological measures of this lesion were consistent with those

observed in ischemic injury. Moreover, we found DWI to be a sensitive measure of damage associated with a cortical devascularization injury.

The second part of this study used 2-aminophenol-N, N, O-triacetic acid acetoxymethyl ester (APTRA-AM) to determine the effectiveness of a calcium buffer in providing neuroprotection after a cortical devascularization injury. Animals were given two intravenous injections of either saline, DMSO, or APTRA-AM at 1 and 12 hours after injury. Animals were then imaged using a multiple b-value DWI sequence prior to injury and then at 12, 24, 48 hours, 3 and 7 days after injury. After 7 days the animals were sacrificed and correlative histological and immunocytochemical studies were done. Our results indicate that saline injection after injury resulted in a decrease in the ADC of the lesion cortex within the first 12 hours of injury, which then slowly returned to prescan levels. In contrast, the injection of either DMSO or APTRA-AM after injury resulted in no significant changes in the ADC within the lesion area. Histologically, both saline and DMSO injected animals had pan-necrotic infarcts with concomitant glial activation and inflammatory cell infiltration. APTRA-AM treated animals showed an 86% reduction in lesion area and no evidence of inflammatory cell infiltration. The results presented here clearly demonstrate the effectiveness of APTRA-AM in preventing neuronal cell death and the accompanying inflammatory response when administered post-injury, suggesting that this molecule may be an excellent candidate for future clinical neuroprotection studies.

Acknowledgements

I am very grateful to Dr. André Obenaus, my advisor and mentor. He has given me the opportunity to pursue science and has provided an environment in which to succeed.

I would also like to thank the members of my graduate committee, Drs. B. Juurlink, J. Thornhill, and C. Rasmussen, whose guidance was greatly appreciated. I am also grateful to Dr. U. Tuor, who has kindly agreed to serve as my external examiner. A special mention should be made to acknowledge the numerous helpful discussions I had with Dr. E. Kendall. Thank you.

I thank the many people in the Departments of Medical Imaging, Anatomy and Cell Biology and the Radiobiology Program at Loma Linda University who offered technical assistance, advice and friendship. Special thanks to Jennifer Hadley, Yusuf Bhagat, Shawnee Eidt, Gregg Parchomchuk, Shirley West, and Lora Benzatyan.

I would be remiss if I didn't acknowledge the love and support of my family and friends. Their patience, generosity and financial support (thanks Dad!) have made this trip a little easier. Thank you all. A special thank you to Sean (xoxop), Jen, Jacquie, Russ and Kristal.

In addition, I would like to acknowledge the financial support I received from the College of Medicine and the Department of Anatomy and Cell Biology.

Table of Contents

List of Tables

List of Figures

List of Abbreviations

ADC	apparent diffusion coefficient
APTRA-AM	2-aminophenol-N, N, O-triacetic acid acetoxymethyl ester
Ca^{2+}	calcium
CNS	central nervous system
CPCB	cell-permeant calcium buffer
DMSO	dimethyl sulfoxide
DWI	diffusion-weighted imaging
ELISA	enzyme linked immunosorbent assay
Gd	gadolinium
Gd-T1WI	gadolinium enhanced T1 weighted imaging
GFAP	glial fibrillary acidic protein
IFNγ	interferon gamma
K^+	potassium
MCA	middle cerebral artery
MRI	magnetic resonance imaging
Na^+	sodium
NF-κB	nuclear factor kappa B
NMDA	N-methyl-D-aspartate
PBS	phosphate buffered saline
ROI	region of interest
T2WI	T2 weighted imaging
T2*	T2 star
TE	echo time
TR	repetition time
TNFα	tumor necrosis factor alpha

List of Abbreviations

ADC	apparent diffusion coefficient
APTRA-AM	2-aminophenol-N, N, O-triacetic acid acetoxymethyl ester
Ca^{2+}	calcium
CNS	central nervous system
CPCB	cell-permeant calcium buffer
DMSO	dimethyl sulfoxide
DWI	diffusion-weighted imaging
ELISA	enzyme linked immunosorbent assay
Gd	gadolinium
Gd-T1WI	gadolinium enhanced T1 weighted imaging
GFAP	glial fibrillary acidic protein
IFNγ	interferon gamma
K^+	potassium
MCA	middle cerebral artery
MRI	magnetic resonance imaging
Na^+	sodium
NF-κB	nuclear factor kappa B
NMDA	N-methyl-D-aspartate
PBS	phosphate buffered saline
ROI	region of interest
T2WI	T2 weighted imaging
T2*	T2 star
TE	echo time
TR	repetition time
TNFα	tumor necrosis factor alpha

1.0 Introduction

Magnetic resonance imaging (MRI) has been used to monitor patho-physiological changes involved in the development of temporary and permanent focal ischemic injury in various animal models (Calamante et al., 1999); (Gill et al., 1995); (Li et al., 2000); (Minematsu et al., 1992); (Moseley et al., 1990); (Pierpaoli et al., 1993); (van Bruggen et al., 1994). Diffusion weighted imaging (DWI), detects injury prior to the onset of vasogenic edema, when tissue death results from cytotoxic edema (Armitage et al., 1998); (Benveniste et al., 1992); (Busza et al., 1992); (Moseley et al., 1990); (Rumpel et al., 1997); (van Gelderen et al., 1994). Other imaging modalities, including T2-weighted MRI (T2WI) and gadolinium-enhanced T1-weighted MRI (Gd-T1WI) have also played a role in the identification of areas affected by an ischemic event. During ischemia, the T2 relaxation time is prolonged in areas with an increase in water content (Lin et al., 1997) such as those affected by vasogenic edema (Ueda et al., 1999). Using Gd-T1WI, changes in blood-brain-barrier permeability and cerebral perfusion can also be identified (Reith et al., 1995); (Kastrup et al., 1999). Typically, these imaging modalities have been used in models of ischemia that involve large areas of the brain. In the experiments reported here, I have used the cortical devascularization model of hemorrhagic brain injury that causes a highly localized permanent focal ischemic event (Herrera, Cuello, 1992); (Berezovskaya et al., 1996); (Bartnik et al., 2001). The results

clearly demonstrate the ability of DWI to identify pathological changes associated with such a small injury.

The cortical devascularization model of ischemia is relatively unknown within the ischemia field, and as such, numerous histological and immunocytochemical experiments were performed to characterize the cellular events associated with infarct formation. While this model was originally chosen because of the small size of the resultant lesion, it also provided an opportunity to study ischemic pathology without the added complication of a reperfusion event. The results obtained from these experiments show that this type of injury results in delayed cell death, which is associated with reactive gliosis and an inflammatory response featuring leukocyte migration and pro-inflammatory cytokine secretion. The characterization of these events is extremely important in understanding the significance of the changes observed by MRI.

Based on the results of the studies detailing the temporal and spatial evolution of a cortical devascularization injury, we chose to examine the effectiveness of the cell-permeant calcium buffer, 2-aminophenol-N, N, O-triacetic acid acetoxymethyl ester (APTRA-AM), on ameliorating the ischemic cell death and its associated inflammatory response when administered after the ischemic injury. Moreover, a multiple b-value DWI study was used to ascertain if APTRA-AM treatment also inhibited the diffusion changes typically associated with a cortical devascularization injury. The results of this neuroprotection study show a significant reduction in infarct volume and diffusion related changes, suggesting that this compound may be an excellent candidate for clinical neuroprotection studies.

2.0 **Literature Review**

2.1 Cerebral Ischemia

Cerebral ischemia is a state of reduced cerebral blood flow resulting in both immediate and delayed cell death (Sweeney et al., 1995) with the severity and progression of cell death being directly proportional to the extent and duration of the ischemic event (van Bruggen et al., 1994); (Lipton, 1999).

The following sections briefly describe the differences between animal models of global and focal ischemia followed by a review of neuronal cell death. Changes in glial activation and the role of inflammation after an ischemic insult are also discussed.

2.1.1 Types of Ischemia

2.1.1.1 Global Ischemia

In rodent models of transient global ischemia, blood supply to the brain is interrupted for variable periods of time (usually ranging between 3 and 30 minutes) by occluding all four extracranial arteries under hypotensive conditions (reviewed in (Stoll et al., 1998); (Lipton, 1999)). Similarly, transient forebrain ischemia is produced by a temporary ligation of the two common carotid arteries (reviewed in (Stoll et al., 1998); (Lipton, 1999)). While the two-vessel occlusion model does not produce a global

ischemic event, it produces damage in a large portion of the forebrain similar to the global ischemia models (Lipton, 1999).

Global ischemia causes cell damage without pan-necrosis in the selectively vulnerable regions of the hippocampus, basal ganglia, and neocortex depending on the duration of the ischemic event (reviewed in (Stoll et al., 1998);(Lipton, 1999)). The hallmark feature of this injury is the delay between the insult and resultant cell death. As such, these models are useful to study the pathological mechanisms associated with delayed cell death in the absence of infarction.

2.1.1.2 Focal Ischemia

Typically models of focal ischemia involve either a proximal or distal occlusion of the middle cerebral artery (MCA) (Hoehn et al., 2001); (Hossman, 1998). In proximal occlusions, the MCA is occluded close to its branch point off the internal carotid artery whereas distal occlusions involve the smaller terminal branches off the MCA. Proximal MCA occlusion leads to infarctions of the basal ganglia and neocortex whereas a more distal occlusion will lead to a cortical infarction only (Stoll et al., 1998); (Hoehn et al., 2001). Currently, the most common methods of occlusion include the insertion of a nylon suture into the lumen of the carotid artery (Longa et al., 1989) or injection of a photothrombic substance such as Rose Bengal (Watson et al., 1985); although numerous other methods exist (reviewed in (Hossman, 1998)). Occlusion may be temporary or permanent, resulting in injuries that either affect only the selectively vulnerable cell populations of the hippocampus or all cell populations resulting in a pan-necrotic infarct.

After a transient focal ischemic insult, the resultant lesion will contain a core region where blood flow is reduced to < 15% surrounded by a penumbra region where blood flow is reduced to < 40% (Lipton, 1999). The core also undergoes rapid anoxic depolarizations, a rise in extracellular potassium (K^+) and intracellular calcium ($[Ca^{2+}]_i$) (Harris et al., 1981); (Harris, Symon, 1984). In contrast, the penumbra is subjected to waves of spreading depression, which result from the spread of increased K^+ and glutamate from the core of the lesion (Lipton, 1999). Spreading depression is a wave of reversible electroencephalogram (EEG) suppression that propagates at a rate of 2-5 mm/min across the cortical surface which is accompanied by a severe disruption in ion homeostasis (Shimizu et al., 2000); (Sonn, Mayevsky, 2000). The resultant disruption in ion homeostasis can then enhance brain damage in this region by increasing $[Ca^{2+}]_i$ and acidosis and causing the release of glutamate (Sonn, Mayevsky, 2000). It is important to note that although the penumbra is considered potentially salvageable (van Bruggen et al., 1994); (Small et al., 1999) the duration of the insult will determine if the penumbra becomes part of the infarct (Lipton, 1999); (Small et al., 1999) as is the case with a permanent ischemic insult.

2.1.2 Pathophysiology of Cerebral Ischemia

2.1.2.1 Neuronal Cell Death

Immediately after injury, neuronal cell death occurs in the core ischemic territory as a result energy failure, acidosis, and the disruption of critical ion ratios notably, high intracellular sodium and calcium levels (Moseley et al., 1990); (Siesjo, 1992); (Sweeney

et al., 1995); (Iadecola, Ross, 1997). In contrast, delayed cell death, which is observed primarily in the surrounding penumbra, is thought to be mediated in part by spreading depression, calcium shifts, glutamate excitotoxicity, free radical production, and inflammation (Siesjo, 1992); (Iadecola, Ross, 1997); (Dirnagl et al., 1999); (Small et al., 1999).

There are two distinct modes of cell death that are part of ischemic cell death, apoptosis and necrosis. Neurons have the ability to exhibit both forms of cell death and the pathway taken will be a function of the nature of the insult, the cell type, the age of the cell and the state of the cell at the time of the insult (Martin et al., 1998).

Necrosis is the result of acute cellular dysfunction and is a passive process associated with ATP depletion (Chandra et al., 2000). Morphologically, this process is characterized by membrane dysfunction, cell swelling, rupture of the plasma membrane, and the spilling of cellular contents into the extracellular space (reviewed in (Choi, 1992); (Chandra et al., 2000)). In contrast, apoptosis involves ordered, energy-dependent physiological processes that require the cell to degrade its own DNA resulting in chromatin condensation, marginalization and fragmentation without any change in cell membrane (reviewed in(Stoll et al., 1998); (Lipton, 1999)). DNA fragmentation gives rise to DNA fragments of 180 base pairs that can then be identified by gel electrophoresis or by terminal deoxyribonucleotidyl transferase (TNT)-mediated 2'-deoxyuridine-5'-triphosphate (dUTP)-digoxigenin nick end labeling (TUNEL) staining of tissue sections (reviewed in (Choi, 1996); (Stoll et al., 1998). Neurons undergoing apoptosis have been identified in both transient and permanent ischemia models. After transient ischemia, apoptotic neurons were found within the inner border zones as early

as 30 minutes, peaking at 24–48 hours and persisting for up to 4 weeks after the onset of reperfusion (Li et al., 1995). Similarly, apoptotic neurons were found throughout the infarct area within 12 hours of permanent focal ischemia (Braun et al., 1996).

The gene products associated with apoptosis have been studied in ischemic models and it appears that the Bcl-2 protein family regulates this process (Davis, Antonawich, 1997). The Bax protein actively promotes apoptosis unless it is bound to either Bcl-2 or Bcl-x long, which renders it less susceptible to apoptotic stimuli (Dixon et al., 1997). Thus the relationship of Bax to its anti-apoptotic homologs Bcl-2 and Bcl-x long seems to be the critical determinant of resistance to apoptotic cell death. In focal ischemia, neurons undergoing apoptotic cell death within the core and surrounding border zone express the Bax protein while surviving cells within the peri-infarct regions express Bcl-2 (Chen et al., 1995); (Isemann et al., 1998).

2.1.2.2 Mechanisms of Cell Death

2.1.2.2.1 Glutamate Excitotoxicity

Glutamate is a major excitatory neurotransmitter in the mammalian central nervous system (CNS). The post-synaptic effects of this excitatory amino acid are mediated by a number of distinct cell membrane receptors including the metabotropic and ionotropic N-methyl-D-aspartate (NMDA), kainate, and 2-amino-3- (3-hydroxy-5-methylisoxazol-4-yl) (AMPA) receptors (Kandel, Schwartz, 1991); (Lyden, Wahlgren, 2000). Activation of the ionotropic receptors leads to the opening of their associated ion channels, which are permeable to Na^+, K^+, and Ca^{2+} depending on the receptor type. The

metabotropic glutamate receptors are not necessarily associated with an ion channel pore but mediate their actions through second messengers, resulting in a mobilization of Ca^{2+} from internal stores (Lyden, Wahlgren, 2000).

Excitotoxic ischemic cell death is thought to result from an excessive release of glutamate. For example, during focal ischemia there is a rise in extracellular glutamate that begins within the first 2 minutes of MCA occlusion (Wahl et al., 1994). Glutamate release occurs via exocytosis, Ca^{2+} dependent vesicular release, and the reversal of the high-affinity Na^{+} dependent glutamate uptake mechanism (Lipton, 1999). Although virtually every glutamate receptor subtype has been implicated in neurotoxicity, the NMDA receptor sub-type has received most of the attention as it is generally accepted that glutamate excitotoxicity is initiated by Ca^{2+} flow through this receptor/channel complex (Choi, 1988); (Tymianski, 1996); (Lyden, Wahlgren, 2000).

2.1.2.2.2 Calcium Overload

Intracellular Ca^{2+} plays an important physiological role as a cellular messenger and under normal circumstances; signal transduction begins with the release of glutamate from the pre-synaptic terminal resulting in the activation of the post-synaptic NMDA receptors. This results in membrane depolarization, an opening of the voltage sensitive Ca^{2+} channels (VSCCs) and the removal of the Mg^{2+} block of the NMDA receptor, allowing Ca^{2+} to enter the cell (reviewed in (Kandel, Schwartz, 1991); (Lyden, Wahlgren, 2000)). Because of its' importance, there are numerous mechanisms that tightly regulate both the intracellular location and concentration of free cytoplasmic

Ca^{2+}. These mechanisms involve a complex interaction between Ca^{2+} influx, buffering, storage, and efflux.

Energy failure after an ischemic event has been hypothesized to cause an increased Ca^{2+} influx, decreased efflux and altered buffering and storage leading to an increase in intracellular Ca^{2+} (Figure 1) (Silver, Erecinska, 1990); (Tymianski, Tator, 1996); (Kristian, Siesjo, 1998). Specifically, the membrane depolarization that results from pump failure causes an opening of Ca^{2+} sensitive voltage gated channels as well as dislodging the Mg^{2+} ion from the NMDA channels facilitating Ca^{2+} influx (Tymianski, Tator, 1996); (Kristian, Siesjo, 1998); (Lipton, 1999). Second, when transmembrane Na^{+} gradients collapse during energy failure, the Na^{+}/ Ca^{2+} exchanger operates in reverse such that it begins to pump in Ca^{2+} instead of pumping it out (Tymianski, Tator, 1996). Finally, the disruption of energy levels also inhibits the storage of Ca^{2+}, as this process is ATP dependent in both the endoplasmic reticulum and mitochondria (Tymianski, Tator, 1996); (Kristian, Siesjo, 1998); (Sattler, Tymianski, 2002). The rise in the intracellular Ca^{2+} concentration results in neuronal death via the activation of phospholipases, endonucleases, proteases (i.e. calpain), protein kinases, phosphatases and enzymes that activate reactive oxygen species and nitric oxide (Figure 1) (Tymianski, Tator, 1996); (Kim et al., 1998); (Kristian, Siesjo, 1998); (Lipton, 1999); (Sattler, Tymianski, 2002).

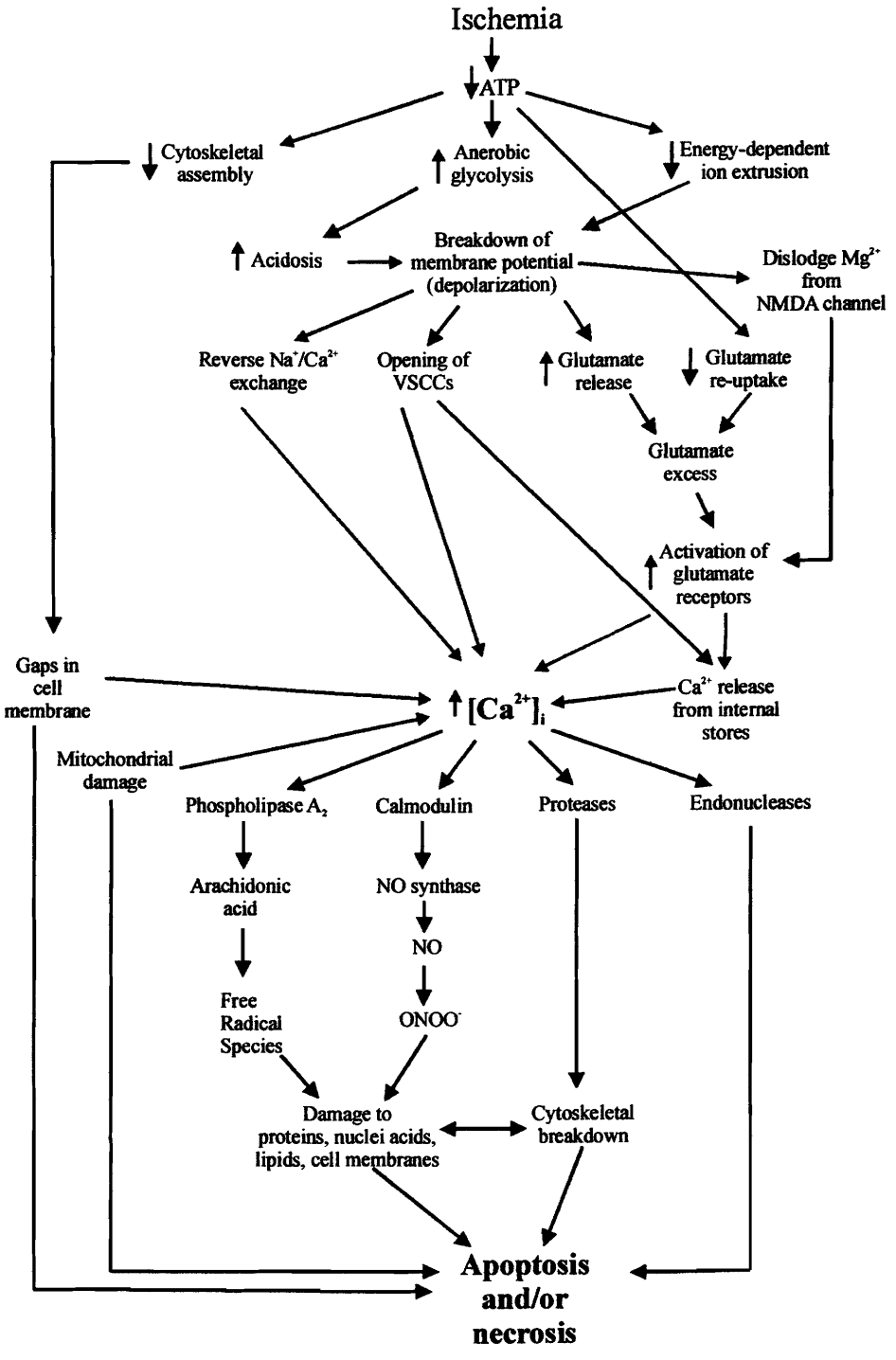

Figure 1: Mechanisms by which ischemia produces intracellular Ca^{2+} elevations which then result in neurotoxicity. Modified from Tymianski and Tator (1996).

2.1.2.2.3 Free Radical Formation

Normally the rate of free radical production is equal to that of free radical scavenging, however, ischemia creates several conditions that result in a net increase in the production of superoxide (O_2^-), hydrogen peroxide (H_2O_2), nitric oxide (NO) and peroxynitrite ($ONOO^-$). First, an accumulation of hypoxanthine due to the breakdown of adenine nucleotides will result in the production of O_2^- (Lipton, 1999). Second, O_2^- and the hydroxyl radical (OH^-) are generated by the increased oxidative metabolism of arachidonic acid which accumulates during the activation of the cyclooxygenase and lipoxygenase pathways (Iadecola et al., 1996); (Nogawa et al., 1997); (Lipton, 1999). Third, alterations in mitochondrial function will result in the excessive generation of free radicals if insufficient oxygen is available to accept electrons passed along the mitochondrial electron transport chain (Tymianski, Tator, 1996); (Lipton, 1999). Fourth, the accumulation and activation of neutrophils within the blood vessels and parenchyma can generate O_2^- during the respiratory burst and subsequent oxidation of the reduced form of nicotinamide adenine dinucleotide phosphate (NADPH; (Lipton, 1999). These reactive oxygen species target multiple components of the cell including lipids, DNA and proteins with a net result of a loss in cell integrity, enzyme function and genomic stability (Hensley et al., 2000).

In addition to increased reactive oxygen species production, neutrophils synthesize inducible nitric oxide synthase (iNOS) within the first 48 hours of ischemia, increasing the amount of nitric oxide (NO) present (Iadecola et al., 1995). NO can also be generated by neuronal or endothelial NOS via the activation of Ca^{2+}/calmodulin (Tymianski, Tator, 1996); (Iadecola et al., 1996); (Iadecola, 1997). The cytotoxic

actions of NO include the direct damage of chromatin by cross liking DNA, the inactivation of antioxidant enzymes and the generation of $ONOO^-$ by combining with O_2^- (Chandra et al., 2000).

There is also accumulating evidence that much of the free radical induced damage that is observed in ischemia is mediated by the nuclear factor kappa B (NF-κB) transcription factor (Clemens et al., 1997); (Carroll et al., 2000); (Clemens, 2000); (Seegers et al., 2000). Numerous studies have shown an increase in NF-κB activation in neurons after both transient (Gabriel et al., 1999); (Stephenson et al., 2000) and permanent (Seegers et al., 2000) MCA occlusion. NF-κB is a heterodimer of transcription factors belonging to the Rel family of proteins, which typically exists as a dimer containing a p65 and a p50 subunit anchored in the cytoplasm by a member of the IκB family of proteins (Baeuerle, Henkel, 1994); (Clemens, 2000). Following the activation of certain signal transduction pathways, IκB is phosphorylated, rendering this molecule susceptible to ubiquitination and subsequent degradation freeing NF-κB up to translocate to the nucleus (Flohe et al., 1997); (Trushin et al., 1999). Once inside the nucleus, this molecule can then bind to specific κB DNA sequences resulting in the transcription of a variety of genes including cytokines, adhesion molecules and enzymes such as iNOS and cyclooxygenase-2 (Clemens et al., 1997); (Gabriel et al., 1999);(Carroll et al., 2000); (Clemens, 2000); (Christman et al., 2000). In turn, these molecules then act to enhance the immune response. Moreover, a number of these activated molecules (specifically the cytokines) can activate NF-κB themselves, initiating an autoregulatory feedback loop (Ghosh et al., 1998)

2.1.2.3 Glial Activation

The involvement of glial cells is a consistent feature in almost all forms of brain injury. Both microglia and astrocytes display a graded response to ischemia and it appears that both the strength and time course of the response is dependent on the severity of the injury. The following outlines some of what is currently known about microglial and astrocyte activation after an ischemic insult.

2.1.2.3.1 Microglia

Microglial make up approximately 10 - 12% of the total glial cell population in the CNS (Gonzalez-Scaano, Baltuch, 1999); (Stoll, Jander, 1999). Microglia are located in the vicinity of neurons within the gray matter, between the fiber tracts in the white matter (Lawson et al., 1990), and in close contact with blood vessels (Graeber, Streit, 1990). Resting microglia have a unique ramified morphology and can be identified immunohistochemically by staining for isolectin B4 and the complement type-3 receptor (CD11b/CD18 complex). Microglia are considered the primary immune effector of the CNS and as such, they respond by migrating to the site of injury where they proliferate, become activated and transform into phagocytes (Stoll et al., 1998); (Gonzalez-Scaano, Baltuch, 1999); (Kato, Walz, 2000). During the activation process, cells begin to retract their processes and develop an enlarged/rounded cell body (Stoll et al., 1998). Eventually, these cells assume a phagocytic morphology and can be identified using the ED-1 monoclonal antibody or antibodies against the major histocompatability class II (MHC-II) antigen (Banati et al., 1993); (Schroeter et al., 1999; Stoll, Jander, 1999);

(Kato, Walz, 2000). At this stage, the phagocytic microglia become indistinguishable from hematogenous macrophages (Schroeter et al., 1999).

The microglial response is dependent upon the severity of the injury. For example with sub-lethal injuries or when only the selectively vulnerable cell populations are affected there is an early, transient activation. However, when a pan-necrotic infarct forms, there is an immediate loss of microglia in the core, with activation of the remaining microglia in the peri-infarct and border zones (Kato, Walz, 2000). Typically, ramified microglia are found within the ischemic areas starting 4 - 6 hours after permanent focal ischemia with phagocytic microglia first appearing in peri-infarct areas approximately 24 hours after injury (Davies et al., 1998); (Schroeter et al., 1999). In most cases, activated microglia remain visible in the peri-infarct and border zones up to 7 days after injury after which time the number of these cells begins to decline (Kato et al., 1996); (Mabuchi et al., 2000).

Activated microglia synthesize numerous potentially harmful factors including NO, O_2^- and H_2O_2, proteolytic enzymes, and the pro-inflammatory cytokines, macrophage inflammatory protein-1 (MIP-1) (Gourmala et al., 1999)), tumor necrosis factor-α (TNF-α) and interleukin 1β (IL-1β) (Banati et al., 1993); (Gonzalez-Scaano, Baltuch, 1999); (Stoll, Jander, 1999).

2.1.2.3.2 Astrocytes

Two types of astrocytes have been recognized, protoplasmic astrocytes, which exist in key positions adjacent to neurons and synaptic clefts within the gray matter and

fibrous astrocytes, which occupy positions adjacent to axons within the white matter (Peters et al., 1991). Numerous functions have been attributed to this cell population and in general, it can be said that astrocytes function to maintain the appropriate extracellular environment for proper neuronal function. Specifically, astrocytes contain high levels of glutamine synthetase, which in conjunction with glutamate transporters, remove and detoxify extracellular glutamate and provide the neuronal substrate glutamine (Eddleston, Mucke, 1993); (Amedee et al., 1997). Astrocytes also store glycogen and have the potential to provide lactate as an alternative aerobic energy substrate for neurons (Tansey et al., 1991); (Sonnewald et al., 1997). These cells also provide neurotrophic support for neurons by releasing nerve growth factor (NGF), basic fibroblast growth factor (bFGF), and insulin like growth factor 1 (IGF-1), (Gluckman et al., 1992); (Eddleston, Mucke, 1993); (Liu et al., 1999). In addition, astrocytes play a role in controlling the blood-CNS interface as they are in direct contact with endothelial cells via their end feet processes and can influence the trafficking of hematogenous cells across the blood-brain-barrier via the release of cytokines and adhesion molecules (Eddleston, Mucke, 1993).

In response to injury, the CNS increases the size and number of astrocytes, with a concomitant increase in glial fibrillary acidic protein (GFAP) expression and shape change from a protoplasmic to a stellate morphology (Eddleston, Mucke, 1993); (Stoll et al., 1998); (Raivich et al., 1999). The transition from a resting to activated state is associated with the expression of adhesion molecules, MHC I and II antigen presentation molecules, pro- and anti-inflammatory cytokines (e.g. IL-1β, TNF-α, interferon-γ (IFN-γ), transforming growth factor–β (TGF-β), interleukin-6 (IL-6), growth factors (e.g.

platlet-derived growth factor (PDGF), IGF-1, bFGF, cytoskeletal elements (e.g. MAP 2, vimentin), early response elements (e.g. AP-1, c-fos), and eicosanoids (e.g. prostaglandin E) (Eddleston, Mucke, 1993); (Raivich et al., 1999).

Depending on the severity of the ischemic injury, there is a rapid induction of dispersed astrogliosis within 12–24 hours after injury, which then becomes much more focused within the infarct region and eventually develops into a glial scar between 15–30 days of injury (Clark et al., 1993); (Raivich et al., 1999). In models of permanent focal ischemia, the astrocytes within the infarct appear with enlarged, pale nuclei, swollen processes and decreased GFAP immunoreactivity early after the ischemic event (Davies et al., 1998); (Liu et al., 1999). These swollen cells are most often observed in the expanding infarct zone and will eventually die as a result of the infarct spreading. However, surrounding the infarct within the border zone are the numerous reactive astrocytes with increased GFAP immunoreactivity that make up the glial scar (Liu et al., 1999). Whether this glial scar is beneficial or harmful still remains unclear. A glial scar may help to wall off areas of tissue necrosis in an attempt to exclude non-resident cells from invading the CNS as well as filling in the space left after neuronal loss. On the other hand, the barrier formed by the glial scar may hinder regenerative processes (Eddleston, Mucke, 1993)

2.1.2.4 Post-Injury Inflammation

After an ischemic event, the brain is capable of mounting an inflammatory response, which includes the activation and accumulation of the resident microglia and astrocytes as well as blood-derived leukocytes (Iadecola, Alexander, 2001). It is

generally accepted that this inflammatory reaction is involved in the amplification of injury in both the acute and sub-acute phases of ischemia.

The exact nature of the response is still unknown, however most reports acknowledge a role for pro-inflammatory cytokines, chemotactic cytokines, adhesion molecules, enhanced permeability of the blood-brain barrier and the resultant accumulation of leukocytes as key components in this response. The following sections focus on blood-derived leukocytes and cytokines, which act as effectors and mediators of the post-injury inflammatory response.

2.1.2.4.1 Leukocytes

Significant amounts of histological evidence have shown that leukocyte accumulation is an early event which coincides with the period of infarct progression, suggesting these cells contribute to ischemic damage (Hallenbeck, 1996); (Pantoni et al., 1998); (Iadecola, Alexander, 2001). Leukocyte accumulation after stroke represents the accumulation of mixed subpopulations, including neutrophils, monocytes and lymphocytes. The relative contribution of these subpopulations differ with neutrophils being the primary population in the early stages of the inflammatory reaction whereas the monocytes arrive within 3–7 days and then persist for multiple weeks (Akopov et al., 1996).

Some debate exists regarding the contribution of inflammation in permanent focal ischemia or if this process is limited to transient ischemic events that feature a reperfusion phase. Zhang et al. (1994), Braun et al. (1996), and Kato et al. (1996) all report leukocyte accumulation in infarcted tissues within 24 hours after both permanent

and transient ischemia. While the temporal studies differ slightly, generally neutrophils begin to infiltrate into ischemic areas within 30 minutes to 12 hours, peak between 24–72 hours and then disappear by 7 days (Garcia et al., 1994); (Zhang et al., 1994); (Kato, Walz, 2000). Monocytes invade in a second wave 2 – 3 days after ischemia (Akopov et al., 1996); (Kato, Walz, 2000). In general, permanent focal ischemia leads to a smaller, more delayed inflammatory reaction than observed in transient ischemia (Zhang et al., 1994); (Jiang et al., 1998).

Both neutrophils and monocytes express complement receptor 3, MHC class I and II antigens, and ED-1 (Kato, Walz, 2000). The migration of these cells into the parenchyma occurs via a highly specific receptor-ligand interaction between intercellular adhesion molecule 1 (ICAM-1) on endothelial cells and a group of CD11/CD18 glycoproteins on the leukocytes (Kochanek, Hallenbeck, 1992); (Arvin et al., 1996); (Becker, 1998); (Lipton, 1999); (Kato, Walz, 2000); (Kubes, Ward, 2000). An increased expression of these molecules is observed after focal ischemia and appears to be under the control of pro-inflammatory cytokines, including TNFα and IL-1β which are released by activated microglia and astrocytes (Matsuo et al., 1994); (Zhang et al., 1994); (Jander et al., 1996); (Kubes, Ward, 2000).

The postulated effects of neutrophils and monocytes to the pathogenesis of stroke include: 1) reduced cerebral blood flow by vessel plugging resulting in the "no-reflow" phenomenon, 2) exacerbation of blood-brain-barrier and parenchymal injury via hydrolytic enzyme release, lipid mediator production or reactive oxygen species production and 3) the initiation of thrombosis (Kochanek, Hallenbeck, 1992); (Akopov

et al., 1996); (Hallenbeck, 1996); (Becker, 1998); (Jiang et al., 1998); (Pantoni et al., 1998).

2.1.2.4.2 Cytokines

Cytokines are soluble polypeptide mediators that act as intercellular messengers that control the growth, differentiation, and function of numerous cell types, most notably those of the immune system (Woodroofe, 1995).

In recent years a substantial amount of experimental evidence has accumulated to identify a role for the pro-inflammatory cytokines IL-1β and TNF-α in the recruitment and trafficking of neutrophils and monocytes into ischemic areas (Feuerstein et al., 1997); (Rothlein et al., 1988); (Lipton, 1999). Specifically, these molecules cause an up regulation of endothelial adhesion molecules (Liu et al., 1994); (Arvin et al., 1996); (Pantoni et al., 1998) as well as the activation of glial cells (Feuerstein et al., 1998); (Gregersen et al., 2000). A number of studies have shown that both IL-1β and TNF-α mRNA are elevated in the ischemic cortex as early as 1 hour after occlusion and up to 4 days following permanent MCA occlusion (Liu et al., 1994); (Arvin et al., 1996); (Feuerstein et al., 1997); (Pantoni et al., 1998); (Touzani et al., 1999). In many cases, cytokine gene expression within cerebral infarcts precedes the macrophage response (Liu et al., 1994); which suggests a CNS derived source of pro-inflammatory cytokine production. Astrocytes, microglia and neurons have all been identified as sources of TNF-α (Liu et al., 1994); (Arvin et al., 1996); (Botchkina et al., 1999) and IL-1β (Woodroofe, 1995); (Feuerstein et al., 1997); (Clark et al., 1999); (del Zoppo et al., 2000).

acetoxymethyl ester (EGTA-AM), 1,2 *bis*- (2-aminophenoxy) ethane-N, N, N', N'-tetraacetic acid acetoxymethyl ester (BAPTA-AM), or APTRA-AM.

Originally, these buffers were used to control or estimate the free cytoplasmic concentration of Ca^{2+}, however, more recently they have been shown to be neuroprotective. Specifically, both EGTA-AM and BAPTA-AM have been shown to protect against early glutamate-induced excitotoxicity *in vitro* and against focal cerebral ischemia *in vivo* (Tymianski et al., 1994); (Tymianski, 1995). In addition, APTRA-AM was shown to be an effective neuroprotectant against anoxic/aglycemic damage *in vitro* (Abdel-Hamid, Tymianski, 1997). It should be noted that in these experiments, the buffers were applied prior to the insult, so what remains unanswered is whether these molecules will be neuroprotective if given after the onset on injury.

Initially, it was thought that neuroprotection by these Ca^{2+} buffers stemmed from their ability to globally buffer excessive intracellular Ca^{2+} loads. However, additional studies suggested that the rate of calcium binding directly affected the buffer's neuroprotective effect. For example, those Ca^{2+} buffers which possess fast forward rates of calcium binding, such as BAPTA-AM or APTRA-AM, protect neurons more effectively than EGTA, a slow-binding Ca^{2+} buffer (Spigelman et al., 1996). This suggests that these molecules may be protective via other mechanisms, including the attenuation of presynaptic transmitter release (Tymianski et al., 1994); (Spigelman et al., 1996) which was demonstrated by its ability to reduce evoked potentials in the rat hippocampus *in vivo* (Spigelman et al., 1998).

2.2 Magnetic Resonance Imaging

2.2.1 Overview of MRI Principles

The following sections contain a brief outline of the basic physical principles associated with magnetic resonance imaging. For a more detailed review, see texts by (Hashemi, Bradley, 1997), (Mitchell, 1999) or (Woodward, 2002).

2.2.1.1 Proton Precession and Resonance

MRI takes advantage of the fact that the nucleus of a hydrogen atom has a magnetic moment, meaning that it has both charge and spin. Magnetic moment is defined as:

$$\text{Magnetic moment} = \mu = \gamma \hbar I \tag{2.1}$$

where γ = gyromagnetic ratio, h is Plank's constant (6.6252×10^{-27} ergs) and I is the spin angular momentum. Nuclei of certain elements have a magnetic moment; as such, when they are placed in a magnetic field their protons will line up in the direction of the field. Each proton that is aligned to the direction of the external magnetic field will then precess around the angle of the external field as well as around their own axis (Figure 2).

The frequency at which a nucleus precesses is a function of both the strength of the magnetic field and its unique gyromagnetic ratio. This frequency is referred to as the Larmor frequency and is given by the equation

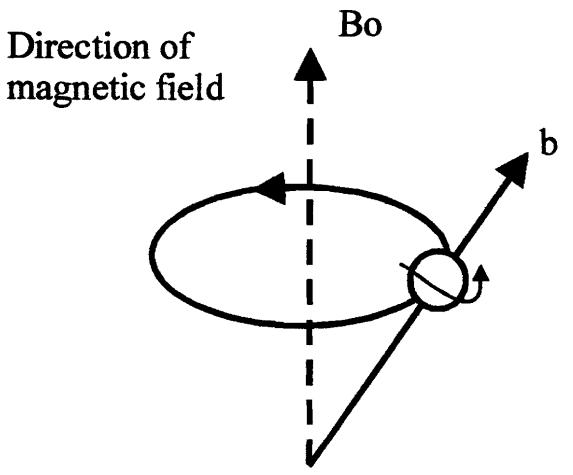

Figure 2: Diagrammatic representation of a proton spinning around the external magnetic field (Bo) and it's own axis (b).

The effects of TNF-α are mediated by both the p75 and p55 TNF-α receptors, which are expressed at different levels on glia, neurons and infiltrating leukocytes. Binding of TNF-α to its receptors leads to the activation of various signal transduction molecules including, protein kinase C, tyrosine kinase, and phospholipases A_2 (Pantoni et al., 1998). The activation of the TNF-α signal transduction pathway results in the activation of the NF-κB transcription factor which then translocates into the nucleus where it activates the promoters for numerous adhesion molecule, cytokines and antioxidant enzymes (Guerrini et al., 1995); (Pantoni et al., 1998); (Gregersen et al., 2000). Similarly, IL-1β binds to it's cell surface receptor, IL-1RI to produce an intracellular signal that is mediated by the NF-κB transcription factor (Guerrini et al., 1995); (Pantoni et al., 1998); (Touzani et al., 1999); (Rothwell, Luheshi, 2000). Again, there is also an important positive feedback loop between cytokines, NF-κB, and free radicals as they all activate one another (Wallach, 1997).

2.1.3 Cell Permeant Calcium Buffers

As previously discussed, it is generally well accepted that ischemic cell death is the result of excessive activation of glutamate receptors. This process triggers and sustains an increase in intracellular Ca^{2+} that results in the activation of numerous intracellular processes that can cause cell damage (see Figure 1). With this in mind, one possible method of protecting neurons from ischemic injury may be through the use of molecules that prevent Ca^{2+} from entering the cell, or interfere with its ability to trigger secondary neurotoxic cascades. This can be achieved by using cell-permeant calcium buffers such as ethyleneglycolbis (β-aminoethyl ether)-N, N, N', N'-tetra-acetate

$$\omega = \gamma B_o \tag{2.2}$$

where ω is the angular precessional frequency of the proton (in Hz), γ is the gyromagnetic ratio and B_o the strength of the external magnetic field. For hydrogen, the γ is 42.6 MHz/Tesla. The Larmor frequency is also important, as it is the frequency at which the proton will absorb energy, which will cause it to change its alignment. The process by which it absorbs energy at the Larmor frequency is called resonance.

Atomic nuclei have specific energy levels that are related to a property called spin quantum number (S). The number of energy states (E) of a nucleus is determined by the formula:

$$E = 2S + 1 \tag{2.3}$$

Hydrogen has a single proton, a spin quantum number of ½ and two energy states, denoted as + ½ and -½. Thus hydrogen protons spin about their axis creating a magnetic field with some protons spinning in the opposite way and creating a magnetic field in the opposite direction. However, because hydrogen has a single proton, there is a net magnetic field in one direction creating the magnetic moment that is used in MR imaging.

2.2.1.2 Longitudinal and Transverse Magnetization

Protons within the object to be imaged, line up with the external magnetic field in either the same direction as the field (parallel) or in the opposite (anti-parallel) direction. The protons also exist in two energy states, with those protons with a lower energy state

(E_1) lining up parallel to the magnetic field and those with a higher energy state (E_2) lining up anti-parallel to the magnetic field (Figure 3). Over time, more spins line up in the direction of the magnetic field creating a net magnetization vector, which is the sum of the contributions of all magnetic moments of the individual protons. This increase follows an exponential growth curve that is dependant on the density of the protons (or spins) in the tissue and the strength of the magnet.

The net magnetization vector (M_o) can be aligned in two directions, longitudinal (M_z) which is aligned along the direction of the external magnetic field (B_o) and transverse (M_{xy}) which is aligned along the direction of the x-y plane (Figure 4).

2.2.1.3 Radio Frequency (RF) Pulse

The goal of MR imaging is to move protons out of their alignment with the external magnetic field and then measure the signal generated as they relax. In the three dimensional laboratory coordinate system, the net magnetization vector M_o points in the z direction ($M_o = M_z$; Figure 5 A). M_o does not precess, as it is made up of the sum of all the individual magnetic moments of the individual protons, which are out of phase with one another. To change the orientation of M_o, protons are set to precess around a different magnetic field that is introduced by applying an RF pulse at the Larmor frequency. This flips the protons into the x-y plane and they begin to precess in phase around the x-axis creating a weaker magnetic field associated with the RF pulse, B_1 (Figure 5 B). The application of the RF pulse also boosts some of the protons from the lower energy state to the higher energy state contributing to the gain of transverse

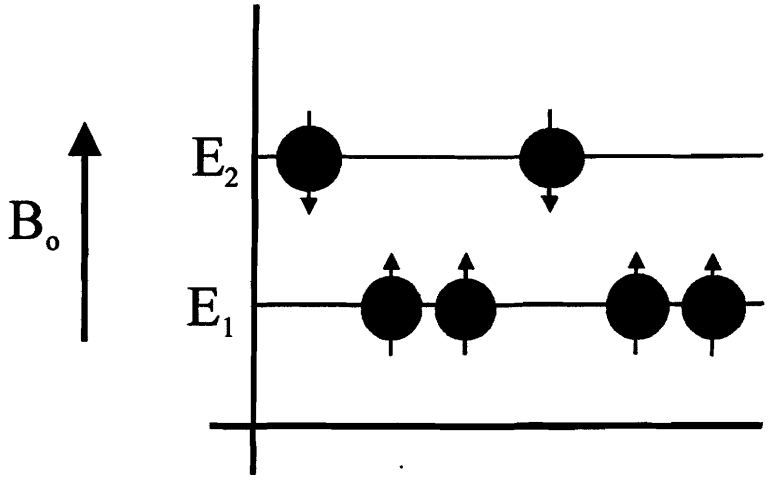

Figure 3: Diagram showing the two energy states of protons and the direction they align themselves in a magnetic field.

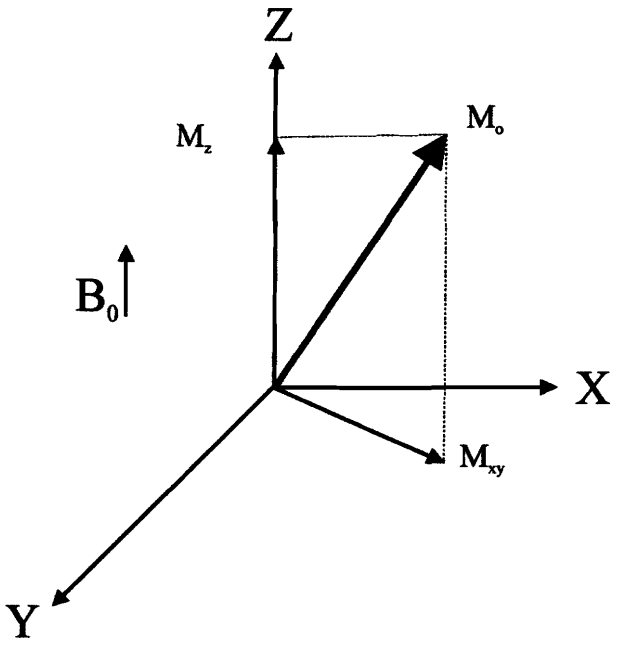

Figure 4: The net magnetization vector showing the longitudinal component (M_z) aligned in the direction of B_o and the transverse component (M_{xy}) aligned in the x-y plane.

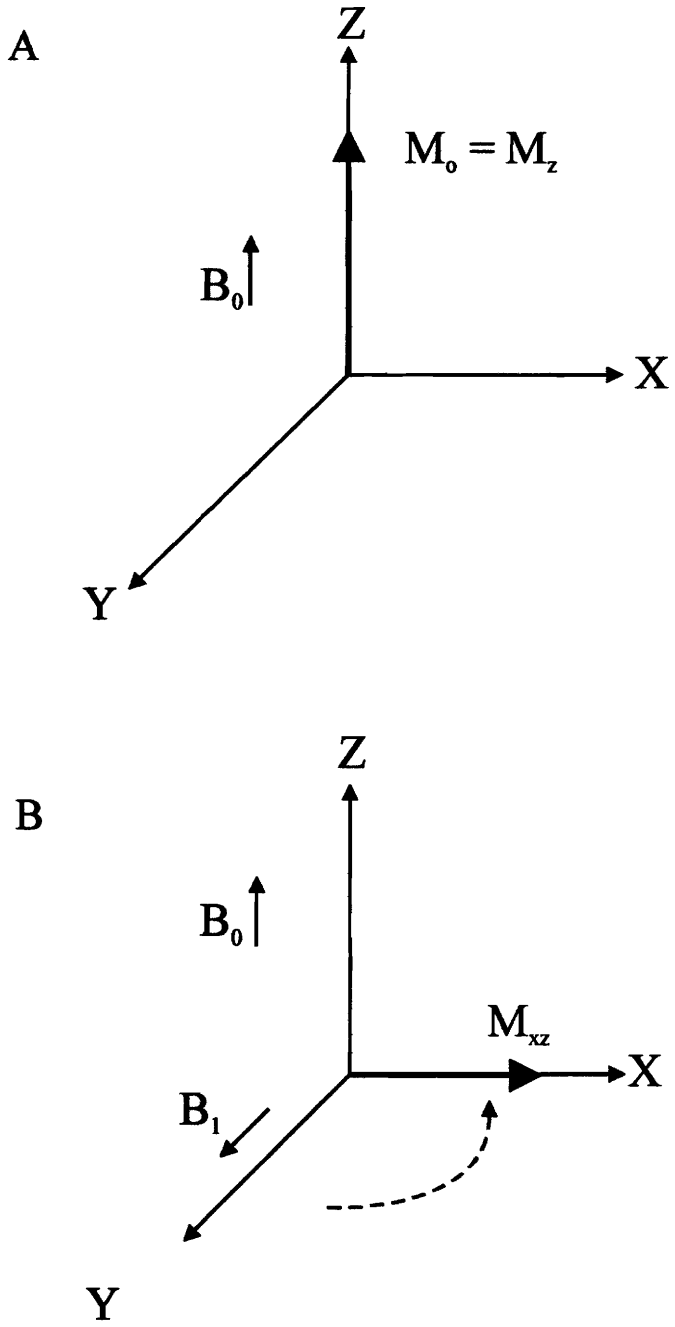

Figure 5: A net magnetization vector (M_o) before an RF pulse is applied (A) and after an RF pulse is applied (B). Prior to the RF pulse, the net magnetization is aligned with B_o ($M_o = M_z$). After an RF pulse, the magnetization flips to the transverse plane (M_{xz}) and begins to rotate around the magnetic field generated by the RF pulse, B_1 (B).

magnetization. When the RF is turned off, the protons stop precessing around the x-axis and begin to decay towards the z-axis.

The precession of protons around the x-axis induces a current in an RF receiver coil and a signal is generated. However, the signal continuously decays in magnitude as it precesses around this x-y plane. The signal received by the receiver coil is called frequency induction decay (FID) due to signal decay. The received FID is collected from all the different protons in the sample with no spatial discrimination.

2.2.1.4 Longitudinal and Transverse Relaxation

Relaxation refers to the return of protons back to their lowest energy states and the return of magnetization along the B_0 axis to M_z. The relaxation of the net magnetization is composed of both a longitudinal (T1) and transverse (T2) component. T1 and T2 relaxation are inherent properties of tissue that occur independently and account for tissue contrast.

T1 relaxation is the time it takes for the spins to realign themselves along the z (longitudinal) axis after being flipped 90° to the x-axis by an RF pulse. The longitudinal component grows as the net magnetization returns to its original state of B_0. More specifically, T1 refers to the time (in ms) in which the longitudinal magnetization grows to 63% of its original state (Figure 6A). T1 relaxation is also referred to as spin-lattice relaxation, meaning that as protons re-align with M_z they give up energy to the lattice or environment surrounding them. This occurs after the RF pulse is turned off and the spins return to their lowest energy states becoming out of phase with one another. The equation governing this behavior is:

A

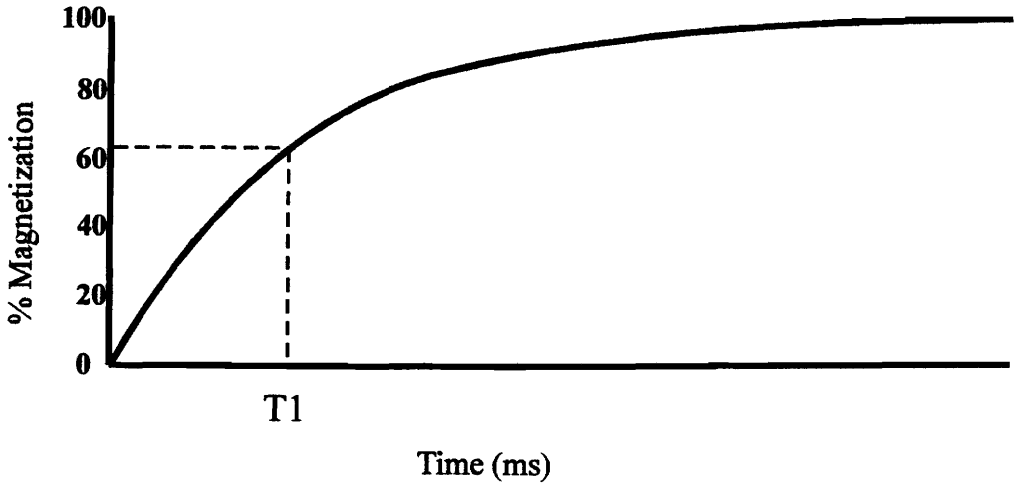

B

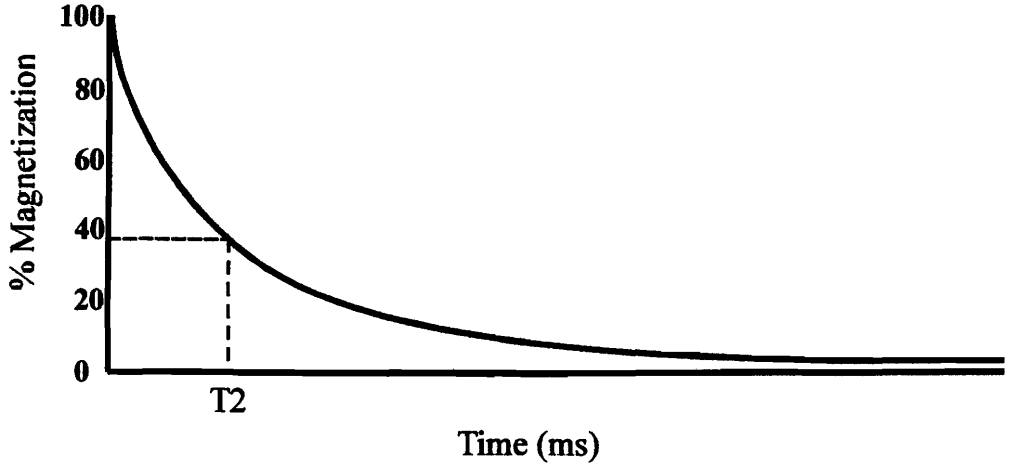

Figure 6: T1 and T2 relaxation curves. At time T1, the longitudinal magnetization has relaxed to 63% of its initial value (A). At time T2, the transverse magnetization has decayed to 37% of its initial value (B).

$$M_z = M_o (1 - e^{-t/T1}) \quad (2.4)$$

T2 relaxation occurs as the transverse magnetization decays back to its original state of zero. More specifically, T2 is the time (in ms) in which the transverse magnetization decays to 37% of the original (Figure 6B), which can be expressed as:

$$M_{xy} = M_o e^{-t/T2} \quad (2.5)$$

Transverse relaxation is known as spin-spin relaxation because of the dephasing of spins over time. Dephasing occurs because the interactions between the individual spins affect each other by altering their precessional frequencies. Any in-homogeneities in the external magnetic field will also result in protons precessing at different rates throughout the tissue due to the slight variations in field strength. As dephasing continues, the individual magnetic moments making up the net magnetization begin to cancel one another out and the net magnetization becomes smaller.

A second type of T2 relaxation occurs, T2*, which is not a tissue specific property but occurs due to inherent properties of the external magnetic field. After a 90° RF pulse, all protons begin to precess in phase at a rate proportional to the magnetic field. If the magnetic field is not homogenous, some protons will precess faster or slower than others, causing them to spin at slightly different frequencies. These differences in frequency place the protons out of phase with one another, thereby contributing to the transverse relaxation.

2.2.1.5 Tissue Contrast Characteristics

The concentration of hydrogen protons, or proton density, differs between tissue types to give tissue contrast when the imaging parameters are carefully adjusted. Each tissue acquires a high, intermediate, or low level of longitudinal magnetization based on its proton density, which is converted to various levels of measured signal and ultimately signal intensity on the final image. Tissues with a high proton density produce high areas of signal and appear bright on the final image whereas tissues with a low spin density convert to low areas of measured signal and dark areas on the final image.

T1 and T2 relaxation values also differ between various types of tissue and as such the imaging parameters can also be adjusted to produce the greatest separation in the areas of tissue contrast. In spin echo imaging, the two parameters that determine tissue contrast are TR (repetition time) and TE (echo time). These parameters are intimately associated with T1 and T2, respectively. TR (in ms) is the amount of time that elapses between successive RF pulses and is the amount of time the individual proton vectors are allowed to realign with the main external magnetic field prior to the next RF pulse. Generally, the TR is not long enough to allow full T1 recovery. TR effects tissue contrast by defining how much magnetization each tissue recovers in the longitudinal plane, which in turn converts to the same level of measurable signal (bright or dark) in the final image.

TE (in ms) is the amount of time between a 90° pulse and when the signal echo is measured. TE effects contrast by determining how much of the measurable signal is maintained or lost by allowing variable amounts of dephasing to occur. For example,

with a long TE, the signal has more time to decay (both T2 and T2*) resulting in a greater tissue contrast between tissues.

The process by which the TR and TE of an imaging sequence are adjusted to produce the tissue contrast of choice is called weighting. The T2 characteristics of a particular tissue are determined by how fast the protons in that tissue dephase. If the protons dephase rapidly then the tissue is said to have a short T2 and if they dephase slowly then it has a long T2. Generally, water has a long T2, fat and proteinaceous substances have an intermediate T2 and solids have short T2 characteristics. The T1 characteristics of tissue depend on the ability of their protons to give off energy to their surroundings. Typically, fat and proteinaceous substances have a short T1, solids have an intermediate T1 and water has the longest T1. In the brain, white matter has a short T1 and T2, gray matter has both an intermediate T1 and T2 and cerebrospinal fluid (CSF) has a long T1 and T2 (Figure 7).

In proton density imaging, contrast is achieved by using a long TR and a short TE. The long TR ensures that tissues can reach full longitudinal magnetization (removing the T1 component) while the short TE ensures a minimal loss of signal due to T2 relaxation. In T1 weighted imaging the desired tissue contrast is produced using a short TR and a short TE. The short TR allows tissues with short T1 values to fully recover and those with a long T1 to only partially recover. The short TE minimizes the signal loss due to transverse magnetization. With T2 weighted imaging, contrast is produced using a long TR and a long TE. The long TR allows tissues to reach full longitudinal magnetization and the long TE allows a controlled loss of transverse magnetization.

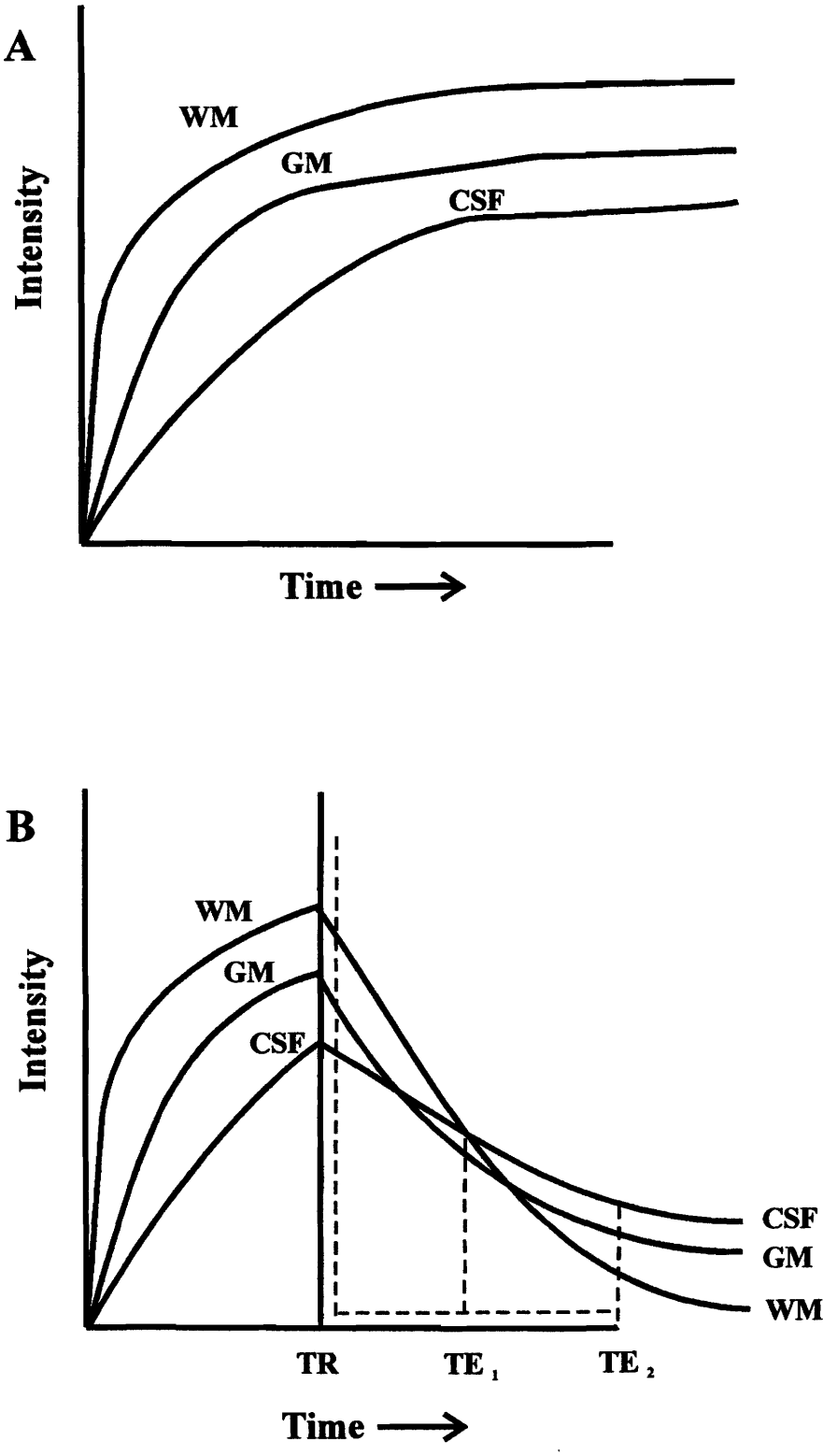

Figure 7: T1 recovery (A) and T2 decay (B) curves of white matter (WM), gray matter (GM), and CSF.

2.2.1.6 Image Construction

The signals received after RF pulses contain information about the entire object being imaged without any spatial information. To collect information about a specific area in the object, 3 gradients, one placed in each direction (G_x, G_y, G_z) are used. Depending on the slice orientation (axial, sagital, transverse), these gradients can be used for slice-select, read-out or phase encoding. Gradients function by creating a temporary magnetic field that changes from point to point in a linear fashion along all 3 axes in order to provide spatial information.

As previously mentioned, when an object is placed in the magnetic field and an RF pulse applied, the resultant FID contains information from the entire object. To collect information from a specific slice or area through that object, the slice select gradient (G_z) is used to alter the magnetic field along the z-axis. This creates a situation where each area of the object will have a slightly different magnetic field strength. Then when an RF pulse with a bandwidth of frequencies which match the Larmor frequencies of that slice are applied, only the protons within that slice will be excited. This process "selects" a slice through the object being imaged without distinguishing points within that slice.

Spatial encoding is the process used to discriminate points within a slice. Spatial encoding is a two-step process involving a frequency encoding step and phase encoding step. Frequency encoding collects spatial information in the x-direction by applying the read-out gradient (G_x) in the x direction when the echo is being received. This alters the field strength in the x direction such that the center of the slice does not experience the

gradient while the columns of pixels to the left will have a lower magnetic field and columns of pixels to the right will have a higher magnetic field. Because the frequency of proton precession is dependant in part on magnetic field strength, protons in the center will precess at the Larmor frequency while protons to the right precess at a slightly higher frequency and protons to the left will precess at a slightly lower frequency. As a result, each column of pixels will have a different frequency making the individual columns within the slice identifiable after the Fourier Transform (FT).

In order to discern spatial information in the y direction a two-dimensional FT is used. This involves the addition of the phase encoding gradient (G_y) in the y direction. The G_y gradient is applied prior to the G_x gradient so that before the frequency encoding step, the pixels in the upper rows experience a higher magnetic field, the pixels in the lower rows experience a lower magnetic field and the center pixels remain unchanged. The G_y gradient causes the protons in the upper rows to precess faster and the protons in the lower rows to precess slower; creating a situation where each row will be out of phase with the others. The application of G_y and G_x result in each pixel have both a distinct frequency and phase, which will encode for the x and y coordinates of that pixel. Phase encoding takes a significant amount of time because there is a separate phase encode step, taking time TR for each row of pixels in the slice.

For every frequency and phase encoding step a signal is generated. Each digitized signal fills one line in a set of rows referred to as k-space. With the first TR, there is no phase shift and the resultant signal is placed in a row in k-space. After the second TR, containing a phase shift and frequency encoding step, the resultant signal is placed in a different row of k-space. This continues until all of the rows of the slice have

been phase shifted and frequency encoded. The number of frequency encoding steps required is specified by the matrix size of the slice selected.

The final step in image creation is the FT, which produces pixel data with different gray scale values. In order to generate an image, the signals, which occur in the time domain, are converted to the frequency domain using the FT. The FT then gives the amplitude and phase of each frequency within each signal, yielding pixel data that has a value representing the MR signal amplitude from that spatial location, allowing a 2 or 3 dimensional image to be created.

2.2.1.7 MRI Hardware

A diagrammatic representation of the hardware components of an MR imaging system is shown in Figure 8. The magnet produces the B_0 field for the imaging procedure. Within the magnet are the gradient coils, G_x, G_y and G_z for producing a gradient in the x, y, and z directions. Adjacent to the gradient coils is the RF coil, which produces the B_1 magnetic field necessary to flip the spins 90° or 180°. The RF coil is also the RF receiver and can detect the signal from the spins within the body. The object to be imaged is placed within the magnet and the entire set up is contained within an RF shield, which prevents the RF signal generated by the imaging system from radiating out of the area while also preventing various RF signals from other sources being detected by the scanner. The computer controls all the components on the scanner including the RF source, pulse programmer, the RF amplifier, the gradient pulse programmer and the gradient amplifier. The RF source produces a sine wave of the desired frequency and

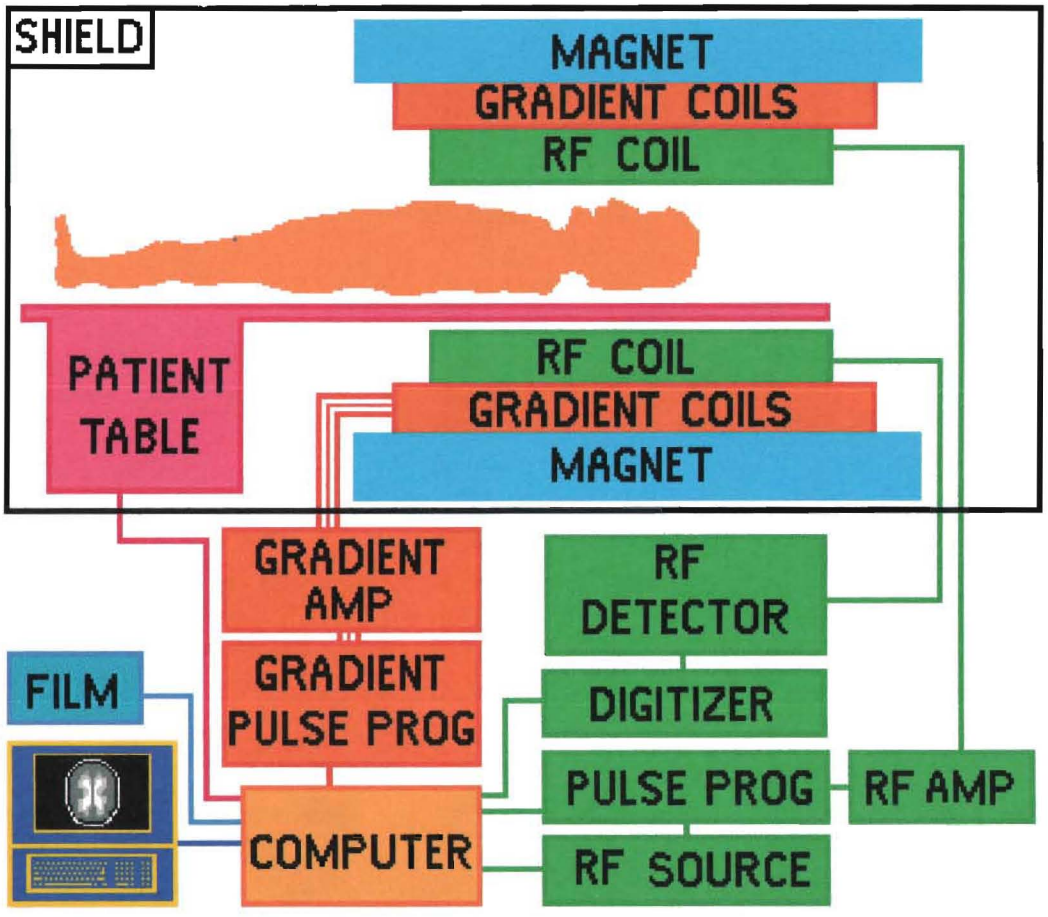

Figure 8: Diagrammatic representation of the typical components found in an MR imaging system (from Hornak, 1996).

the pulse programmer shapes the RF pulse. The RF amplifier increases the pulse's power. The gradient pulse programmer sets the shape and amplitude of each of the three gradient fields while the gradient amplifier increases their power to a level high enough to drive the gradient coil.

The following sections provide more detail on magnets and RF coils.

2.2.1.8 Magnets and Static Fields

There are different types of magnets used in imaging experiments: permanent, resistive, and superconducting. Permeant magnets contain material that directly creates a magnetic field. The axis of these magnets runs perpendicular to the bore of the magnet. The strength of the magnet is typically 0.5T but new technology is increasing this field strength. Resistive magnets generate magnetic fields perpendicular to an electrical current, which flows along a cylindrical coil parallel to the bore of the magnet. The field strength generated by magnets of this type is also in the range of 0.5T. Superconducting magnets also generate magnetic fields perpendicular to the current, however the field strength is much stronger due to the elimination of resistance by lowering the temperature.

It is absolutely critical for a magnetic field to be uniform, so that the strength will be the same at all points within the sample and all points will resonate at the same frequency. Thus field homogeneity is critical for high quality images. Shimming is the process where by the magnetic field is shaped into a homogenous or less inhomogeneous field. This process involves the application of a shim gradient, which can be adjusted to correct the minor heterogeneities in the main magnetic field.

2.2.1.9 RF Coils

RF coils create the B_1 field, which rotates the net magnetization in a pulse sequence; they also detect the transverse magnetization as it precesses in the x-y plane. RF coils transmit energy with which the spins are manipulated and receive the generated signals. The coils may be either transmit only, receive only, or transmit and receive.

Numerous types of coils exist, and in the experiments described in sections 3.5, both surface and quadrature coils were used. The advantage to using a surface coil is that it detects signal from a smaller area excluding the unwanted or un-needed signals and increasing the overall signal to noise ratio (SNR). In contrast, a quadrature coil both transmits and receives signals. Moreover, signals from both the x and y axes are received and then added together. Coils of this type have been shown to increase the SNR by 41%.

2.3.1 T1-Weighted Imaging

2.3.1.1 T1-Weighted Imaging of Cerebral Ischemia

T1WI has been reported to be sensitive to ischemia as T1 relaxation increases shortly after the onset of the ischemic event (Germano et al., 1989); (Calamante et al., 1999). More recently, (Kettunen et al., 2000) have shown that the early increase in T1 relaxation may be related to the cessation of cerebral blood flow and that increases observed at later time points may be due to edema. Typically, T1WI does not show large changes as a result of ischemia and therefore it is not frequently used.

2.3.1.2 Contrast-Enhanced T1-Weighted Imaging of Cerebral Ischemia

Gadolinium (Gd) enhanced T1 weighted imaging (Gd-T1WI) can be used to study changes in the integrity of the blood-brain-barrier (BBB) as well as cerebral perfusion. Gadolinium is a paramagnetic metal complex that does not normally cross the blood-brain-barrier and shortens the T1 relaxation time via dipole-dipole interactions with neighboring water molecules (van Bruggen et al., 1994); (Kastrup et al., 1999). If there is an increase in blood-brain-barrier permeability, as seen with the reperfusion of ischemic areas, gadolinium can move from the blood vessels into the tissue (Kastrup et al., 1999); (Reith et al., 1995); (Merten et al., 1999). Thus, enhancement within the parenchyma after an ischemic injury suggests that the integrity of the blood-brain-barrier is compromised (Kastrup et al., 1999).

2.3.2 T2-Weighted Imaging

2.3.2.1 T2-Weighted Imaging of Cerebral Ischemia

T2WI reflects the relaxation time of protons within the tissue and is highly sensitive to the state of both free and bound water (Lin et al., 1997). During ischemia, the T2 relaxation time is prolonged in areas with an increase in water content (Pierpaoli et al., 1993); (Lin et al., 1997) perhaps due to vasogenic edema (Gill et al., 1995); (Ueda et al., 1999). In both humans and animal models of ischemia, T2WI can detect vasogenic edema between 6 and 8 hours, which is well in advance of its peak at 24 – 48 hours after onset (Moseley et al., 1990); (Ueda et al., 1999). However, in one study of

focal ischemia, both T2 and T1 relaxation times were found to increase as early as one hour after the ischemic event (Germano et al., 1989).

While the use of T2WI in the detection of cerebral ischemia is often limited to the visualization of vasogenic edema (Moseley et al., 1990), this imaging modality has been reported to detect hemorrhage associated with infarction (Magiera Dunithan et al., 1998); (van Everdingen et al., 1998); (Ebisu et al., 1997). In addition, T2WI is used to determine the size and site of the infarct (van Bruggen et al., 1994); (Biernaskie et al., 2001).

2.3.3 Diffusion-Weighted Imaging

2.3.3.1 Proton Diffusion

Proton diffusion can be defined as the random translational motion of an ensemble of particles (Le Bihan et al., 1986); (Le Bihan, Basser, 1995). The mobility of water molecules is described by a physical constant called the diffusion coefficient, *D,* which is a function of the diffusing molecules as well as the solvent's viscosity and temperature (Le Bihan et al., 1986). This constant is a bulk property dominated by the "free" fraction of water (Hazlewood, 1995). The mean square of the distance covered during diffusion is proportional to time and *D*. For example, the diffusion coefficient for the self-diffusion of water (i.e. water diffusing through water) at 25°C is 2.3×10^{-3} mm^2/sec and the root mean square distance covered in 100 msec in a given direction is 20 μm (Le Bihan et al., 1986).

Diffusion is restricted when either permeable or impermeable boundaries in the medium prevent molecules from moving freely, limiting water to a certain volume. Biological tissues are heterogeneous and contain numerous sub-compartments (e.g. cellular organelles, membranes and myelin sheaths), which impede the movement of water in tissue. Moreover, diffusion may be restricted by the hydration effects where water is bound to macromolecules and is not freely diffusible or bulk phase effects where the physical properties of water are affected by the presence and nature of subcellular surfaces (Hazlewood, 1995). Thus, D will depend on the permeability of the barriers that divide these sub-compartments, the diffusion time and the geometry of the limiting volume (Le Bihan et al., 1986). Molecules within the various sub-compartments of the tissue (i.e. intracellular, extracellular, cell bodies, axons) also have different intrinsic diffusion properties.

Diffusion in the brain is also affected by the tortuosity of the extracellular space. Tortuosity is a dimensionless factor, λ, which accounts for the geometrical constraints imposed by local barriers to diffusion and relates to the both D and ADC via the equation (Helperen et al., 1995):

$$\mathrm{ADC} = D/\lambda^2 \tag{2.6}$$

Tortuosity affects both the time course and magnitude of changes in the extracellular space (Nicholson, 1995). This is particularly important in pathological situations were the swelling of cells reduces the volume of the extracellular space while increasing

tortuosity as the extracellular pathways disappear, ultimately decreasing the diffusion of water through the extracellular space.

2.3.3.2 MR Measurements of Water Diffusion

DWI provides a contrast mechanism for MRI as well as a non-invasive method for measuring the water mobility of tissues *in vivo*. DWI is accomplished by the addition of two gradient pulses to any spin echo sequence (Figure 9; (Le Bihan, Basser, 1995); (Mitchell, 1999). Using the Stejskal-Tanner paradigm, the diffusion gradient is applied in the form of pulses during the dephasing and rephasing parts of the echo sequence (Stejskal, Tanner, 1965).

The first gradient pulse labels the initial position of the water molecules and the second reads the final position of these molecules after they've had time to diffuse. If the water molecules have diffused, the second gradient will be unable to focus the MR signal properly and the image intensity will be reduced. The degree of sensitivity of the water molecules to diffusion is given by the b-value or diffusion gradient strength (Le Bihan et al., 1986) and the larger the b-value, the greater the sensitivity to diffusion (Magiera Dunithan et al., 1998). Since diffusion is not isotropic, the direction of the diffusion gradients can be varied along the x, y, or z directions allowing for the detection of diffusion along the different axes.

The TE and TR are generally long in DWI to accommodate the diffusion gradients, which gives some inherent T2 weighting to the images. As a result, this T2 weighting will change the appearance of the DWI due to T2 shine through (Burdette et al., 1999). To obtain an image that is sensitive to only the changes in diffusion, 2 sets of

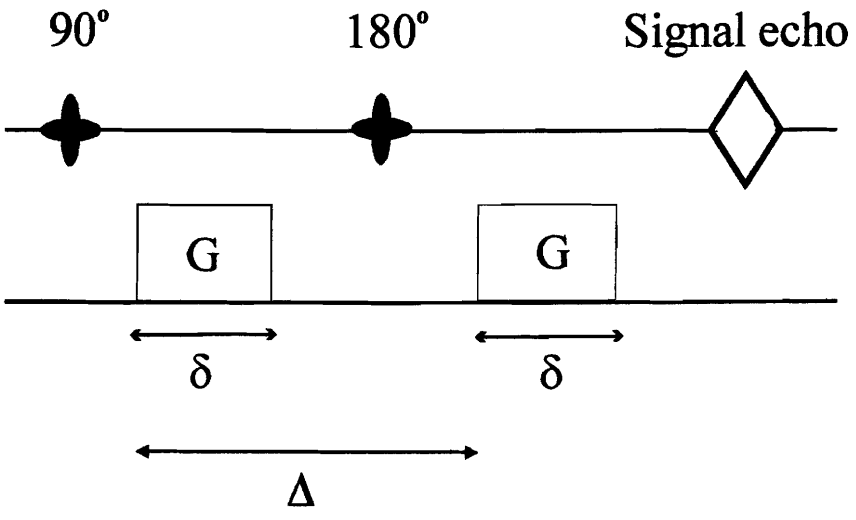

Figure 9: A typical DWI sequence. G is the gradient pulse, δ is the pulse duration and Δ is the pulse separation.

images have to be acquired, one with a b = 0 weighting and the second with a specific b-value. These images are then post-processed into diffusion maps using the Stejskal Tanner equation:

$$ADC = \log (So/Sn)/b \quad (2.7)$$

where ADC is the apparent diffusion coefficient, So is the signal intensity of the un-weighted image, Sn is the signal intensity of the weighted image, and b is the diffusion gradient strength (Le Bihan et al., 1986). DWI is sensitive to all intravoxel incoherent motions, including diffusion, thus instead of *D*, the term ADC is applied (Le Bihan et al., 1986). Typically DWI measurements use a diffusion time of approximately 40 ms, which allows the molecules to displace approximately 10 μm (Beaulieu et al., 1999).

Diffusion maps are used to quantify changes in ADC as areas with a decreased ADC indicate regions of decreased water diffusion (Magiera Dunithan et al., 1998). ADC determinations are most accurate when more than two images, obtained with multiple b-values are used (Le Bihan, 1995), however two point fits have become standard in the field as they provide reasonably accurate ADC values within a minimum imaging time (Xing et al., 1997).

2.3.3.3 Diffusion-Weighted Imaging of Cerebral Ischemia

The biophysical environment of water and its relationship to cell function is of great interest in the study of ischemia. Alterations in cell function; specifically the regulation of cell volume may be reflected in changes to the environment of water and

these changes can then be used to better understand the pathophysiological evolution of ischemia (Helperen et al., 1995).

During ischemia, DWI has been reported to detect the affected areas prior to the onset of vasogenic edema, suggesting that this imaging modality is sensitive to cytotoxic edema with the resultant decrease in ADC the result of alterations in intra- and extracellular fluid volumes (Moseley et al., 1990); (Benveniste et al., 1992); (Busza et al., 1992); (Pierpaoli et al., 1993); (van Gelderen et al., 1994); (Armitage et al., 1998). DWI has demonstrated decreased ADC in the ischemic areas within minutes of an interrupted blood supply (Pierpaoli et al., 1993). As such, DWI is used clinically to detect early ischemic changes when T2 weighted images appear normal (Ueda et al., 1999). Typically, the ADC in sub-acute and acute ischemic brains decreases between 33 – 60% in the first few hours following ischemia, regardless of species (Moseley, Kucharczyk, 1995). This decline is rapid and precedes changes in any other proton MR parameter studied (Helperen et al., 1995); (van Everdingen et al., 1998).

It is generally accepted that the early drop in ADC reflects the bulk slowing of water caused by an accumulation of a more slowly-diffusing intracellular population of water caused by the disruption of the sodium/potassium transmembrane pump or an increase in the number of diffusion barriers such as denaturization of intracellular molecules (Moseley, Kucharczyk, 1995) or changes in the tortuosity of the extracellular environment (i.e. swelling) (Armitage et al., 1998). However, the time course of diffusional changes in acute stroke is also consistent with the complete loss of high energy metabolites (glucose and oxygen) and an increase in extracellular potassium (Busza et al., 1992), suggesting that ADC changes may also reflect tissue metabolism.

Moreover, regions of reduced diffusion have also been matched to areas of acidosis and lactate accumulation (Kohno et al., 1995); (Harris et al., 2000).

While DWI is no doubt useful in the identification of ischemic areas early in the acute periods, diffusion studies are often combined with more conventional T2 weighted or perfusion imaging studies to provide a clearer picture of outcome by examining the tissue for edema and perfusion deficits.

2.3.1.4 Q-Space Imaging (Multiple b-value Diffusion-Weighted Imaging)

Diffusion in the brain is complicated by the fact that there are different diffusing populations contained within an environment of restricted geometries. As a result, the measured ADC becomes a function of a summation of individual diffusion coefficients belonging to different diffusing populations as well as the diffusion time and b-value chosen for the experiment (Assaf, Cohen, 1998). In the low b-value range ($0 - 1 \times 10^6$ s/cm^2), the decay of water signal is mono-exponential and independent of the diffusion time while analysis over an entire range of b-values showed non-bi-exponential signal attenuation of brain water, which was dependent on the diffusion time (Niendorf et al., 1996); (Assaf, Cohen, 1998). At the lower b-values, the mono-exponential diffusion is a weighted average of both the intracellular and extracellular diffusion coefficients (Niendorf et al., 1996), while the bi-exponential diffusion observed at higher b-values ($3.2 - 35.8 \times 10^6$ s/cm^2) reflects the individual contributions of the different diffusing populations (Assaf, Cohen, 1998); (Assaf, Cohen, 2000). It has been suggested that these two populations are in fact a slow and a rapidly diffusing population. Some

investigators suggest that these populations actually represent the intracellular and extracellular components of water (Assaf, Cohen, 2000).

Q-space imaging involves the spatial mapping of diffusion coefficients using a narrow pulsed-gradient spin-echo (PGSE) sequence. In PGSE imaging, the sequence begins with a 90° RF pulse followed by a magnetic field pulse in the x, y, or z direction of duration δ and amplitude G, an 180° pulse, followed by a second identical gradient pulse. The time between the two pulses is the diffusion time, Δ (Szafer et al., 1995). Moreover, narrow diffusion gradient pulses are used in order to neglect motion over the duration of the gradient pulse. Like traditional diffusion experiments, the first gradient pulse imparts a phase shift to the spins, after the 180° refocusing pulse, the shift is inverted and by the second gradient pulse, the spins have moved to their next location. If the spins are stationary, a perfectly refocused echo will occur, but any motion would cause a phase shift in their contribution to the echo, resulting in reduced signal intensity (Callaghan, 1995).

The q-space theory describes diffusion measurements in terms of displacement probabilities, using the reciprocal spatial vector, q, which is defined as:

$$q = (\gamma \delta g)/2\pi \tag{2.8}$$

where γ is the gyromagnetic ratio, δ is the duration of the gradient pulse and g is the magnitude of the gradient (Kuchel et al., 1997); (Assaf, Cohen, 2000). The magnitude of this vector, q, controls the echo intensity decay for displacements.

Q-space is important as it provides important physiological information on water mobility, compartmentation and structural anisotropy (Neeman et al., 1995). Specifically, changes in the mean square displacement and loss of signal intensity with increased diffusion time can be used to determine restricted diffusion, fractal diffusion and random Brownian diffusion in normal and diseased or injured tissue (Neeman et al., 1995).

3.0 Specific Aims and Hypothesis

Imaging modalities can clearly identify the areas affected by ischemic insults, however, the underlying tissue alterations remain unknown. The ability to non-invasively characterize and quantify changes in brain edema and pathology with morphology is critical in understanding ischemic pathophysiological processes. The goals of this research were:

1) To determine the temporal and spatial evolution of a permanent focal ischemic lesion induced by cortical devascularization. The subsequent pathophysiological changes were observed using DWI, T2WI, and Gd-T1WI as well as correlative cresyl violet histochemistry.
2) To determine the glial activation pattern and extent of an inflammatory response after cortical devascularization. These changes were observed using immunocytochemical and ELISA methods.
3) To determine if delayed neuronal death and post-injury inflammation could be prevented by treatment with APTRA-AM. These changes were observed by histochemical and immunocytochemical methods.
4) To determine if the ADC changes typically associated with a cortical devascularization injury could be inhibited by treatment with APTRA-AM. This was assessed using multiple b-value DWI.

We hypothesized that diffusion weighted imaging would be able to accurately detect the temporal and spatial evolution of pathological changes after cortical devascularization. Moreover, we predicted that the changes observed by DWI, T2WI and Gd-T1WI would accurately reflect the morphological changes observed by histology and immunocytochemistry, allowing us to correlate specific physiological events to changes in diffusion.

Once the model was characterized, we studied the neuroprotective effect of the cell permeant calcium buffer, APTRA-AM. While the neuroprotective properties of APTRA-AM have been demonstrated against early *in vitro* glutamate-induced excitotoxicity and against *in vivo* focal cerebral ischemia (Tymianski et al., 1994) we hypothesized that this molecule would also be neuroprotective if given after a permanent ischemic insult. Moreover, we felt that if APTRA-AM prevented neuronal cell death, it may also block the glial activation and inflammation typically associated with this type of injury. Finally, if APTRA-AM proved to prevent the cell death, glial and inflammatory responses, it should also suppress any MRI sensitive (i.e. diffusion) changes to the tissue.

4.0 Materials and Methods

4.1 Animal Model

A small focal permanent ischemic lesion was created in the right frontal cortex of male Wistar rats (250–300g; from a colony maintained by the Department of Anatomy and Cell Biology, University of Saskatchewan, Saskatoon, Canada or Charles River, Hollister, CA) using a modification of a cortical devascularization technique (Berezovskaya et al., 1996). To create the lesion, a midline incision was made over the skull and a 2.3 mm hole was drilled through the skull 2 mm anterior and 1 mm lateral to Bregma (Figure 10). The dura was removed, exposing the pial vasculature and a single descending pial vessel was transected. Once bleeding stopped, residual blood was washed from the area using phosphate buffered saline and the wound was then closed in discontinuous silk suturing. In the initial experiments, anesthesia was induced using a mixture of ketamine (125 mg/kg, i.p., J.A. Webster, Sterling, MA; K836) and xylazine (10 mg/kg, i.p., J.A. Webster, Sterling, MA; 560680) while later experiments used isofluorane (J.A. Webster, Sterling, MA; 634705) inhalation (3% for induction, 1.5% for maintenance).

Sham-operated control animals underwent a similar surgical procedure that involved a craniotomy followed by the removal of the dura, exposure of the pial vessels but without the vessel transection. All procedures conformed to animal care regulations

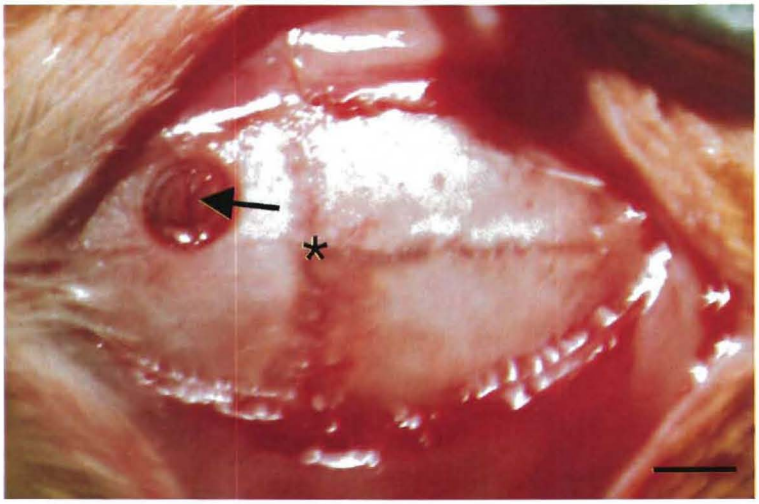

Figure 10: Photograph of a rat's skull showing the placement of the craniotomy relative to Bregma (asterisk). A large pial vessel can be seen traversing the hole (arrow). Scale bar = 2 mm.

and were approved by both the University of Saskatchewan and Loma Linda University Animal Care Review Committees.

4.2 Magnetic Resonance Imaging

4.2.1 MRI Acquisition at 1.5T

The initial DW and T2W MRI experiments were performed at the University of Saskatchewan using a Siemens 1.5T SP Magnetom with a 150 mm-diameter Helmholtz surface coil (Figure 11A). Animals underwent light anesthesia with ketamine (90 mg/kg, i.p.) and xylazine (10 mg/kg, i.p.). After slice positioning, a spin echo diffusion imaging sequence (TR = 2200 ms, TE = 111 ms, b = 0, b = 12819 s/cm^2, δ = 32 msec) and a 16 echo T2 sequence (TR = 2000 ms, TE = 20 - 245 ms) were run. Seven coronal slices, each 2 mm thick and interleaved by a 2 mm separation, with a 50 mm field of view and a matrix size of 128 x 128 were collected for each sequence. Two averages were used to increase the signal to noise ratio of the images.

A total of thirty-seven animals were used in this study (see section 8.1 for details). The animals were scanned before surgery ('prescan') and then at 12, 24, 48 hours, 3, 5, 7 and 14 days after surgery. These time points were chosen after preliminary experiments that showed no significant change in signal intensity prior to 12 hours. In order to correlate histological changes with the individual time points, three animals were culled from the temporal imaging study at each of the eight time points.

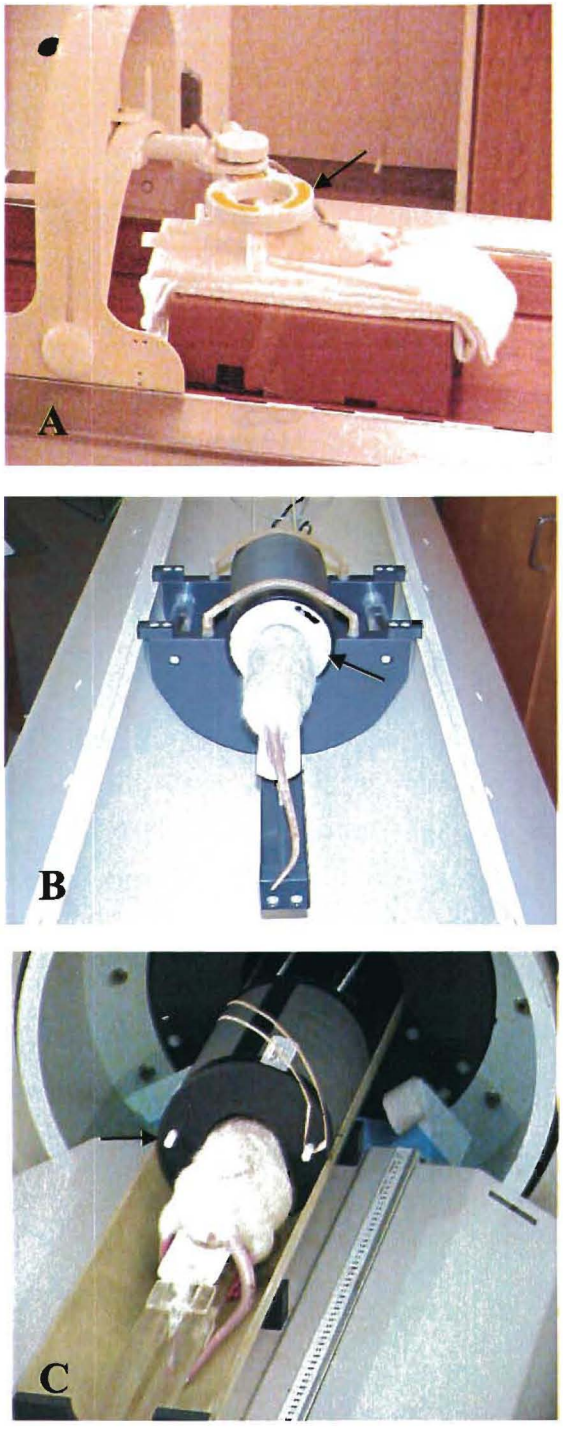

Figure 11: The placement of a rat in the Helmholtz surface coil used at 1.5T (A), the quadrature coil used at 3.0T (B) and the quadrature coil at 4.7T (C).

4.2.2 MRI Acquisition at 3.0T

To determine if the cortical devascularization resulted in an increase in blood brain barrier permeability, 7 animals underwent a gadolinium (Gd; ProHance™ gadoteridol; Bracco Diagnostics, Mississauga, ON; J4-639) enhanced T1 weighted (Gd-T1WI) study (see section 8.1 for details). All animals had tail vein catheters in place prior to imaging. This data set was collected at the University of Saskatchewan on a SMIS (Surry Medical Imaging Systems, England) 3.0T magnet with a 50 mm quadrature RF coil (Morris Instruments, Ontario; Figure 11B). Animals were anesthetized using isofluorane inhalation (3% for induction, 1.5% for maintenance). After slice positioning, a pre-contrast T1 weighted sequence was performed (TR = 650 ms, TE = 20 ms). Ten coronal slices, each 1.5 mm thick and interleaved by a 1.5 mm separation, with a 40 mm field of view and a matrix size of 128 x 128 were collected. Two averages were used to increase the signal to noise ratio of the images. Following this acquisition, the contrast agent was injected via a tail vein catheter (0.3 mmol/kg); followed by a series of T1 weighted sequences (using the same parameters) performed continuously over the next 30 minutes. Each animal was imaged prior to and then again at 1, 2, 3, and 7 days after surgery. Both pre- and post-contrast images were collected at each time point.

4.2.3 MRI Acquisition at 4.7T

Q-space (multiple b value) diffusion weighted imaging was used to study diffusional related changes in injured animals after receiving saline, dimethyl sulfoxide (DMSO) or APTRA-AM injections. This data was collected at Loma Linda University

on a Bruker (Billerica, MA) 4.7T magnet with a 50 mm quadrature RF coil (Figure 11C). Animals were anesthetized using isofluorane inhalation (3% for induction, 1.5% for maintenance) and after slice positioning, a T1 weighted sequence was performed (TR = 750 ms, TE = 20 ms) followed by a DWI sequence (TR = 3000 ms, TE = 20 ms, b = 19, 100, 350, 738 s/mm^2, δ = 32 ms). Twelve coronal slices, each 1.5 mm thick and interleaved by a 1.5 mm separation, with a 45 mm field of view and a matrix size of 256 x 256 were collected. Two averages were used to increase the signal to noise ratio of the images.

A total of 23 animals were used in this study (see section 8.1 for details) and the animals were imaged before surgery ('prescan') and then at 12, 24, 48 hours, and 7 days after surgery.

4.2.4 MRI Analysis

To quantify changes in the diffusional motion of water due to the devascularization injury, diffusion weighted maps were generated from the 1.5T images using an in-house program and the apparent diffusion coefficient (ADC, cm^2/s) calculated for each pixel using the Stejskal Tanner equation (see equation 2.7). It should be noted, that the un-weighted (b = 0) image is essentially a T2 weighted image owing to its long TR and short TE.

To quantify the changes in the overall water content after the surgery, T2 maps were generated from the 16 echo sequences obtained at 1.5T and the relaxation constants were calculated for each pixel using nonlinear least squares curve fit to the data using the equation,

$$M(t) = Mo\ (e^{t/T2}) \qquad (3.2)$$

where Mo is the initial magnetization before decay, t is the echo time (ms) and T2 is the spin-spin relaxation time (ms).

Region of interest (ROI) analysis of the 1.5T diffusion and T2 maps were done using Cheshire™ image processing software (Hayden Image Processing Group, Waltham, MA). Two ROIs were manually drawn on the DW and T2 maps; region one was located in the cortex immediately inferior to the surgery site (the "lesion") and region two was located in the homologous cortical area on the contralateral side (Figure 12). Each ROI contained an area of 3 pixels by 3 pixels, with a pixel size of 352 μm. Both regions were located in the primary motor cortex (frontal area 1, Fr1). On the DW maps, a mean ADC (± standard error of the mean (SEM)) was calculated for each region of interest and a mean T2 relaxation time (± SEM) was generated using the T2 maps. Differences in the means of both these tissue properties were compared across time points using a repeated measures one way ANOVA followed by individual Student-Newman-Keuls comparisons (Sigma Stat™, SPSS Inc., New York, NY) for statistical significance ($p<0.05$; highly significant at $p<0.01$). The difference in ADC or T2 relaxation between both hemispheres was analyzed for statistical significance ($p<0.05$; highly significant at $p<0.01$) using a Student's t-test.

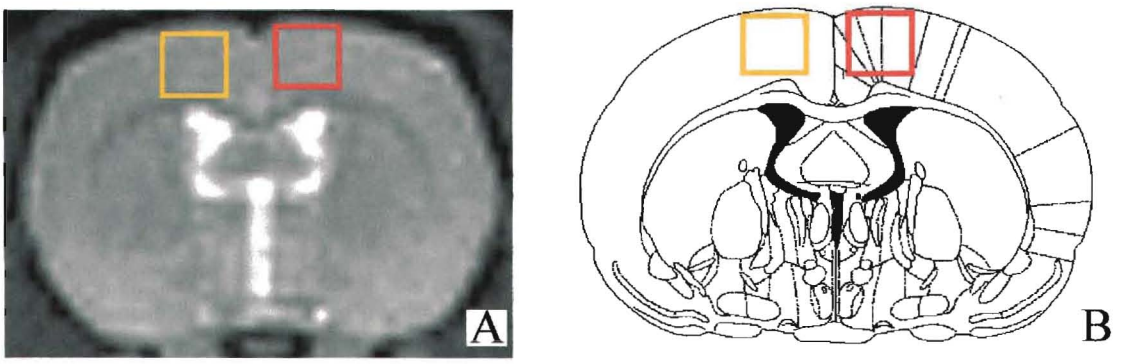

Figure 12: Regions of interest selected for the quantification of ADC. The un-weighted (b = 0) image (A) shows the location of the ROIs and the atlas (Paxinos and Watson, 1998) image (B) shows the location of the ROIs in the primary and association motor cortices of both hemispheres.

ROI analysis in the q-space DWI experiments was done using the Image Sequence Analysis tool, which is part of the ParaVision 2.1.1 software package (Bruker; Billerica, MA). The ROI were located in the same areas as the original diffusion maps (see Figure 12), however the size of the ROI differed slightly owing to the difference in pixel size (176 μm). In this data set, ADC maps were not generated for the ROI analysis instead; the ADCs of the ROI were calculated manually from the mean signal intensities using equation 2.7. Three ADCs were calculated for each animal at each time point, the first using b = 19 s/mm^2 and b = 110 s/mm^2, the second using b = 19 s/mm^2 and b = 350 s/mm^2 and the third using b = 19 s/mm^2 and b = 738 s/mm^2.

The differences in the mean ADC at each b-value were compared across time points using a repeated measures one way ANOVA followed by individual Student-Newman-Keuls comparisons (Sigma Stat™, SPSS Inc., New York, NY) for statistical significance ($p<0.05$; highly significant at $p<0.01$). Differences in the mean ADC of the lesion ROI were also compared across the different treatment groups using the same statistical analysis. A Student's t-test was used to determine if the ADC of the lesion and contralateral ROI were significantly different ($p<0.05$; highly significant at $p<0.01$).

In the Gd-T1WI study, analysis was done by visually inspecting the post-contrast images for the presence of contrast within the tissue parenchyma.

4.3 Tissue Analysis

4.3.1 Fixation and Tissue Processing

Rats were anesthetized using a mixture of ketamine (125 mg/kg, i.p.) and xylazine (10 mg/kg, i.p.) and perfused transcardially with 4% paraformaldehyde in 0.12mM Millonig's buffer (see section 8.2.2.1) at selected time points after injury or treatment. The brain was left *in situ* and refrigerated for one hour, after which time it was removed and placed in 4% paraformaldehyde for 1 hour. Following this, 3, 30 minute rinses in 0.12 mM Millonig's buffer (see section 8.2.1.2) were done and the rinsed brains then placed in a 30% sucrose solution (see 8.2.2.2) until they sank. The brain was blocked into 3 sections (cerebellum, frontal cerebrum, and rostral cerebrum), coated in OCT Compound (Tissue Tek™, Fisher Scientific, Tustin, CA; 1-437-365) and quick-frozen over dry ice. Frozen tissue was stored at –80°C until processed. Sections (30 μm) were cut using a cryostat set at – 20°C and every 10^{th} section was mounted on gel-chrome-alum coated slides. Tissue not mounted was placed in a 1.5 ml microcentrifuge tube containing a cryoprotectant solution (see section 8.2.2.3). This archived tissue was stored at 4°C until processed.

4.3.2 Light Microscopy

4.3.2.1 Cresyl Violet Histochemistry

To ascertain the amount of damage caused by the cortical devascularization, mounted slides were then stained with cresyl violet acetate. Briefly, sections were

dehydrated in two 5-minute changes of 95% alcohol, followed by the removal of lipids in chloroform – ether solution (see section 8.2.3.1.2) for 15 minutes. The sections were then rehydrated through descending concentrations of alcohol with a final rinse in distilled water. Slides were then placed in 0.1% cresyl violet acetate (see section 8.2.3.1) for 10 minutes followed by 2 rinses in distilled water and a brief clearing in acetic formalin (see section 8.2.3.1.3). The slides were then rinsed in 2 changes of distilled water and dehydrated through ascending concentrations of alcohol, followed by a final clearing in 3 changes of Histoclear™ (National Diagnostics, Atlanta, GA; H5200).

4.3.2.2 Measurement of Lesion Area

The area (mm^2) of the infarct was determined by computerized planimetery of the maximal area of damage (defined as tissue rarefaction, vacuolation, necrosis and edema) observed on cresyl violet stained sections at a magnification of 200X. Measurements were made using the Computer Assisted Stereological Toolbox - Grid system (C.A.S.T.- Grid; Albertslund, Denmark) and the data expressed as mm^2. The resultant traces of the infarct area were constructed of a series of straight lines drawn at the edge of the infarct. The start and end points were connected by a straight line to approximate the surface of the brain (Figure 13).

Three sections from each time point were analyzed, as were sections from each animal included in the neuroprotection study (see section 8.1 for details). The individual area measurements from each animal were pooled and expressed as mean lesion area (mm^2). Differences in mean lesion area (± SEM) were compared across the different

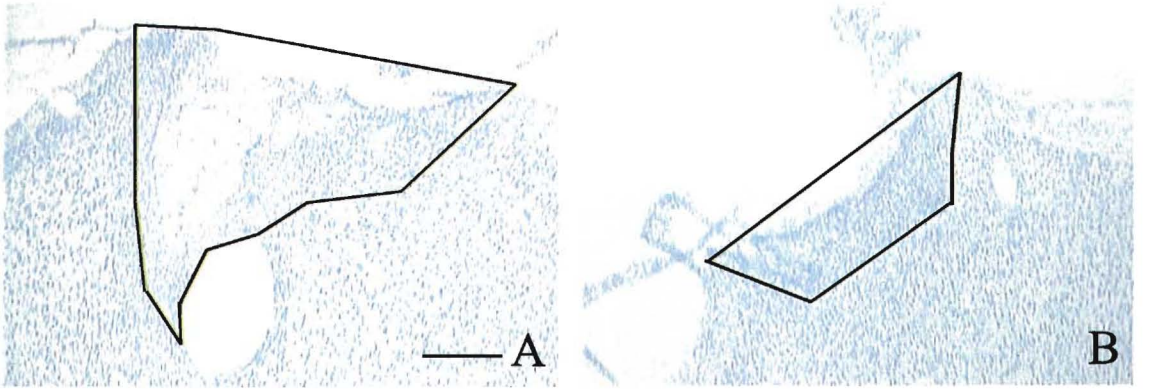

Figure 13: Two representative photomicrographs of a lesion following cortical devascularization (A) and after APTRA-AM treatment (B). Images show the delineation of the two dimensional area used to calculate lesion area. Scale bar = 100 μm.

time points using a repeated measures one way ANOVA followed by individual Student-Newman-Keuls comparisons for statistical significance ($p<0.01$). For the data collected from the neuroprotection study, differences in the lesion area (± SEM) at 7 days after the different treatments were compared using a ranked sum ANOVA followed by Dunn's method of pairwise multiple comparisons (significance $p<0.01$; Sigma Stat™, SPSS Inc., New York, NY).

4.3.2.3 Immunocytochemistry

Sections through the lesion were selected for immunocytochemical analysis (see section 8.1 for details). Neurons were identified using a mouse anti-neuronal nuclei (NeuN, 1:1000; Chemicon International, Temecula, CA; MAB377) monoclonal antibody. Glial subpopulations, astrocytes and microglia, were identified using a rabbit anti-glial fibrillary acidic protein (GFAP, 1:500; DAKO, Carpinteria, CA; Z0334) and a mouse anti-CD11b (OX-42, 1:250; Serotec, Raleigh, NC; MCA275R) primary monoclonal antibody, respectively. Phagocytic cells were identified with a mouse anti-ED1 primary monoclonal antibody (1:400; Serotec, Raleigh, NC; MCA341R). NF-κB activation was identified using a mouse anti-NF-κB p65 subunit primary monoclonal antibody (1:500; Roche Molecular Biochemicals, Indianapolis, IN; 1-697-838). This NF-κB antibody was chosen as it recognizes an epitope within the nuclear translocation signal of the p65 subunit, thus it selectively stains a released and activated form of NF-κB (Zabel.U. et al., 1993).

Sections were washed twice in phosphate buffered saline (PBS) and placed in a 12 well culture plate with one section per well. The sections were blocked in 5% horse

serum (Vector Laboratories, Burlingame CA; S2000), 1% bovine serum albumin (BSA, Sigma-Aldrich, St. Louis, MO; A9647), and 1% Triton-X-100 (Sigma-Aldrich, St. Louis, MO; T9284) and incubated in one of the primary antibodies diluted in PBS containing 5% horse serum, 0.1% BSA and 0.1% Triton-X-100 overnight at 4°C. The next day, sections were washed, incubated with a biotinylated universal antibody (Vectastain Universal Elite ABC kit, Vector Laboratories, Burlingame CA; PK6200) for 1 hour at room temperature, quenched with 3% H_2O_2, washed again, incubated with avidin-peroxidase (Vectastain Universal Elite ABC kit, Vector Laboratories, Burlingame CA; PK6200) for 1 hour, and colored by diaminobenzidine (DAB, Sigma-Aldrich, St. Louis, MO; D8001). Finally, sections were rinsed in distilled water, mounted on gel-chrome-alum coated slides and dried on a slide warmer set at 37°C. Control sections for non-specific staining were prepared by the omission of the primary antibody.

4.3.3 Fluorescent Microscopy

4.3.3.1 Immunocytochemistry

A number of sections were selected for fluorescent double-labeled immunocytochemistry to determine where the pro-inflammatory cytokines, TNF-α and INF-γ co-localized (see section 8.1 for details).

Briefly, sections were washed twice in PBS and placed in a 12 well culture plate with one section per well. The sections were blocked in 5% horse serum, 1% bovine serum albumin, and 1% Triton-X-100 for 15 minutes and then incubated in two of the primary antibodies diluted in PBS containing 5% horse serum, 0.1% BSA and 0.1%

Triton-X-100 overnight at 4°C. Primary antibodies used included GFAP (1:500), OX-42 (1:250), ED1 (1:400), a rat anti-TNFα (1:500; R&D Systems, Minneapolis, MN; AF-510-NA) and a rat anti-IFN-γ (1:500; R&D Systems, Minneapolis, MN; AF-585-NA) monoclonal antibody. The next day, sections were washed 4 times in PBS and incubated with two of either Texas Red® anti-rabbit IgG, fluorescein anti-rabbit IgG, Texas Red® anti-rat IgG, fluorescein anti-mouse IgG, or Texas Red® anti-goat IgG (diluted at 1:200; Vector Laboratories, Burlingame CA; TI-1000, FI-1000, TI-9400, FI-2000, TI-5000), for 1 hour at room temperature. Sections were then washed 4 times in PBS, mounted on gel-chrome-alum coated slides, dried on a slide warmer set at 37°C and mounted with Vectashield™ mounting media containing 4', 6-diamidino-2-phenylindole, dihydrochloride (DAPI) (Vector Laboratories, Burlingame CA; H-1200). Control sections were prepared by the omission of the primary antibodies.

4.3.3.2 Fluoro-Jade™ Staining

Sections both preceding and adjacent to the cresyl violet and immunocytochemically stained slides were stained with Fluoro-Jade™ (Histo-Chem Inc., Jefferson AZ) to identify the presence and location of degenerating neurons (see section 8.1). Briefly, sections were rinsed in distilled water, mounted on gel-chrome-alum coated slides, and dried on a slide warmer set at 60°C. After drying, the slides were rehydrated in 80% alcohol containing 1% NaOH, 70% alcohol and distilled water. The slides were then incubated in 0.06% potassium permanganate followed by a distilled water rinse and subsequent incubation in Fluoro-Jade diluted in 0.1% acetic acid. Finally, the slides were washed 3 times in distilled water, dehydrated in xylene, and mounted with DPX

(Fluka, St. Louis, MO; 44581). The sections were observed using a fluorescein/fluorescein-5-isothiocyanate (FITC) filter system.

4.4 Neuroprotection Study

A histological study was undertaken to assess the neuroprotective effects of APTRA-AM. Rats were randomly assigned to five treatment groups (see section 8.1 for details): 1) ischemia with no treatment, 2) ischemia with saline (0.9% NaCl), 3) ischemia with vehicle (1% DMSO (Sigma-Aldrich, St. Louis, MO; D2650) in 0.9% NaCl), 4) ischemia with APTRA-AM (40 mg/kg in 1% DMSO; Molecular Probes, Eugene OR; A6896), and 5) sham-surgery with no drug treatment. All treatments were administered intravenously via tail vein injection. For each injection, a total volume of 3 mL was administered over 15 minutes using an infusion pump set at a flow rate of 0.2 ml/min (Harvard Apparatus, Holliston, MA). Each animal received two injections, the first at 1 hour after injury and the second 12 hours after injury. This regimen was chosen based on previous findings that intravenous APTRA-AM reduced evoked potentials in the rat hippocampus *in vivo,* an effect that was maximal 6 hours after infusion with return to baseline by 24 hours (Spigelman et al., 1998). Moreover, since neuronal death appears to occur with a delay of about 48 hours after cortical devascularization (Bartnik et al., 2001) we reasoned that optimal neuroprotection might be achieved with a double dose regimen. Seven days after injury and treatment, the animals were sacrificed for subsequent histological and stereological analysis.

4.5 Enzyme Linked Immunosorbent Assay (ELISA)

Three, 6, 12, 24, 48 hours and 3 days following cortical devascularization or sham operation, rats (see section 8.1 for details) were euthanised using 100% CO_2 asphyxiation and the ischemic infarct and contralateral homologous cortical areas were rapidly removed and snap frozen in liquid nitrogen. The tissue was homogenized in 50 µl of PBS/Protease Inhibitor Cocktail (Calbiochem-Novabiochem, San Diego, CA; 539134) for every 10 mg wet weight. The samples were then centrifuged at 10,500 *g* at 4°C for 15 minutes and the supernatant aliquoted. A quantitative sandwich ELISA technique was used to quantitatively ascertain the amount of these inflammatory cytokines produced as a result of the cortical devascularization.

Briefly, a 96-well Microwell plate (NUNC Maxisorb™, Fisher Scientific, Tustin, CA; 12-565-210) was coated with a 100 µl of the capture antibody (either anti-rat TNF-α or anti-rat INF-γ) diluted in coating buffer, the plate sealed and incubated overnight at 4°C. After incubation, the plate was washed five times in wash buffer, followed by blocking with assay diluent at room temperature for one hour. The plates were then washed five times with the wash buffer and 100 µl of sample or standard (recombinant rat TNF-α or IFN-γ) was loaded into each well and incubated for 2 hours at room temperature. Following this incubation, the plates were again washed 5 times with wash buffer, incubated with detection antibody (biotinylated anti-rat TNF-α or anti-rat IFN-γ, 1: 250) for one hour at room temperature. The wells were washed again and 100 µl of avidin-horseradish peroxidase conjugate (diluted 1:250) added to each well and incubated for 30 minutes at room temperature. After incubation, the plates were washed five times and incubated in 3, 3-, 5, 5-tetramethylbenzidine (TMB) substrate in the dark

for 30 minutes. To stop the reaction, 50 mL of 2N H_2SO_4 was added to each well and the absorbance read at 450 nm. The amount of cytokine present was normalized to the amount of tissue analyzed and expressed as pg/mL. All the reagents and antibodies used in these experiments were supplied with the OptEIA™ rat TNF-α (558870), OptEIA™ rat IFN-γ (558861), and reagent set B (550534) kits (Pharmingen, San Diego, CA).

The mean concentration of each cytokine (in pg/mL ± SEM) was calculated for each of the ROIs and differences in the cytokine concentration of each region were compared across time points using a repeated measures one way ANOVA followed by individual Student-Newman-Keuls comparisons (Sigma Stat™, SPSS Inc., New York, NY) for statistical significance ($p<0.05$; highly significant at $p<0.01$).

5.0 Results

5.1 Cortical Devascularization: A Model of Permanent Focal Ischemia

The cortical devascularization model used in the following studies produces a well-circumscribed, small, permanent cortical ischemic lesion that develops slowly. All animals undergoing this procedure developed a lesion of similar size and severity. Specifically, the lesion in each animal was well circumscribed; never extending inferiorly beyond the corpus callosum and contained within 600-1500 μm of tissue. Only occasionally was blood found within the infracted region.

Previously, this model has been used to study choline acetyltransferase activity in the nucleus basalis (Stephens et al., 1985), the effect of injury on glial cells (Herrera, Cuello, 1992), the effect of colony stimulating factor-1 on neuronal survival (Berezovskaya et al., 1996) as well as lesion-induced changes in nerve growth factor levels (Conner et al., 1998). Despite its previous use, we are the first to characterize the temporal evolution of neuronal damage, glial changes, and post-injury inflammation. Moreover, we are the first to publish the MR changes associated with an injury of this type (Bartnik et al., 2001).

5.1.1 Temporal Evolution of Infarct Development: MR Changes

5.1.1.1 Diffusional Changes at 1.5T

Hyper-intense regions in DW images define areas where water mobility is relatively restricted resulting in decreased ADC values (Moseley et al., 1990). The converse is also true, where hypo-intense regions correspond to areas of increased ADC. Control (un-injured) animals and all prescan images showed consistent patterns of water mobility, with the ventricles and interstitial regions exhibiting the highest mobility. However, intensity changes in diffusion were observed after the cortical devascularization on the ipsilateral side of the brain (Figure 14), which were quantified by calculating the ADC for each region of interest.

The ADC isolates the diffusional effects from the influence of T2 changes specifically the quantity of water and its intrinsic relaxation rate properties (Moseley et al., 1990). Comparison of the mean ADC of the lesion area before and after treatment revealed significant ($p<0.05$) ADC reductions at 12, 24, 48 hours as well as 3 and 5 days (Figure 15). The most significant decrease in ADC occurred at 12 hours after injury, when the ADC of the lesion area had decreased to 67.5% of the prescan value (Table 1). The ADC of the lesion area remained below 80% of the prescan value until 7 days after injury (Table 1). By 7 days the ADC had recovered to 80% of the prescan value (not significant) and at 14 days the ADC had returned to prescan values (Table 1). In addition, a significant ($p<0.05$) difference in ADC within the corresponding

Figure 14: Representative diffusion un-weighted (b = 0; first column) and weighted (b = 12819 s/cm^2; second column) MR images at 1.5T of animals sampled from control (A, B) and 12 hours (C, D), 24 hours (E, F), 48 hours (G, H), 7 days (I, J), 14 days (K, L) after cortical devascularization. Both the un-weighted and weighted diffusion images are typical for the control (A, B) group. The weighted image (B) has the brain outlined in black. A region of increased signal intensity corresponding to the lesion area (arrow) is observed at both 12 (D) and 24 hours (F). After 48 hours, the un-weighted image shows a decrease in signal intensity in the area corresponding to the lesion (G, arrow) which continues into the 7 day time point (I, arrow) while the corresponding diffusion weighted images show increased signal intensity in the lesion area (H, J). By 14 days, both the un-weighted (K) and weighted images (L) are similar to the control group. Scale bar = 1 cm.

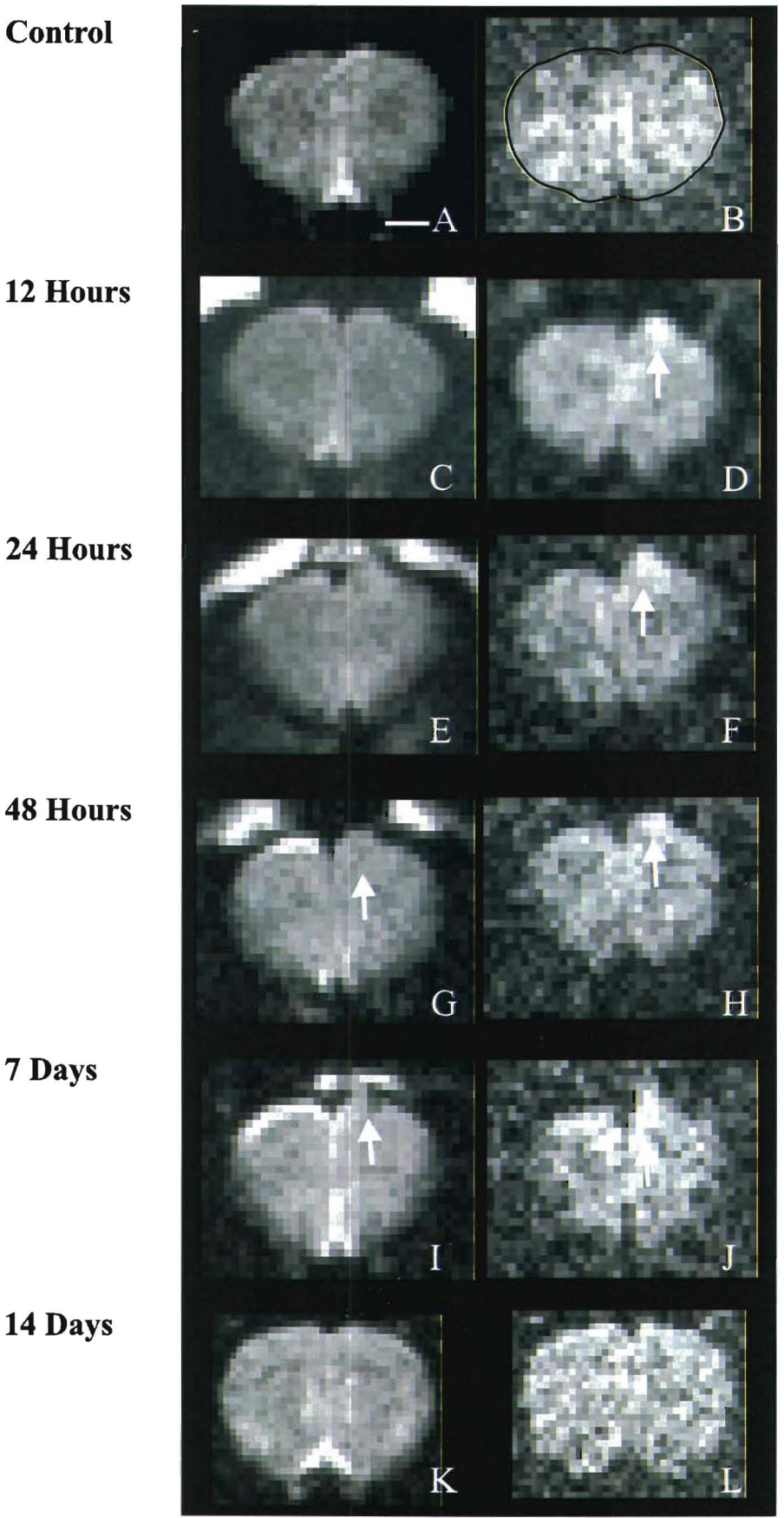
Control
A
B
12 Hours
C
D
24 Hours
E
F
48 Hours
G
H
7 Days
I
J
14 Days
K
L

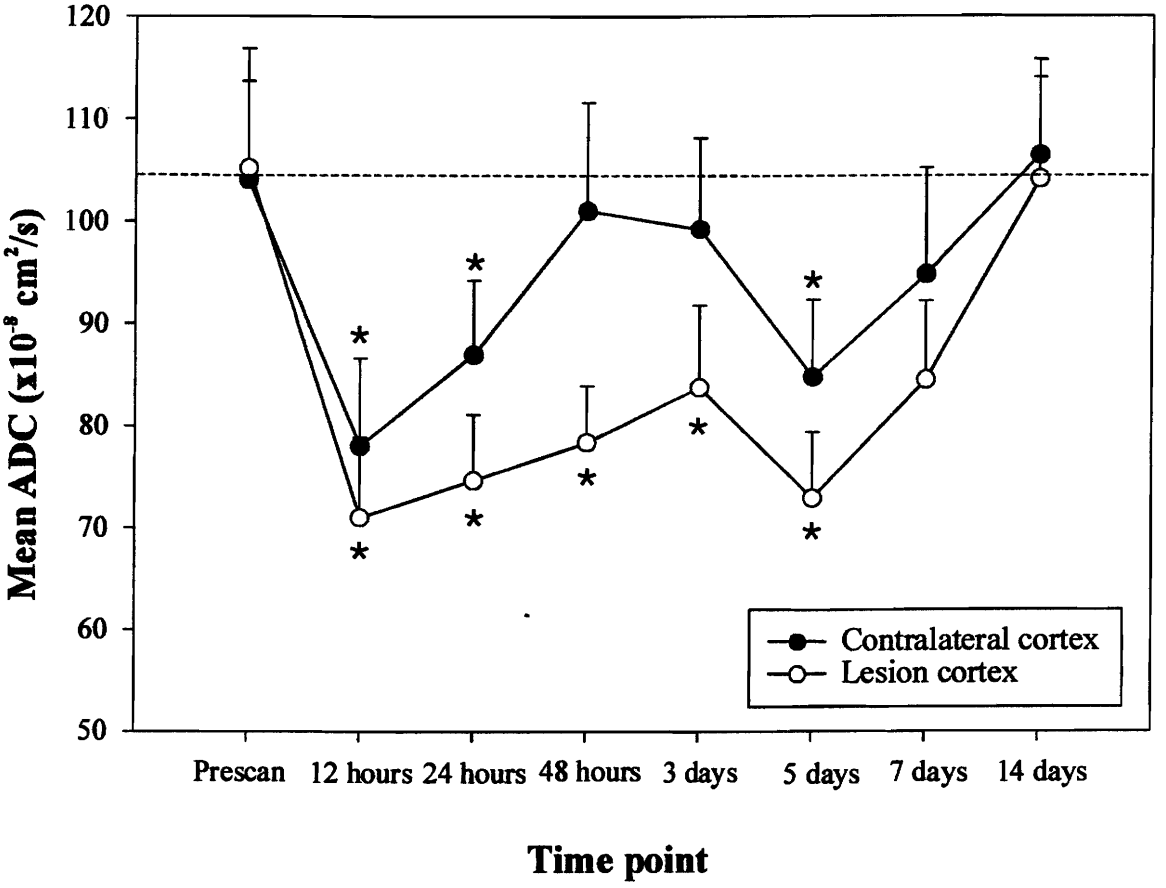

Figure 15: Mean ADC (cm^2/s, ± SEM) versus observation time of the contralateral and lesion (ipsilateral) regions of interest (ROI). An asterisk denotes a significant ($p<0.05$) difference in the ADC of the lesion ROI at 12, 24, and 48 hours, 3 and 5 days after injury when compared to the same area of the animals images prior to surgery (prescan). A significant decrease in ADC was also observed in the contralateral ROI at 12, 24 hours and 5 days after injury when compared to the identical ROI in the prescan images.

Table 1: Quantitative evaluation of the mean ADC (± SEM) and T2 relaxation time (± SEM) in the lesion and homologous contralateral region of interest in devascularized animals. [1]

		Mean ADC (± SEM) (x 10^{-8} cm^2/s)			T2 relaxation time (± SEM) (ms)		
Observation Time	**Histology (n)**	**Lesion side**	**Contralateral side**	**n**	**Lesion side**	**Contralateral side**	**n**
Prescan	3	105.21 ± 11.64	104.03 ± 9.64	23	105.20 ± 6.17	108.84 ± 11.36	23
12 hours	4	71.05 ± 7.84*	78.08 ± 8.52*	5	99.15 ± 2.28	96.50 ± 5.79	5
24 hours	4	74.69 ± 6.42*	87.00 ± 7.23*	8	92.01 ± 5.73	92.42 ± 4.73	8
48 hours	4	78.44 ± 5.48*	101.05 ± 10.55	8	95.31 ± 7.45	102.13 ± 9.02	5
3 days	4	83.80 ± 8.01*	99.25 ± 8.88	6	85.54 ± 2.23	88.83 ± 7.10	6
5 days	4	72.95 ± 6.47*	84.80 ± 7.54*	7	85.96 ± 3.38	106.84 ± 8.88	8
7 days	4	84.52 ± 7.68	94.81 ± 10.39	6	95.73 ± 8.59	100.78 ± 15.39	5
14 days	5	104.11 ± 9.90	106.43 ± 9.34	5	87.38 ± 8.00	91.45 ± 10.15	5

[1]Values in a column followed by asterisk are significantly different from the prescan value at the 5% level according to a repeated measure one-way ANOVA followed by individual Student-Newman-Keuls comparisons.

contralateral region at 12, 24 hours and 5 days (Figure 14) were also observed, with the largest reduction (75%) observed at 12 hours after injury (Table 1).

A representative DWI from the sham data set at 3 days post surgery is illustrated in Figure 16. Quantitative analysis did not detect a significant difference in ADC compared to the pre-scan values (Table 2).

5.1.1.2 T2 Changes at 1.5T

Signal intensity in T2W images (T2WI) is indicative of proton relaxation time and is considered a putative marker for vasogenic edema. An increase in signal intensity corresponds to areas with an increased relaxation time. As the un-weighted (b = 0) image is essentially a T2 weighted image owing to its long TR and short TE, the first column of Figure 14 is used to illustrate the T2 changes. Prior to surgery (prescan), no regions of altered signal intensity existed indicating that the anesthesia also had no effect on T2 relaxation time (Figure 14 A). After injury, slight changes in signal intensity were observed on the MR images at 24, 48 hours and 7 days (Figure 14 E - I). Statistical analysis indicated that these changes were not significant (Table 1). Animals in the sham group also showed a slight decrease in the signal intensity in the area inferior to the surgery site (Figure 16 A) however; statistical analysis indicated that the change in T2 relaxation time was not significant.

5.1.1.3 Contrast-Enhanced T1 Changes at 3.0T

The use of paramagnetic contrast agents to study blood-brain-barrier permeability has been well documented. It is generally accepted that an accumulation of

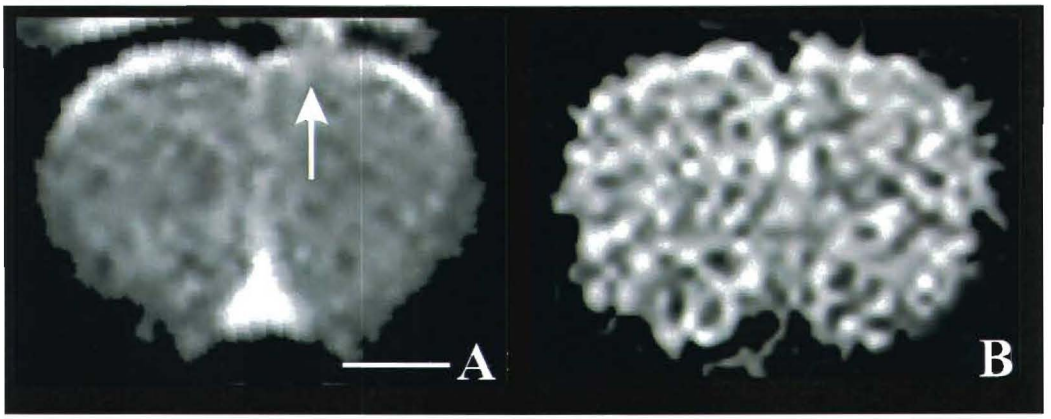

Figure 16: Representative diffusion un-weighted (A) and weighted MR (B) images of a sham animal 3 days after surgery. The un-weighted diffusion image shows a slight decrease in signal intensity in the area corresponding to the surgery site (A, arrow). The diffusion-weighted image shows no change in signal intensity between the area inferior to the surgery site and the matching contralateral region (B). Scale bar = 1 cm.

Table 2: Mean ADC (± SEM) of the ipsilateral and contralateral region of interest in the sham animals.

	Mean ADC (± SEM) (x 10^{-8} cm^2/s)			T2 relaxation time (± SEM) (ms)		
Observation Time	**Lesion side**	**Contralateral side**	**n**	**Lesion side**	**Contralateral side**	**n**
Prescan	109.50 ± 4.17	104.04 ± 5.96	9	107.21 ± 17.30	98.27 ± 7.50	8
12 hours	108.82 ± 3.60	95.70 ± 7.68	4	104.65 ± 11.58	115.70 ± 13.92	4
24 hours	98.70 ± 7.10	87.21 ± 8.10	6	94.35 ± 5.47	120.34 ± 20.24	6
48 hours	107.99 ± 7.27	88.06 ± 10.37	6	102.48 ± 14.65	121.82 ± 21.36	5
3 days	105.48 ± 9.20	98.67 ± 7.59	4	90.35 ± 5.86	82.71 ± 2.53	4
5 days	111.69 ± 8.92	92.38 ± 3.08	5	103.42 ± 8.69	116.15 ± 10.92	5
7 days	100.05 ± 6.36	88.37 ± 17.89	5	96.75 ± 5.52	95.42 ± 6.93	5
14 days	103.44 ± 9.90	81.33 ± 7.15	5	95.46 ± 6.68	120.97 ± 18.11	4

gadolinium within the parenchyma is likely the result of disturbances in the blood-brain-barrier (Reith et al., 1995); (Kastrup et al., 1999), (Park et al., 1999). In our study, there was no consistent parenchymal enhancement at any time point studied after cortical devascularization (Figure 17), despite the evidence of a lesion (Figure 17 A, B, D, E, G, H, arrows). As expected, parenchymal enhancement was not observed in any of the sham animals (Figure 17 C, F, I).

5.1.2 Temporal Evolution of Infarct Development: Morphological Changes

5.1.2.1 Neuronal Cell Death and Infarct Formation

Using cresyl violet histochemistry, control (un-operated) brains featured compact parenchyma with little extracellular space; neurons were round, with well-stained Nissl substance and prominent nuclei throughout the frontal areas (Figure 18 A, B). However, transection of a descending pial vessel produced a progressive pan-necrotic infarct in the cortical area supplied by that vessel.

Injury evolved systematically: 12 hours after surgery the tissue below the surgery site looked similar to control tissue (Figure 18 D) with occasional minor disruption in the outer molecular layer; at 24 hours the tissue remained intact with some vacuolated neurons (Figure 18 F). No morphological changes were observed in the contralateral (non-lesion) side at either of these early time points (Figure 18 C, E).

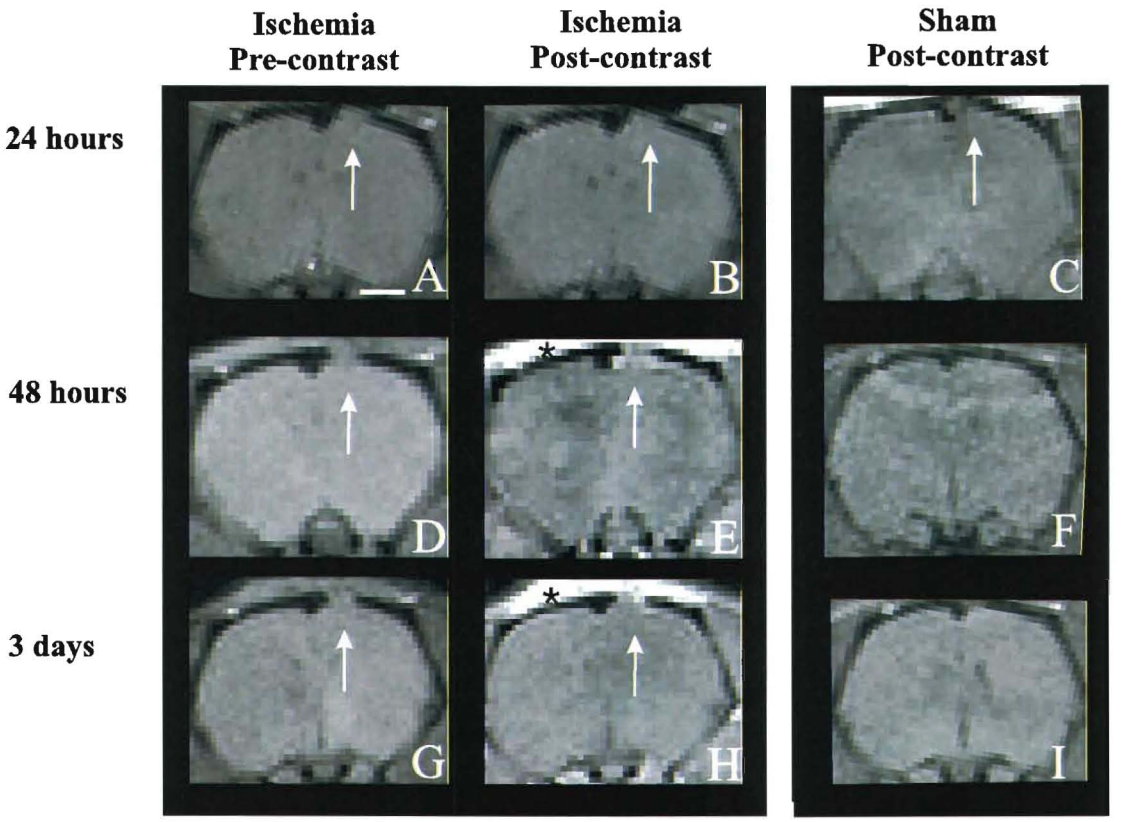

Figure 17: Representative T1 weighted (pre-contrast) and Gd-enhanced T1 weighted (post-contrast) images of ischemic animals 24, 48 hours and 3 days after surgery. After cortical devascularization, both the pre- and post-contrast images clearly show evidence of tissue injury (A, B, D, E, G, H arrows). After Gd injection, there was increased signal intensity in the meninges and skin overlying the injury site (E, H asterisk) but no enhancement within the parenchyma. Sham animals injected with Gd also showed no change in signal intensity within the parenchyma (C, F, I). Scale bar = 1 cm.

Figure 18: Photomicrographs of cresyl violet stained tissue sections from control (A, B), 12 hours (C, D) and 24 hours after cortical devascularization groups. Cresyl violet histochemistry of the control (A, B) animals shows the typical compact neuropil and rounded neuronal nuclei in both hemispheres which is characteristic of healthy tissue. Twelve hours (C, D) after cortical devascularization, both the contralateral and ipsilateral cortices continue to have the typical healthy appearance. In the 24-hour animals, some neuronal vacuolation begins to appear in the lesion cortex (F, arrows). Scale bar = 100 μm.

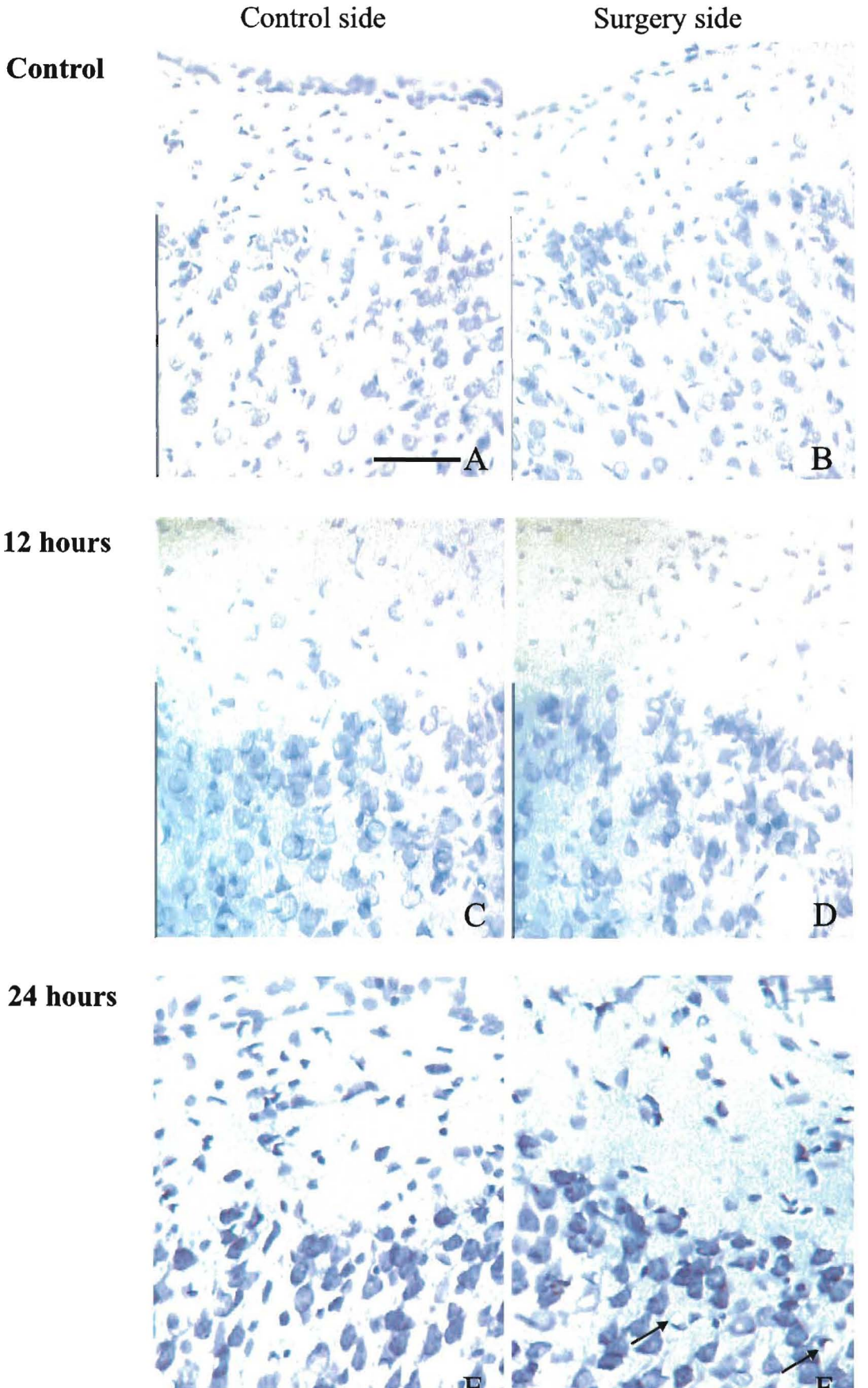
Control side
Surgery side
Control
A
B
12 hours
C
D
24 hours
E
F

Forty-eight hours after surgery, the area below the surgery site showed signs of infarct development. The parenchyma was vacuolated (Figure 19 B, asterisks) with increased extracellular space. Numerous shrunken, necrotic nuclei were present (Figure 19 B, arrows). Inflammatory cells (most likely polymorphonuclear cells) were observed in the overlying meninges. At 7 days, no recognizable neurons were found as the entire lesion area was filled with shrunken necrotic nuclei and what appeared to be inflammatory cells (Figure 19 D). Finally, at 14 days, the lesion area contained less cellular debris and appeared cystic (Figure 19 F). No overt histological changes were seen in the contralateral side (Figure 19 A, C, E). All the animals included in the histological analysis showed similar patterns of temporal development and infarct size.

In the sham-operated animals, histological analysis revealed healthy tissue in the cortical layers of both hemispheres with no evidence of swelling, vacuolation or cell necrosis in the area below the surgery site up to and including 3 days post-surgery (Figure 20). However, at 14 days, the cortex inferior to the surgery site had often herniated up into the surgery site. Cresyl violet staining showed that the herniated area was filled with compact neuropil and typically stained nuclei; however, the neuronal cell bodies had an elongated morphology.

While cresyl violet histochemistry clearly delineated the loss of neurons associated with infarct formation, Fluoro-Jade fluorescent immunohistochemistry was used to ascertain the extent of ongoing neuronal degeneration throughout the course of infarct formation. At all time points following cortical devascularization, there was no evidence of neuronal degeneration associated with the progressive development of the

Figure 19: Photomicrographs of cresyl violet stained tissue sections from animals 48 hours (A, B), 7 days (C, D) and 14 days (E, F) after cortical devascularization. Cresyl violet histochemistry shows healthy tissue in the contralateral cortex of the 48-hour (A), 7 (C) and 14 days (E) animals. However, at 48 hours, the lesion cortex is vacuolated (B, asterisks) with numerous necrotic nuclei scattered throughout (B, arrows). In both the 7 and 14 days animals an infarct has formed at the site of the devascularization (D, F). Scale bar =100 μm.

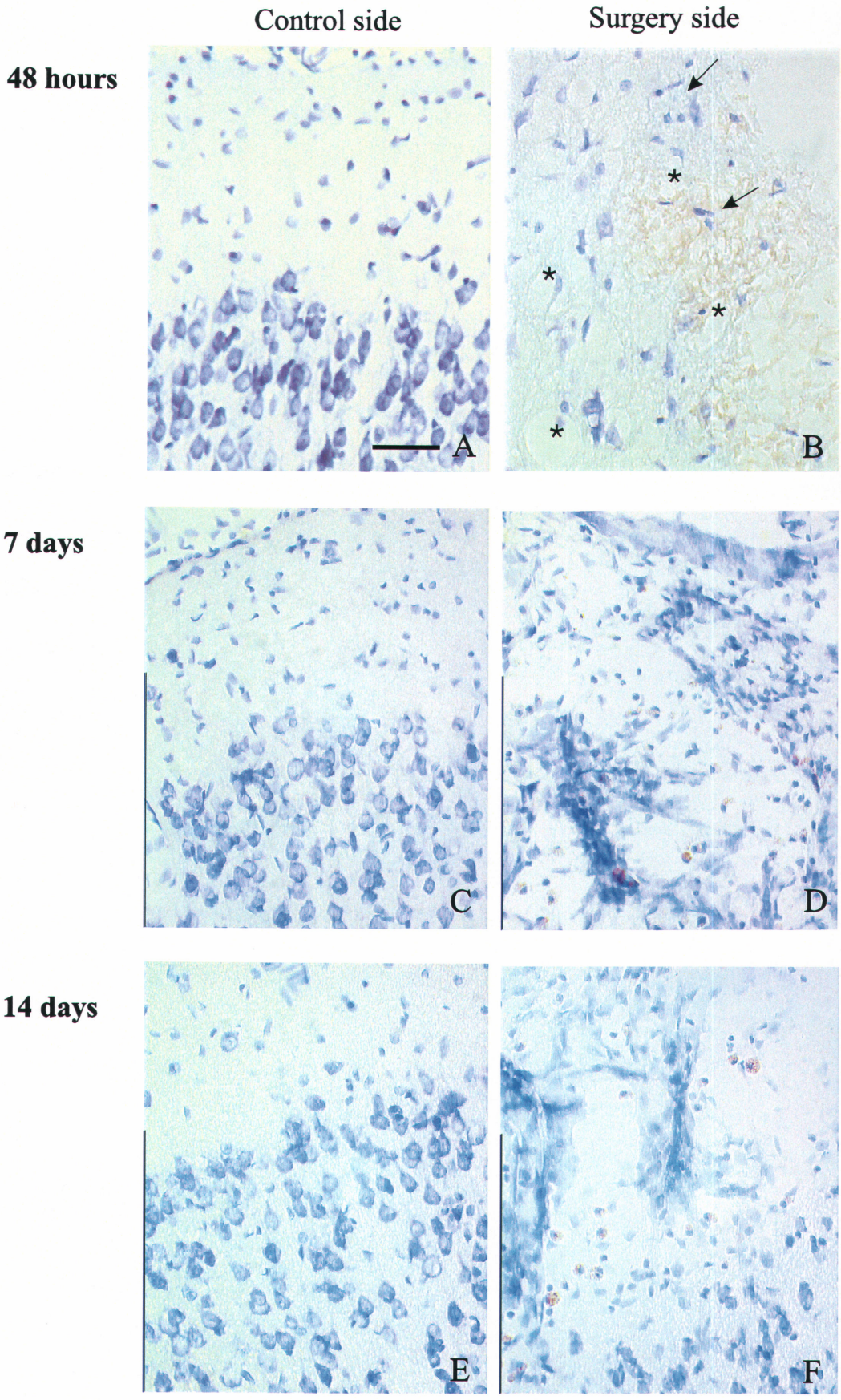
Control side
Surgery side
48 hours
7 days
14 days
A
B
C
D
E
F

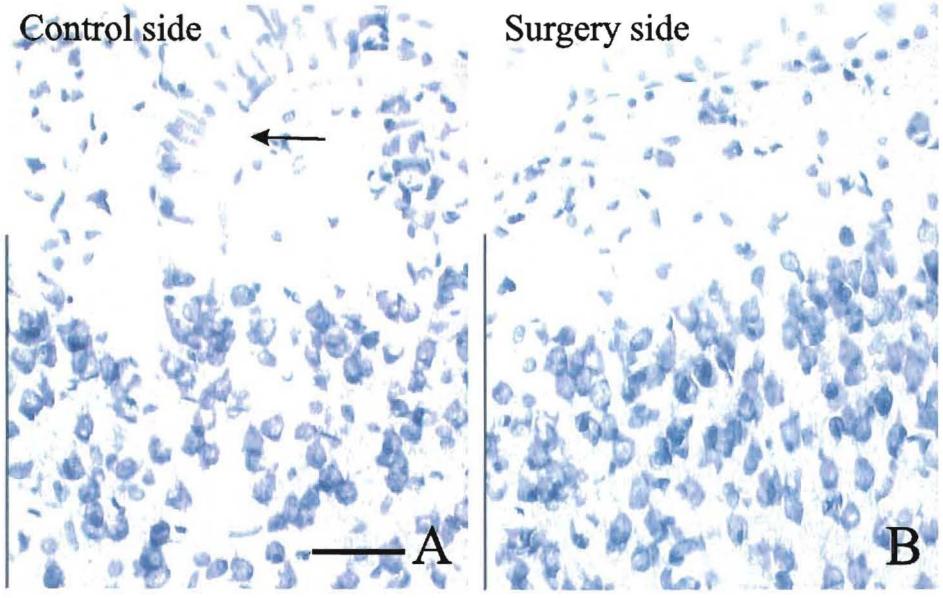

Figure 20: Photomicrographs of the contralateral (A) and lesion (B) cortices of a sham-operated animal 3 days after surgery. The sham-operated animals had the skull and dura removed from the same area as the cortical devascularization animals however, the pial vessel was not disrupted. Cresyl violet histochemistry shows healthy tissue in both motor cortices (A, B). The arrow indicates a descending vessel similar to those that would be disrupted during the devascularization surgery. Scale bar = 100 μm.

lesion, as indicated by the absence of Fluoro-jade positive neurons (Figure 21 B). Sections extending throughout the 500 μm rostral and caudal to the infarct were also stained with Fluoro-Jade and no evidence of neuron degeneration was present. Interestingly, many of the invading inflammatory cells stained with Fluoro-Jade (Figure 21 B), as did much of the infarct debris.

5.1.2.2 Lesion Area

Cresyl violet histochemistry was used to quantitatively measure the maximum area (mm^2) of tissue involved in the infarct. Within the first 24 hours after the devascularization surgery the injured area was restricted to a small ($<0.50\ mm^2$; Figure 22) area of edema and scattered vacuolation within the first two cortical layers. After 48 hours, the infarct area had increased significantly ($p<0.001$) from 24 hours to reach its maximum of $2.20 \pm 0.59\ mm^2$ (Figure 22). The infarct contained rarefied, vacuolated tissue with widespread necrosis and edema involving all cortical layers (see Figure 19 B). Three days after the injury the area of the infarct had decreased to $1.53 \pm 0.32\ mm^2$ and contained mainly cellular debris and scattered inflammatory cells. Seven days after injury, the lesion area remained at $1.59 \pm 0.27\ mm^2$ (Figure 22).

5.1.2.3 Glial Reactivity

After cortical devascularization, astrocytes within both hemispheres responded to the unilateral injury (Figure 23). Within, 24 hours of the injury, the ipsilateral cortex showed increased GFAP immunoreactivity in many of the perivascular astrocytes as

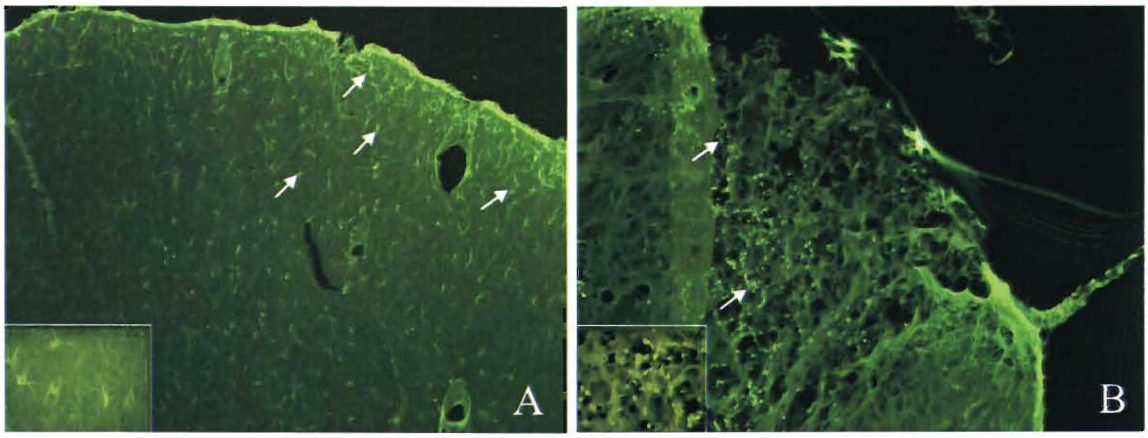

Figure 21: Fluorescent photomicrographs of cortical tissue from the ipsilateral hemisphere of a control (A) and a devascularized animal (B) stained with Fluoro-Jade 7 days after injury. The control tissue shows staining of numerous glial cells (A, arrows) and the meninges. In the injured animal, numerous cells within the infarct stained with Fluoro-Jade (B, arrows). Inset images provide enhanced view of the morphology of the stained cells.

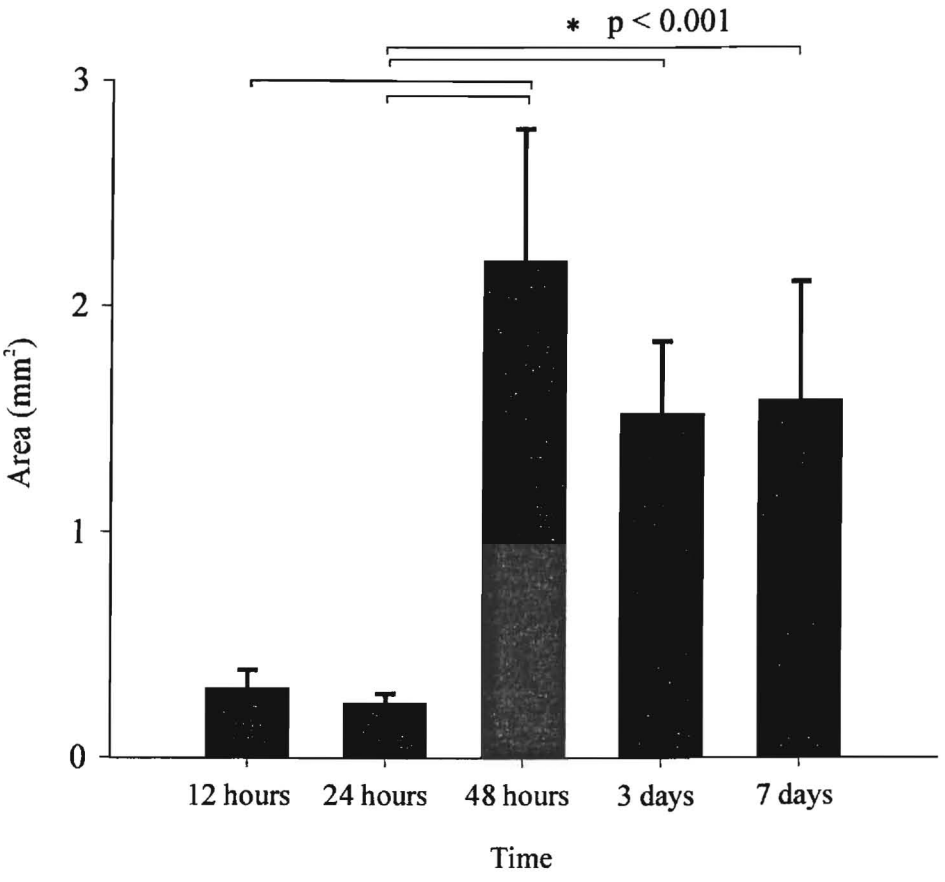

Figure 22: Graph of the mean lesion area ($mm^2 \pm$ SEM) at 12, 24, and 48 hours, 3 and 7 days after injury. The lesion was located 2 mm from Bregma and reached its maximum size at 48 hours. The asterisk denotes statistical difference (ANOVA, $p<0.001$).

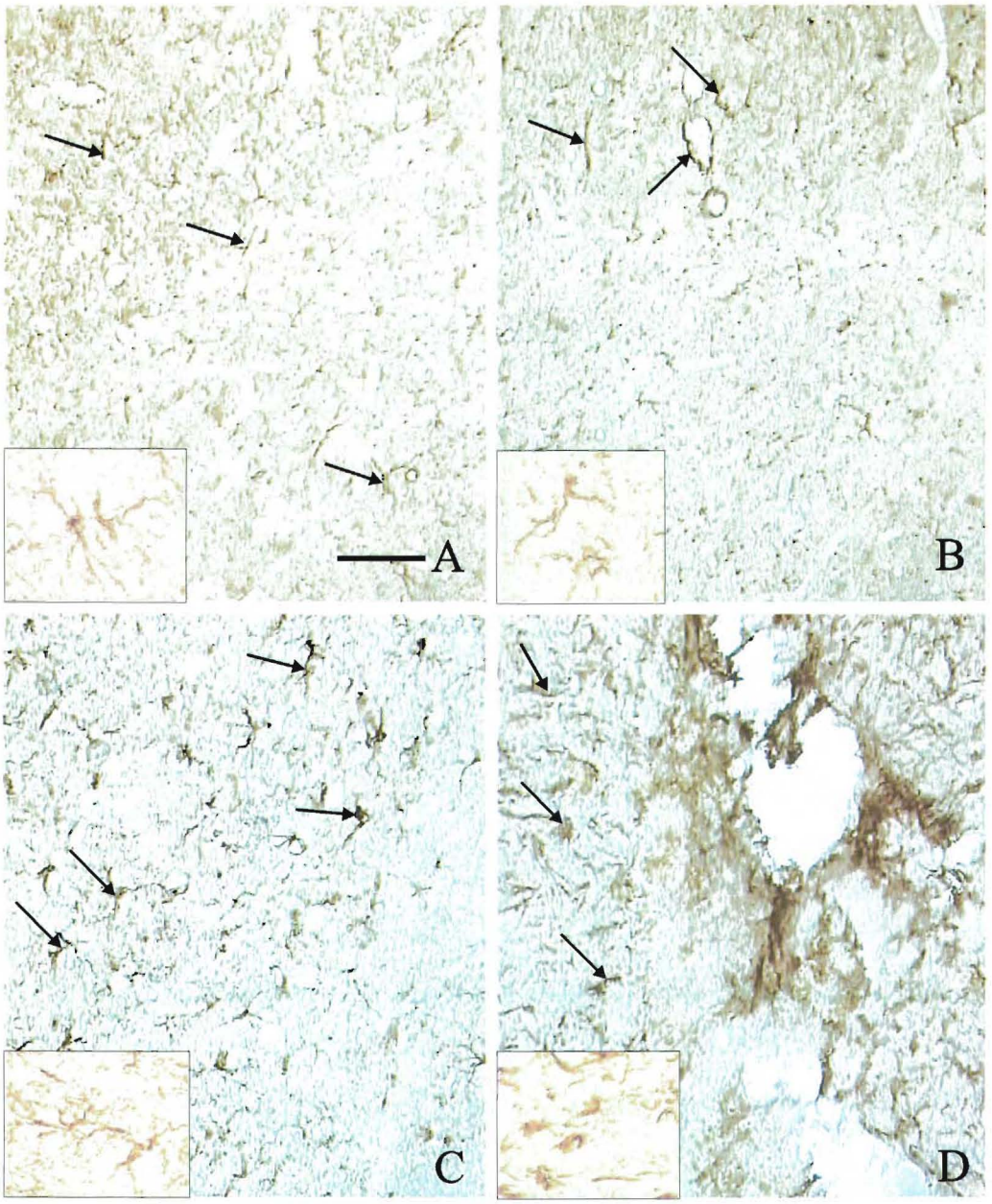

Figure 23: Photomicrographs of the ipsilateral cortex immunostained with a rabbit anti-GFAP monoclonal antibody from control animals (A), and at 24 hours (B), 48 hours (C) and 7 (D) days after cortical devascularization. Faint GFAP immunoreactivity highlighting the typical stellate morphology of astrocytes can be observed in the control tissue (A, arrows and inset). After devascularization, GFAP immunoreactivity increased over time; first in the perivascular astrocytes (B, arrows) then in the numerous reactive astrocytes surrounding the infarct (C, arrows). By 7 days a glial scar has formed around the edge of the lesion (D, arrows). Inset images are at a higher magnification (100 X) to display better cellular detail. Scale bar = 100 μm.

well as a number of other scattered astrocytes. While these cells had increased immunoreactivity, they did not display a reactive morphology (Figure 23 B). Astrocytes within the contralateral thalamus, corpus callosum and cingulate areas also had increased GFAP reactivity, with a few scattered reactive astrocytes in the corpus callosum and medial cingulate area. After 48 hours, a band of reactive astrocytes were found surrounding the infarct (Figure 23 C), which were still present 7 days after the injury (Figure 23 D). Numerous reactive astrocytes were also present throughout the entire ipsilateral hemisphere.

Similar to tissue taken from the control group, astrocytes in the subpial layer (glial limitans), the outer molecular layer, and surrounding the blood vessels of the sham-operated animals had faint GFAP immunoreactivity (Figure 24 A).

Twenty-four hours after injury, a dramatic increase in OX-42 immunoreactivity was observed in the microglia of both hemispheres in comparison to control animals (Figure 25 A, B). Despite the increase in immunoreactivity, these cells retained the typical stellate shape and highly branched processes of resting microglia. After 48 hours, OX-42 immunoreactivity in both the ipsilateral and contralateral cortex declined from its 24-hour peak, however the immunoreactive cells began to feature the characteristic reactive morphology including the shortened cellular processes and the loss of secondary arborizations (Figure 25 C). These cells were located in the peri-infarct areas and appeared as a band around the developing infarct. After 7 days, numerous immunoreactive cells with an amoeboid morphology were observed surrounding the infarct (Figure 25 C, arrows). Further, immunoreactive cells with a

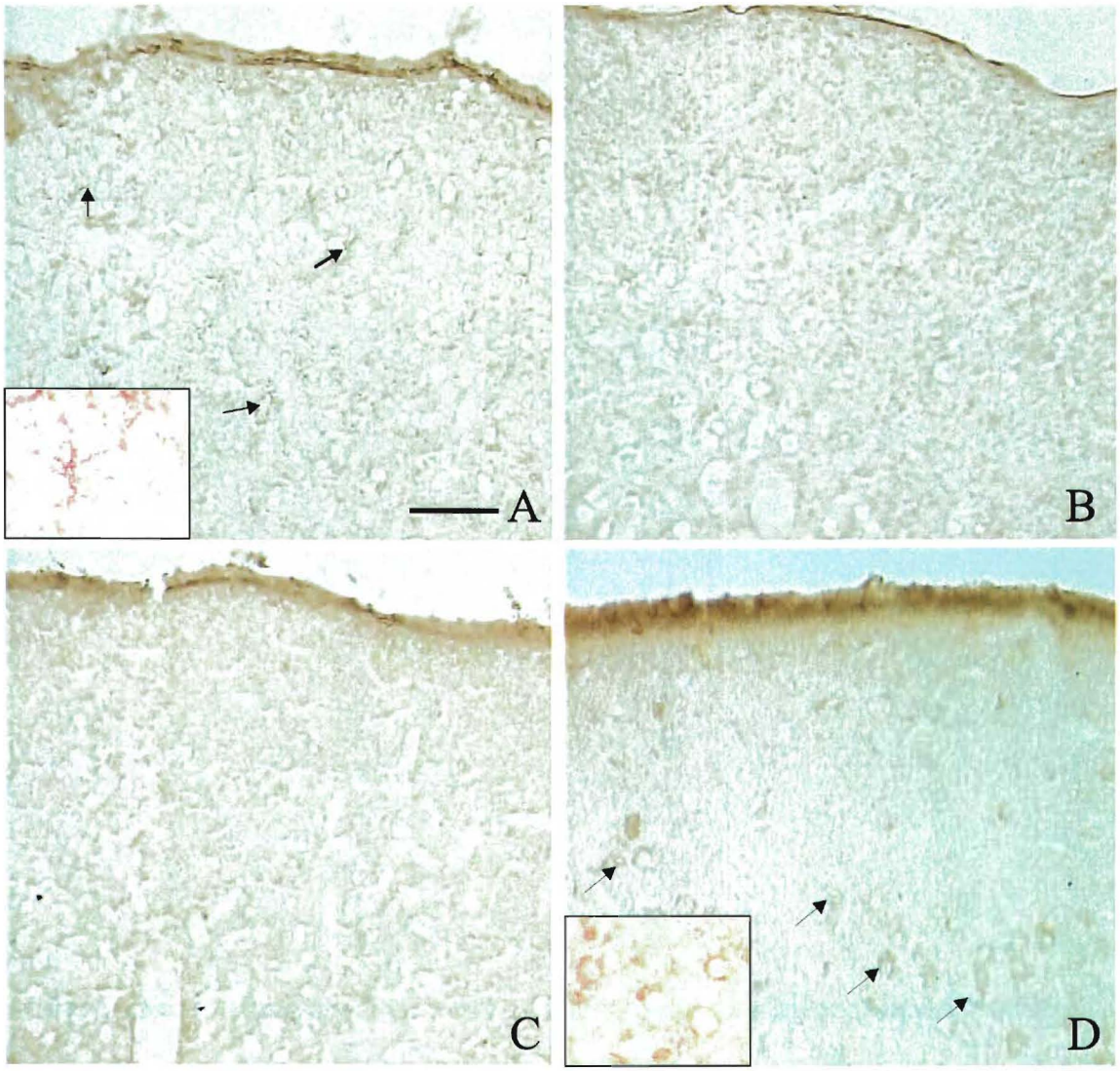

Figure 24. Ipsilateral cortical tissue 3 days after sham surgery immunostained for GFAP (A), OX-42 (B) ED-1 (C) and NFκB (p65 sub-unit) (D) . GFAP immunostaining shows little GFAP immunoreactivity with some reactivity in the perivascular astrocytes (A, arrows and inset). Faint OX-42 immunoreactivity could be found in both hemispheres (B) and there was no ED-1 immunoreactivity detected in either hemisphere (C). NF-κB immunoreactivity was detected throughout both hemispheres but was restricted to the cytoplasm of neurons (D, arrows and inset). Inset images are at a higher magnification (100 X) to show greater cellular detail. Scale bar = 100 μm

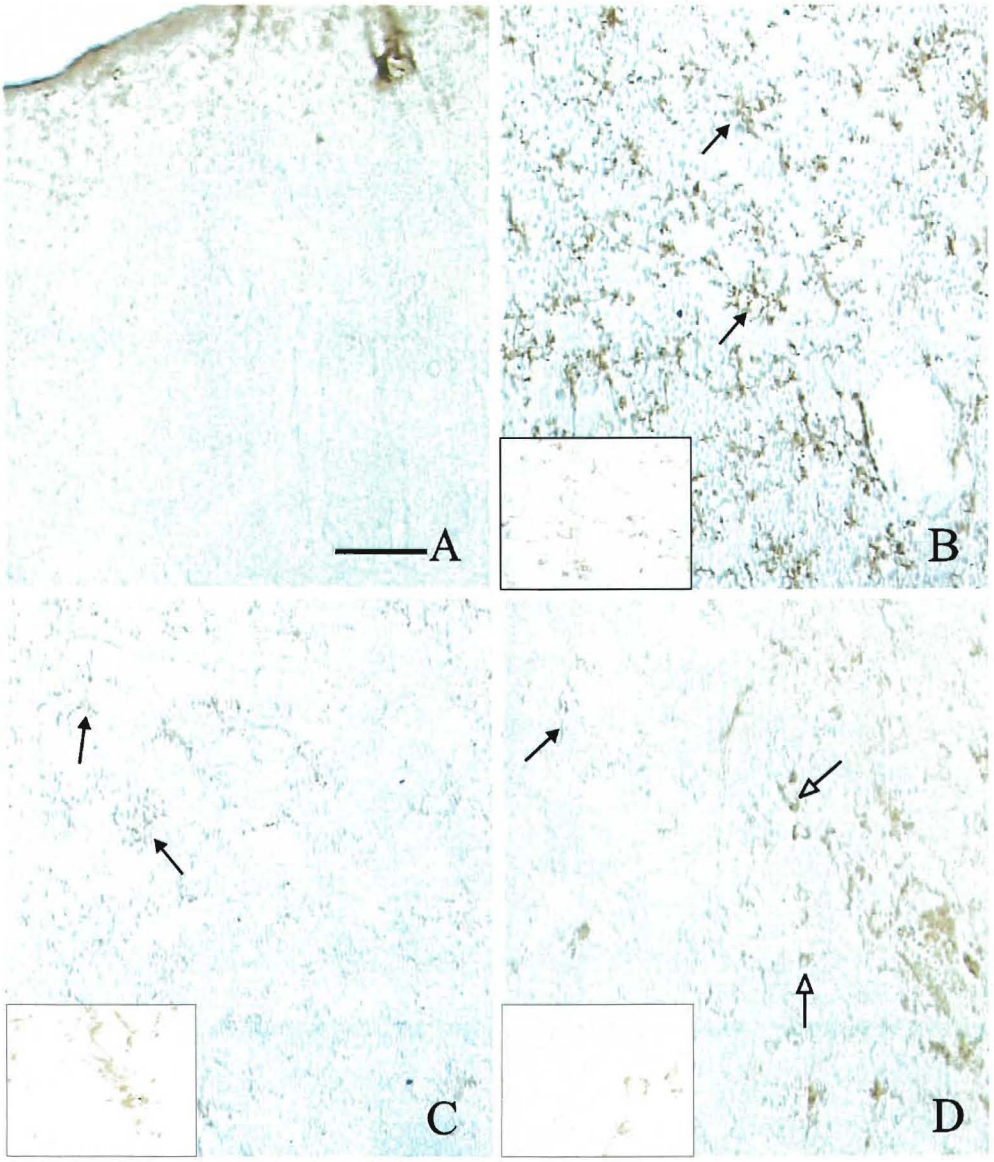

Figure 25. Representative photomicrographs of the ipsilateral cortex immunostained for OX-42 from control animals (A), and 24 hours (B), 48 hours (C) and 7 (D) days after cortical devascularization. Control tissue had no discernable OX-42 immunoreactivity (A). However, 24 hours after cortical devascularization a substantial increase in OX-42 immunoreactivity was observed throughout the ipsilateral hemisphere (B, arrows). After 48 hours, the immunoreactivity decreased with the OX-42 positive cells featuring a more reactive morphology (C, arrows). After 7 days OX-42 immunoreactivity could be found in the ramified, amoeboid microglia (D, closed arrows) of the surrounding glial scar as well as in any remaining macrophages within the infarct (D, open arrows and inset). Inset images are at a higher magnification (100 X) for greater cellular detail. Scale bar = 100 μm.

rounded nuclear morphology were observed surrounding and within the infarct as well as on the surface of the brain in the region of the infarct (Figure 25 D, arrows). The morphology and location of these cells made it difficult to determine if these were invading hematogenous macrophages or phagocytic microglia.

The sham animals had only faint OX-42 immunoreactivity throughout both hemispheres with the most intense staining observed in the corpus callosum (Figure 24 B).

5.1.2.4 Inflammatory Response

ED-1 reactivity is specific for a subset of glycoproteins on the surface of lysozomal membranes and is used to identify phagocytic cells, specifically, reactive and phagocytic macrophages and microglia (Dijkstra et al., 1985); (Bauer et al., 1994); (Damoiseaux et al., 1994). The ipsilateral cortex of both control and devascularized animals examined 12 and 24 hours after injury had no ED-1 positive cells within the parenchyma (Figure 26 A, B). However, a small number of ED-1 positive cells could be seen in the overlying meninges, most likely the result of bleeding into the subarachnoid space during the surgical procedure. After 48 hours, the enlarged subarachnoid space adjacent to the infarct was filled with ED-1 positive cells. Numerous ED-1 positive cells were observed within and adjacent to vacuoles in the infarct (Figure 26 C). By 7 days, the number of ED-1 positive macrophages within the infarct had decreased and these were restricted to areas of the infarct that still contained cellular debris (Figure 26 D, open arrows). Numerous ED-1 positive ramified microglia were observed surrounding the infarct (Figure 26 D, closed arrows).

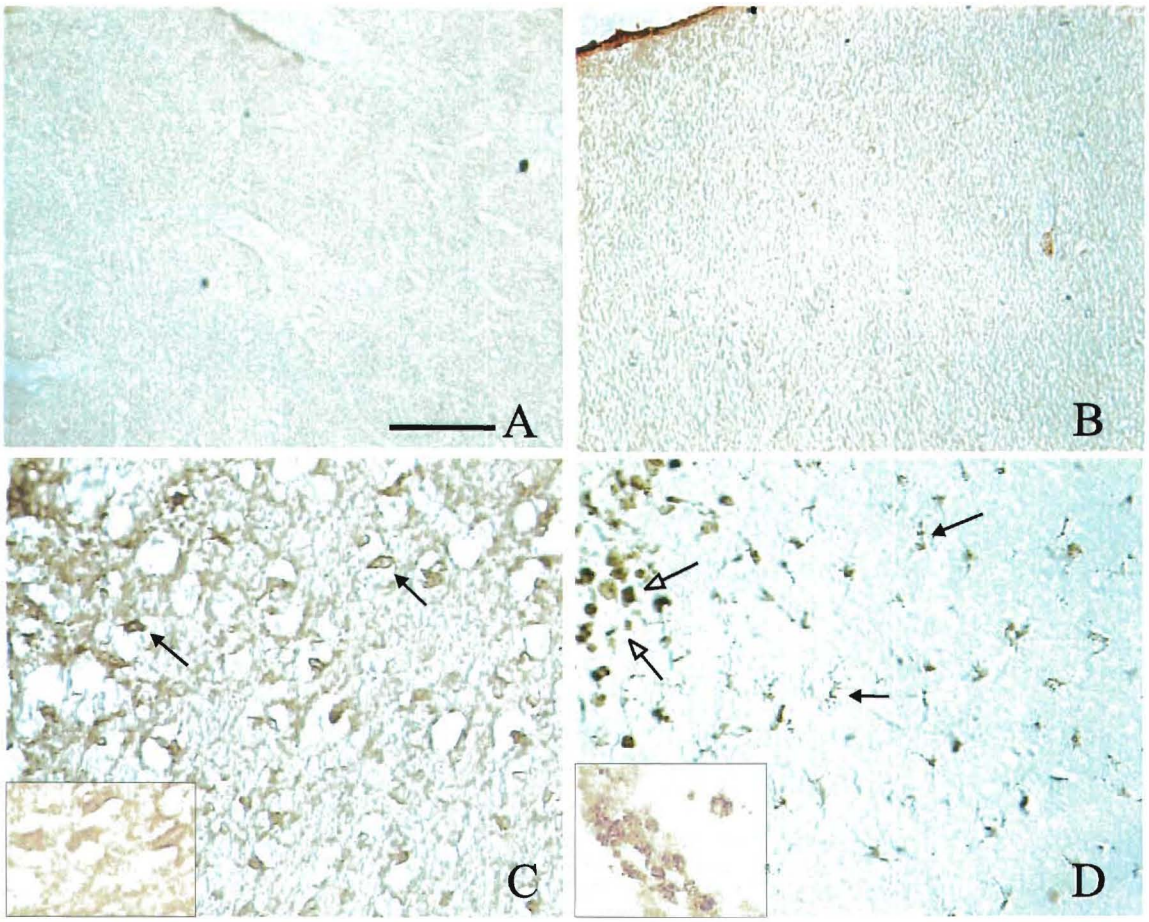

Figure 26. Ipsilateral cortical tissue immunostained with a mouse anti-ED-1 monoclonal antibody from control rats (A), 24 (B) and 48 hours (C), and 7 days (D) after cortical devascularization. There was no ED-1 immunoreactivity until 48 hours at which point ED-1 positive cells were found within and adjacent to vacuoles in the lesion area (C, arrows and inset). After 7 days the ED-1 positive cells have both a rounded morphology characteristic of hematogenous macrophages (D, open arrows and inset) as well as the ramified, amoeboid shape characteristic of activated microglia (D, closed arrows). Inset images are at a higher magnification (100 X) for better cellular detail. Scale bar = 100 μm.

In the sham-operated animals there was no ED-1 immunoreactivity within the parenchyma but an occasional ED-1 positive cell in the surrounding subarachnoid space were observed (Figure 24 C).

5.1.2.5 Nuclear Factor kappa B (NF–κB) Activation

NF-κB is a transcription factor that is upregulated by a number of stimuli (free radicals, cytokines, physical stress) and plays a role in potentiating the inflammatory response via regulation of gene transcription (Flohe et al., 1997); (Ghosh et al., 1998); (Christman et al., 2000). Faint immunoreactivity was observed in both the cytoplasm and nuclei of all neurons in both the ipsilateral and contralateral hemispheres of control (Figure 27 A) and 24 hours post-injury (Figure 27 B) groups. After 48 hours, degenerating cells within the infarct were strongly immunoreactive as were neurons in the surrounding peri-infarct region (Figure 27 C, arrows). This immunoreactivity localized principally to the nucleus. Neurons in the contralateral hemisphere were only weakly immunoreactive. After 7 days, neurons in the surrounding peri-infarct region remained moderately immunoreactive, however macrophages surrounding the infarct had very intense, punctate immunoreactivity (Figure 27 D, arrows). Neurons in the contralateral hemisphere were only faintly immunoreactive.

The sham-operated animals also showed faint neuronal immunoreactivity, similar to that observed in both control and contralateral cortical tissue (Figure 24 D).

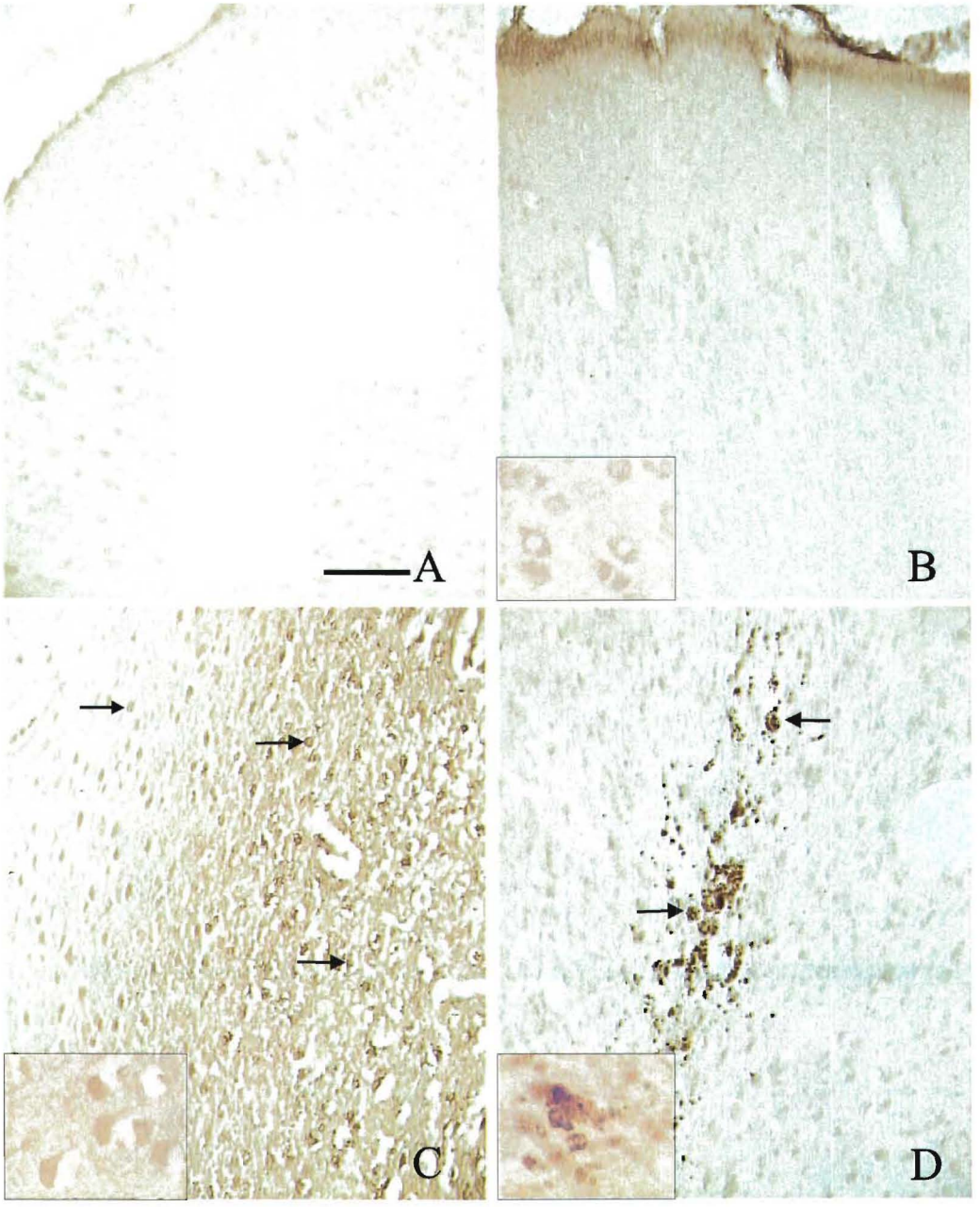

Figure 27. Photomicrographs of ipsilateral cortical tissue immunostained for NF-κB p65 sub-unit activation in control rats (A), and 24 hours (B) 48 hours (C), and 7 days (D) after cortical devascularization. There was faint NF-κB immunoreactivity co-localized to neurons in both the control (A) and 24 hour (B, inset) tissue. At 48 hours, the nuclei of degenerating neurons (C, arrows and inset) were strongly immunoreactive. After 7 days, neurons surrounding the infarct were faintly NF-κB immunoreactive while macrophages within the infarct were strongly immunoreactive (D, arrows and inset). Inset images are taken at a magnification of 100 X for improved cellular detail. Scale bar = 100 μm.

5.1.3 Cytokine Expression

Pro-inflammatory cytokines have been reported to play a role in the pathogenesis of cerebral ischemia (Yamasaki et al., 1996); (Pantoni et al., 1998); (Feuerstein et al., 1998);(Martiney et al., 1998) and traumatic brain injury (Arvin et al., 1996); (Ghirnikar et al., 1998). As part of characterizing the pathological events associated with a cortical devascularization injury, the pro-inflammatory cytokines TNF-α and IFN-γ were studied with the evolution of this slowly developing infarct. These two cytokines are released by inflammatory cells after immune stimulation, are highly cytotoxic, and are potent activators of inflammatory cells and resident glia (Roitt et al., 1998).

5.1.3.1 TNF-α and IFN-γ Fluorescent Immunocytochemistry

TNF-α and IFN-γ fluorescent immunocytochemistry was used to determine the presence and cellular source of these cytokines after the cortical devascularization injury. Double labeling experiments revealed that both these cytokines were present in moderate amounts within the parenchyma and subarachnoid space during the active formation of the infarct. This immunoreactivity co-localized to ED-1 positive phagocytes. Prior to infarct formation, TNF-α and IFN-γ immunoreactivity was restricted to ED-1 positive circulating monocytes residing in the tissue capillaries. Twenty-four hours after the surgery there was an accumulation of ED-1 positive microglia and monocytes in the superficial cortical layers inferior to the surgery site (Figure 28 A, C). However, only those cells with a round cell body were TNF-α (Figure 28 B) or IFN-γ (Figure 28 D) positive. After 48 hours, numerous ED-1/TNF-α (Figure

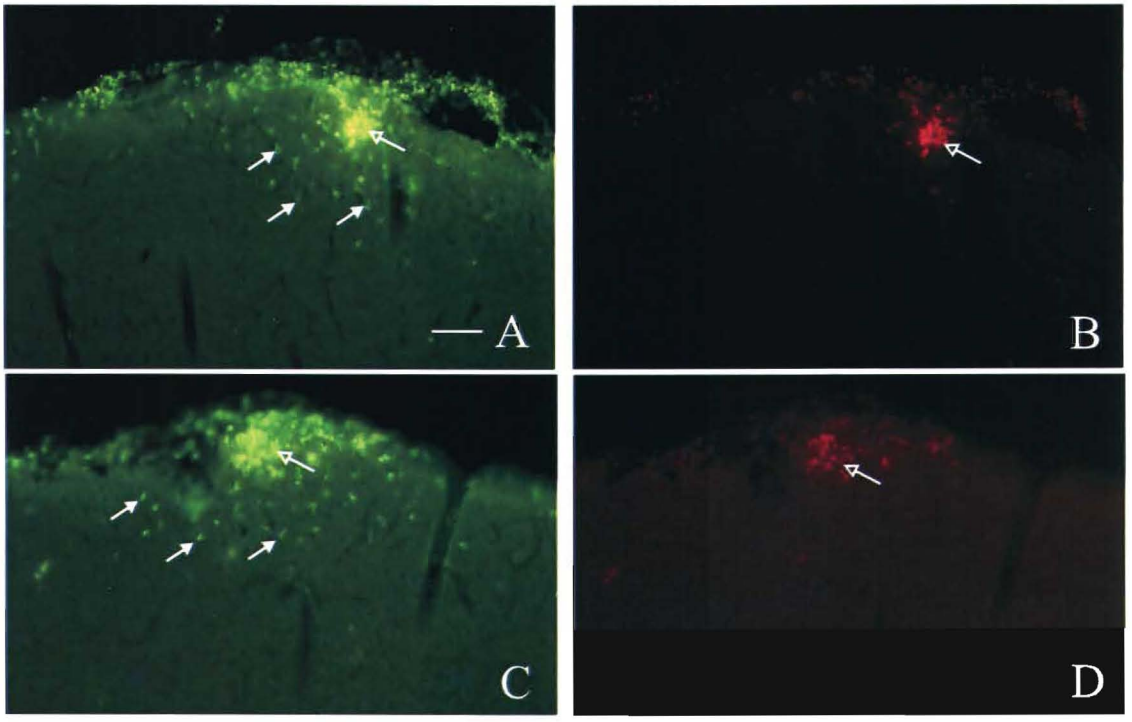

Figure 28: Fluorescent photomicrographs of the ipsilateral cortex of animals 24 hours after cortical devascularization labeled with an ED-1 antibody (A, C), TNF-α (B) and IFN-γ (D). ED-1 immunoreactivity indicates that both phagocytic macrophages (A, B; open arrows) and microglia (A, B; closed arrows) are present during infarct formation. The pro-inflammatory cytokines TNF-α (B; open arrows) and IFN-γ (D; open arrows) were also present during infarct formation and co-localize with ED-1 positive macrophages. Scale bar = 100 μm.

29 A, B) and ED-1/ INF-γ (Figure 29 C, D) immunoreactive cells were found throughout the infarct and into the surrounding parenchyma and subarachnoid space. Again these cells featured the rounded morphology of phagocytic macrophages. Seven days after injury, numerous ED-1 immunoreactive macrophages and microglia were present in the infarct and peri-infarct regions (Figure 30 A, C) however; the amount of TNF-α immunoreactivity appeared to be decreasing (Figure 30 B). In addition, IFN-γ immunoreactivity was absent by this time (Figure 30 D).

In the sham-operated animals, TNF-α and IFN-γ immunoreactivity was restricted to cells located within the parenchymal capillaries and co-localized to ED-1 immunoreactive circulating monocytes.

5.1.3.2 TNF-α and IFN-γ Enzyme Linked Immunosorbent Assay

After finding both TNF-α and IFN-γ immunoreactive cells during infarct formation, a sandwich ELISA technique was used to quantify the level of these cytokines 6, 12, 24, 48 hours and 3 days after surgery. Despite TNF-α immunoreactivity, there were no significant changes in TNF-α cytokine levels at any time point in either the ipsilateral or contralateral hemispheres (Table 3). Moreover, the only significant change in IFN-γ activity was in the contralateral cortex, which showed a decrease in concentration 6 hours and 3 days after injury (Table 3).

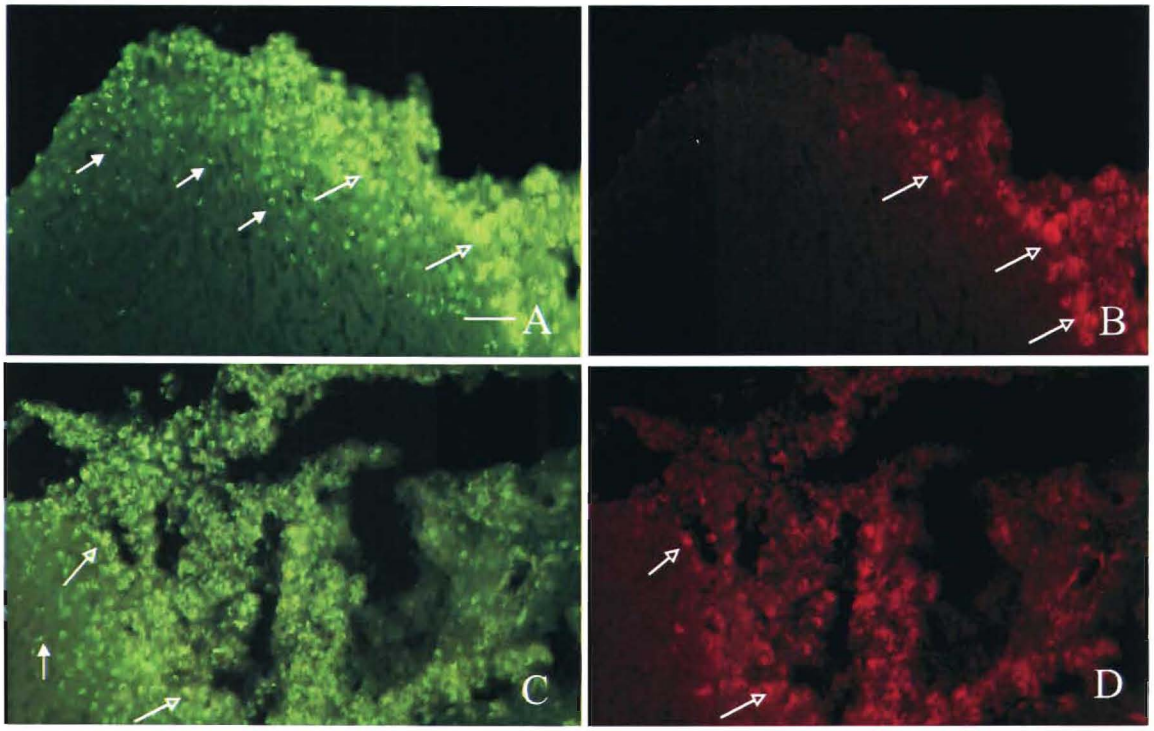

Figure 29: Fluorescent photomicrographs of animals 48 hours after cortical devascularization labeled with an ED-1(A, C), TNF-α (B) and IFN-γ (D) antibody. ED-1 immunoreactivity shows an increase in both phagocytic macrophages (A, B; open arrows) and microglia (A, B; closed arrows) in the developing infarct of the ipsilateral cortex. TNF-α (B; open arrows) and IFN-γ (D; open arrows) co-localized to ED-1 positive macrophages at the edge of the infarct. Scale bar = 100 μm.

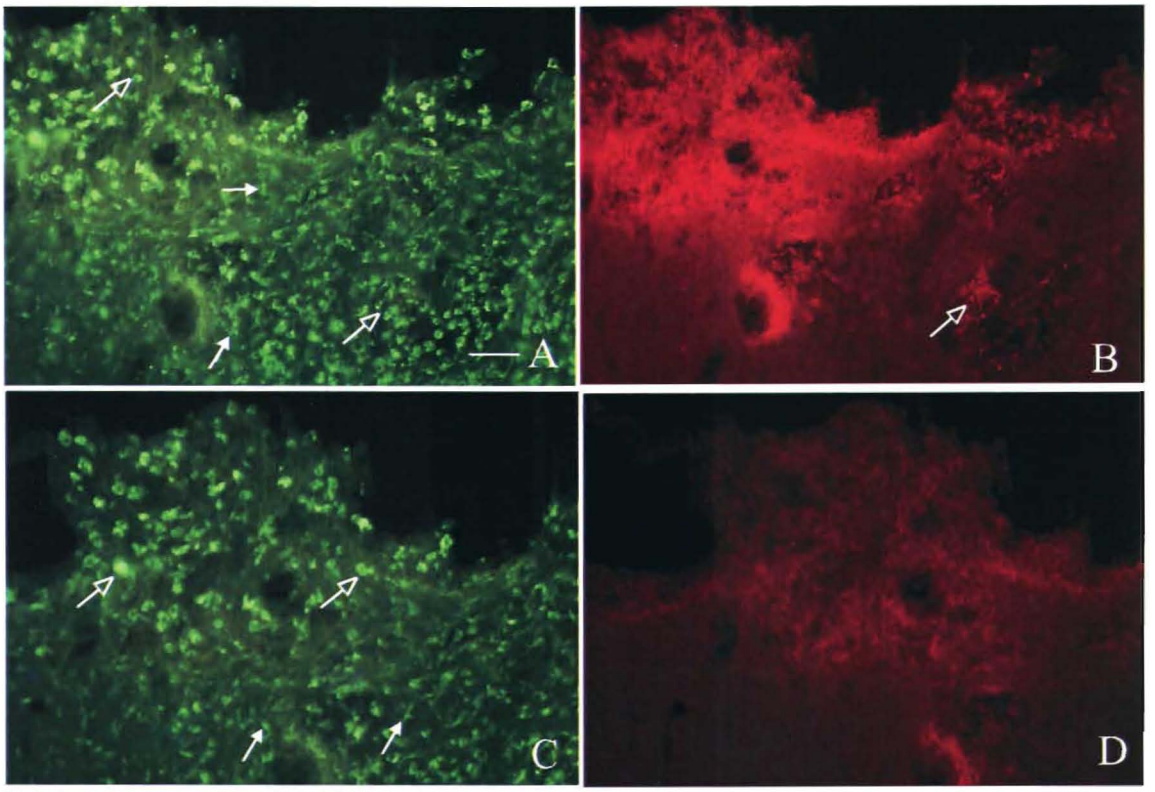

Figure 30: Fluorescent photomicrographs of the infarct in animals 7 days after cortical devascularization. ED-1 immunoreactivity indicates that both phagocytic macrophages (A, C open arrows) and microglia were still present 7 days after injury (A, C closed arrows). A small amount of TNF-α immunoreactivity (B; open arrows) was present within the infarct and co-localized to ED-1 positive macrophages. IFN-γ immunoreactivity was absent at this time point (D). Scale bar = 100 μm.

Table 3: Mean concentration (pg/ml ± SD) of TNF-α and IFN-γ in the ipsilateral and contralateral cortex of ischemic animals[1].

	TNF-α activity (pg/ml ± SD)			**IFN-γ activity** (pg/ml ± SD)		
Observation Time	**Lesion side**	**Contralateral side**	**n**	**Lesion side**	**Contralateral side**	**n**
Control	2.10 ± 2.25	2.26 ± 0.45	8	5.49 ± 4.59	5.09 ± 0.73	5
6 hours	2.72 ± 3.98	1.79 ± 3.25	4	5.68 ± 0.37	2.05 ± 0.29*	3
12 hours	1.49 ± 2.78	3.86 ± 4.56	6	6.49 ± 4.70	6.38 ± 5.15	3
24 hours	0.48 ± 2.83	1.67 ± 4.28	7	4.66 ± 5.94	3.07 ± 3.33	3
48 hours	2.57 ± 3.87	2.07 ± 2.29	9	4.76 ± 3.33	3.85 ± 3.75	5
3 days	1.76 ± 3.79	2.04 ± 3.74	6	2.07 ± 0.72	1.45 ± 0.51*	3

[1]Values in a column followed by asterisk are significantly different from the control value at the 5% level according to a repeated measure one-way ANOVA followed by individual Student-Newman-Keuls comparisons.

5.2 Neuroprotection After Cortical Devascularization

5.2.1 MR Changes

The effectiveness of saline, DMSO and APTRA-AM in preventing the diffusion changes associated with cortical devascularization was assessed at 12, 24, 48 hours and 3, 7 days after injury. A multiple b-value DWI sequence using b-values of 110, 350 and 738 s/mm^2 was used.

5.2.1.1 Saline Treatment

Eight animals underwent cortical devascularization followed by two injections of saline one and 12 hours after injury. Two of these animals were removed from the study, as the ADC values obtained at the prescan time point were two standard deviations above the mean. The following results describe observations made from the remaining six animals.

The b = 19 s/mm^2 (nominal b-value) images show the first appearance of a hyper-intense lesion at 12 hours (Figure 31 D) which continued until 3 days after injury (Figure 31 G, J, M). With the addition of the diffusion gradients (i.e. 350 s/mm^2), the lesion area remained hyper-intense in the first 3 days suggesting a decrease in the diffusion of water within the lesion area (Figure 31 E, H, K, N). The corresponding ADC maps confirmed the decrease in diffusion at 12, 24 and 48 hours (Figure 31 F, I, L). After 7 days, a noticeable morphological change was apparent in the lesion area. This was associated with an increase in signal intensity in the b = 350 s/mm^2 image and a decrease in signal intensity in the ADC map (Figure 31 Q, R).

Figure 31: Diffusion un-weighted (b = 19 s/mm^2), weighted (b = 350 s/mm^2), and ADC map images of animals injected with saline at 1 and 12 hours after cortical devascularization. The un-weighted, weighted and ADC map images are typical for the prescan (A - C) group. A region of increased signal intensity corresponding to the lesion area (arrows) is observed in both the un-weighted and weighted images at 12 (D, E), 24 (G, H), 48 hours (J, K) and 3 days (M, N). The ADC maps show the lesion as an area of decreased signal intensity (arrows) at 12 (F) and 24 (I) and 48 hours (L). After 7 days there was no longer an increase in signal intensity in the un-weighted image (P) however, the weighted image (Q) and ADC map (R) show an area of diffuse restricted diffusion in the cortex of the ipsilateral hemisphere. Scale bar = 1 cm.

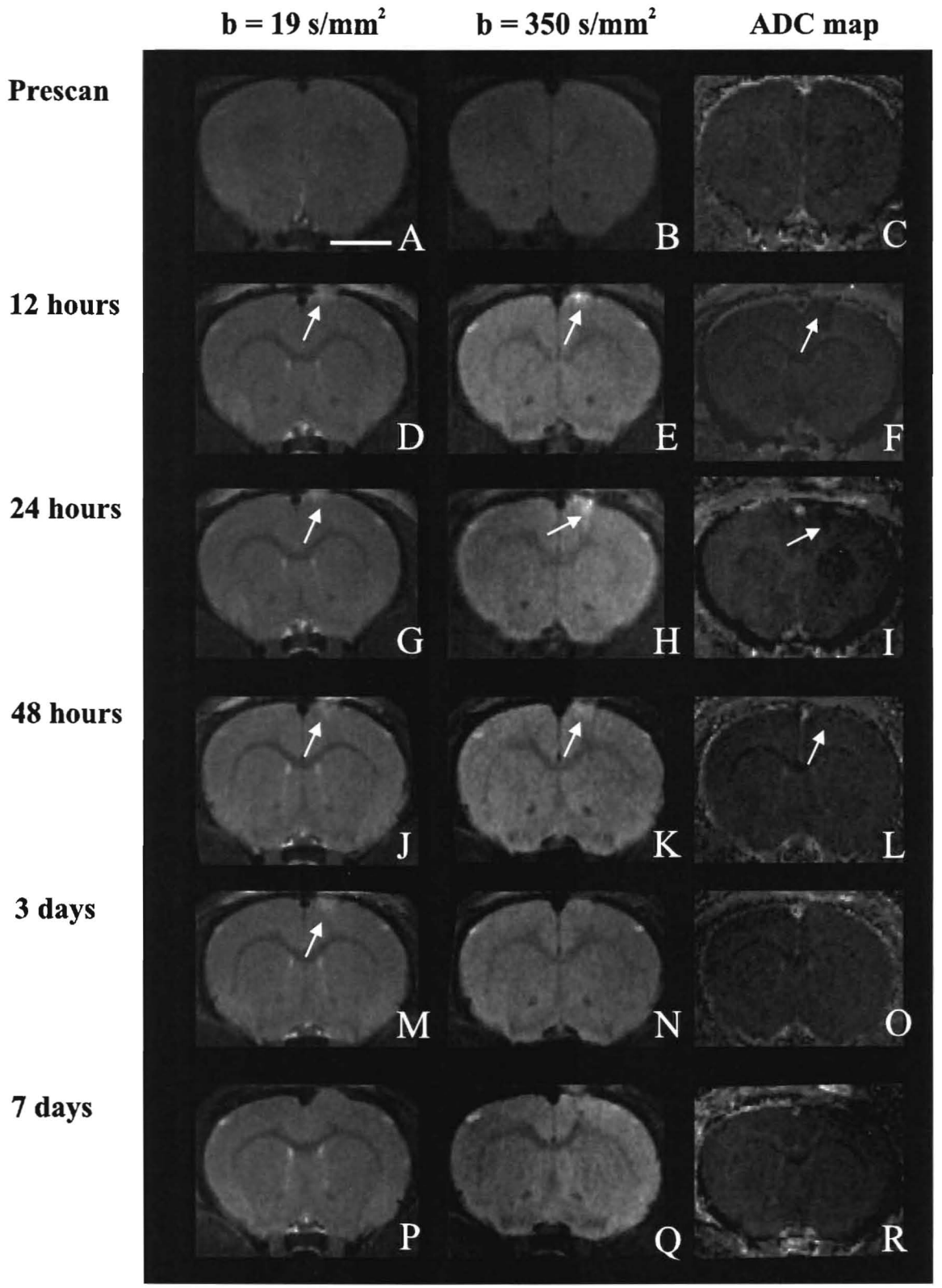
b = 19 s/mm²
b = 350 s/mm²
ADC map
Prescan
12 hours
24 hours
48 hours
3 days
7 days
A
B
C
D
E
F
G
H
I
J
K
L
M
N
O
P
Q
R

The mean ADC values of each ROI were calculated for each b-value and then plotted over time. Using a b-value of 110 s/mm^2, a significant ($p<0.05$) decrease in the ADC of the ipsilateral/lesion ROI was first observed at 24 hours and remained below prescan values throughout the first 3 days (Figure 32 A; Table 4). However, by 7 days, the ADC returned to prescan values (Figure 32 A). The most significant ($p<0.01$) decrease in ADC was observed in the lesion ROI at 3 days after injury and treatment. In the contralateral ROI, a highly significant ($p<0.001$) decrease in ADC was observed 12 hours after injury (Figure 32 A). This was followed by a dramatic increase in the ADC at 24 hours, which then began to slowly decrease towards the prescan value over the following 6 days (Figure 32 A). When the contralateral and lesion ADC values were compared, there was a significant ($p<0.05$) difference at 24 hours and a highly significant ($p<0.001$) difference at 3 days (Table 4).

With a b-value of 350 s/mm^2, a decrease in the ADC of the lesion ROI could not be observed until 24 hours after injury after which time it began to slowly increase back towards the prescan value (Figure 32 B). While the decrease in ADC at 24, 48 hours and 3 days was not significant when compared to the prescan value, these changes were significant ($p<0.05$) when compared to the 7 day ADC value (Figure 32 B). In the contralateral ROI, there were no significant changes in ADC (Figure 32 B). When the contralateral and lesion ADC values at each time point were compared, we found no significant differences at any time point (Table 4).

Using a b-value of 738 s/mm^2, we were unable to detect a significant decrease in the ADC of the lesion at any of the time points studied, when compared to the prescan ADC value (Figure 32 C). However, the 7 day lesion ADC values

Figure 32: Mean ADC (mm^2/s ±SEM) versus observation time of the contralateral and lesion ROI of saline treated animals collected at b = 110 s/mm^2 (A), b = 350 s/mm^2 (B), or b = 738 s/mm^2 (C). At b = 110 s/mm^2 a significant ($p<0.05$) difference in the ADC of the lesion ROI at 24, 48 hours, and 7 days was observed when compared to the prescan ROI (A, asterisks). A highly significant ($p<0.001$) decrease in ADC was observed at 3 days after injury (A, double asterisk). A significant decrease was also observed in the contralateral ROI at 12 hours (A, asterisk). At b = 350 s/mm^2, there was a significant ($p<0.05$) decrease in ADC at 24, 48 hours and 3 days when compared to 7 days (B, asterisk). At b = 738 s/mm^2, there was a significant ($p<0.05$) decrease in ADC at 24, 48 hours and 3 days when compared to 7 days (C, asterisk).

A

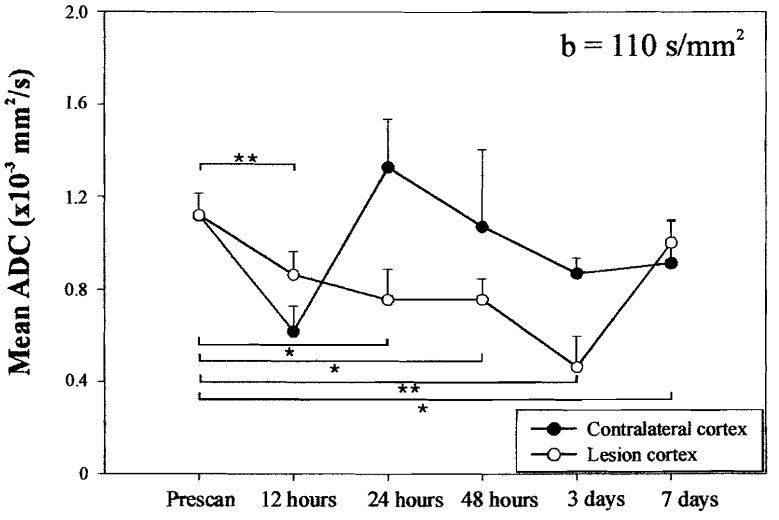
b = 110 s/mm²
Mean ADC (x10⁻³ mm²/s)
2.0
1.6
1.2
0.8
0.4
0
**
*
*
**
*
Contralateral cortex
Lesion cortex
Prescan
12 hours
24 hours
48 hours
3 days
7 days

B

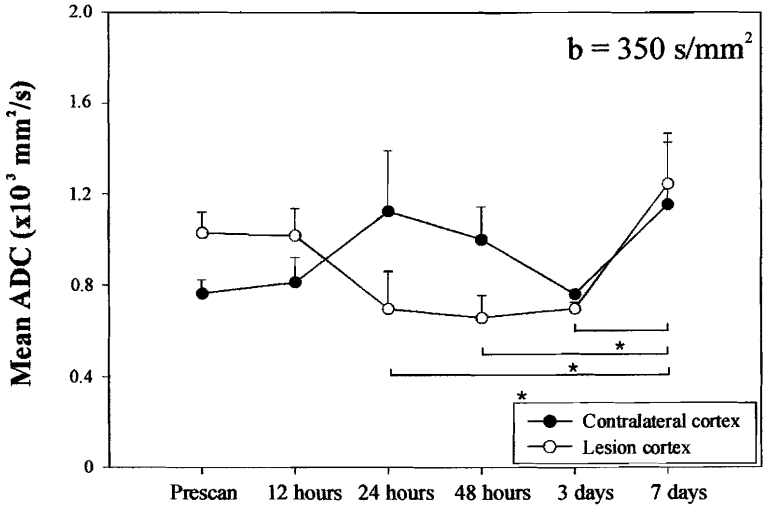
b = 350 s/mm²
Mean ADC (x10⁻³ mm²/s)
2.0
1.6
1.2
0.8
0.4
0
*
*
*
Contralateral cortex
Lesion cortex
Prescan
12 hours
24 hours
48 hours
3 days
7 days

C

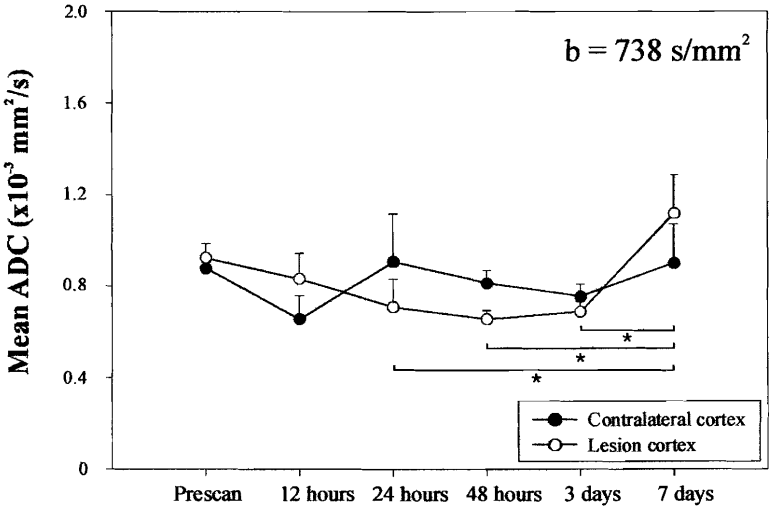
b = 738 s/mm²
Mean ADC (x10⁻³ mm²/s)
2.0
1.6
1.2
0.8
0.4
0
*
*
*
Contralateral cortex
Lesion cortex
Prescan
12 hours
24 hours
48 hours
3 days
7 days

Table 4: Quantitative evaluation of the mean ADC (± SEM) in the lesion and homologous contralateral region of interest in devascularized animals treated with saline at different b-values. [1]

SALINE (n = 6)	Mean ADC (± SEM) ($\times 10^{-3}$ mm^2/s)					
	b = 110 s/mm^2		b = 350 s/mm^2		b = 738 s/mm^2	
Observation Time	**Lesion side**	**Contralateral side**	**Lesion side**	**Contralateral side**	**Lesion side**	**Contralateral side**
Prescan	1.12 ± 0.09	1.12 ± 0.01	1.03 ± 0.09	0.77 ± 0.07	0.93 ± 0.06	0.88 ± 0.03
12 hours	0.86 ± 0.10 *	0.62 ± 0.01*	1.02 ± 0.12	0.82 ± 0.11	0.83 ± 0.11	0.66 ± 0.10
24 hours	0.76 ± 0.01 *‡	1.33 ± 0.21‡	0.70 ± 0.16	1.13 ± 0.26	0.71 ± 0.12	0.91 ± 0.21
48 hours	0.76 ± 0.09 *	1.07 ± 0.33	0.66 ± 0.10	1.00 ± 0.14	0.66 ± 0.04‡	0.81 ± 0.06‡
3 days	0.46 ± 0.01 *‡	0.87 ± 0.07‡	0.70 ± 0.02	0.76 ± 0.02	0.69 ± 0.04	0.76 ± 0.05
7 days	1.00 ± 0.10	0.91 ± 0.18	1.25 ± 0.18	1.16 ± 0.31	1.12 ± 0.12	0.90 ± 0.17

[1]Values in a column followed by an * are significantly different from the prescan value at the 5% level according to a repeated measure one-way ANOVA followed by individual Student-Newman-Keuls comparisons. Values followed by a ‡ are significantly different than the ROI in the opposite hemisphere at a 5% level according to a paired t-test.

were a significantly ($p<0.05$) different from the lesion ADC value at 24, 48 hours and 3 days (Figure 32 C). In the contralateral ROI, no significant changes in ADC were found (Figure 32 C). When the ADC of both the contralateral and lesion ROIs were compared, there was a significant ($p<0.05$) difference in these ADC values at 48 hours (Table 4).

5.2.1.2 DMSO Treatment

A second group of 7 animals underwent cortical devascularization followed by two injections of 1% DMSO vehicle at 1 and 12 hours after surgery. Again, 2 animals were removed from the study, as their prescan values were 2 standard deviations above the mean.

The b = 19 s/mm^2 images show a small, superficial area of hyper-intensity within the lesion area at 24 (Figure 33 G) and 48 hours (Figure 33 J). By 3 days, this hyper-intense region is very superficial (Figure 33 M) and by 7 days, there are no longer any signal intensity changes in the b = 19 s/mm^2 images (Figure 33 P). With the addition of the diffusion gradients (i.e. 350 s/mm^2), the lesion area was also hyper-intense at 24 (Figure 33 H) and 48 hours (Figure 33 K) but by 3 days there was no longer any hyper-intensity within the lesion area (Figure 33 N). After 7 days, the lesion was no longer hyper-intense, however, a diffuse increase in signal intensity could be found throughout the entire ipsilateral and much of the contralateral hemisphere (Figure 33 Q). The corresponding ADC maps confirmed that the increase in signal intensity observed at 24 and 48 hours were the result of a decrease in diffusion (Figure 33 I, L). After 7 days, tissue within the lesion area had herniated (Figure 33 P - R); however this was not

Figure 33: Diffusion un-weighted (b = 19 s/mm^2), weighted (b = 350 s/mm^2), and ADC map images of animals injected with DMSO at 1 and 12 hours after cortical devascularization. The un-weighted, weighted and ADC map images are typical for the prescan (A - C) group. A region of increased signal intensity corresponding to the lesion area (arrows) is observed in both the un-weighted and weighted images at 24 (G, H) and 48 hours (J, K). In contrast, the ADC maps show the lesion as an area of decreased signal intensity (arrows) at 24 (I) and 48 (L) hours. After 7 days there was no longer an increase in signal intensity in the un-weighted image (P) however, the weighted image (Q) and ADC map (R) show an area of diffuse diffusion restriction in the cortex of the ipsilateral hemisphere. Scale bar = 1 cm.

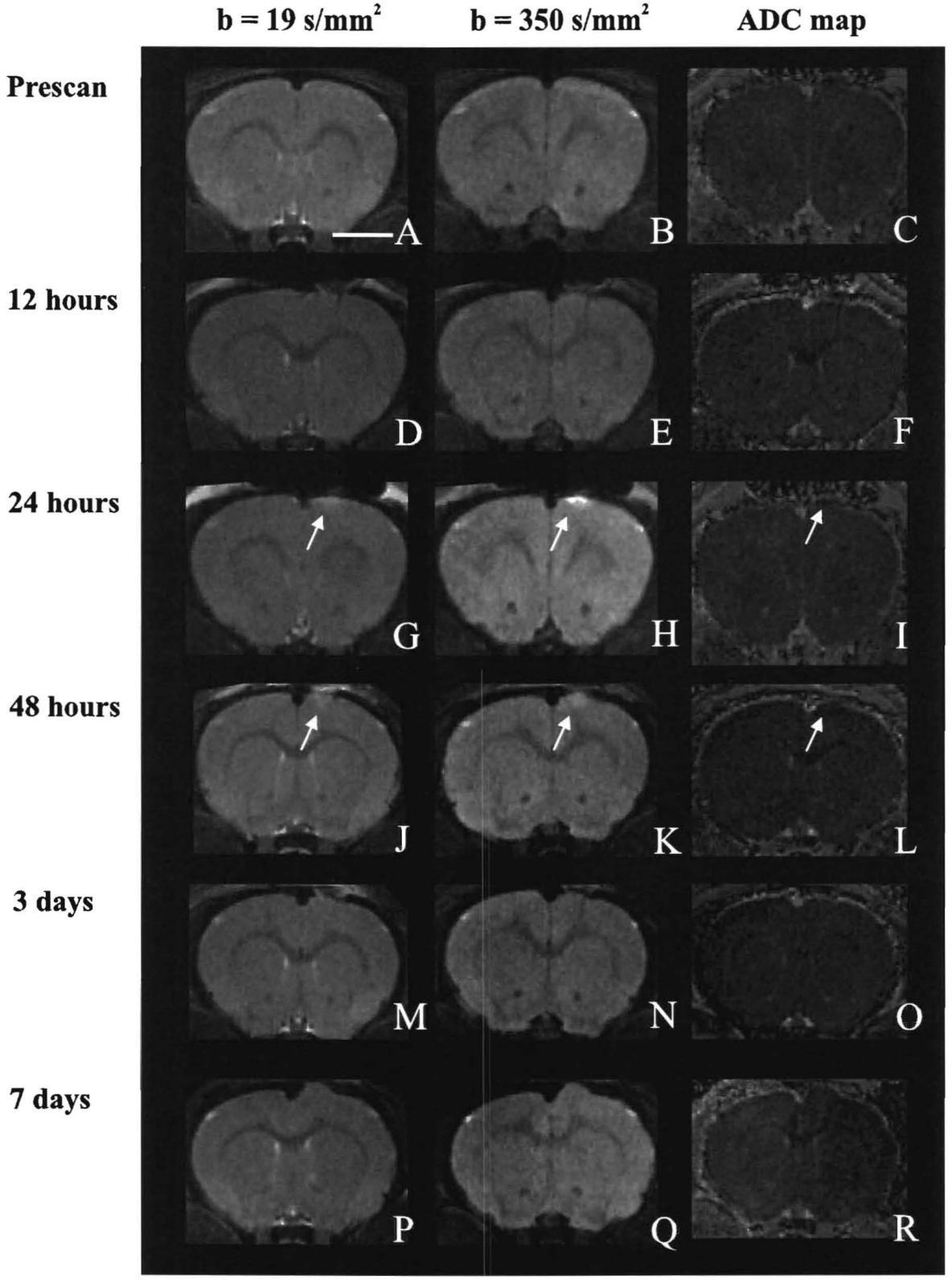
b = 19 s/mm²
b = 350 s/mm²
ADC map
Prescan
12 hours
24 hours
48 hours
3 days
7 days
A
B
C
D
E
F
G
H
I
J
K
L
M
N
O
P
Q
R

accompanied by an increase in signal intensity at either b = 19 s/mm^2 or 350 s/mm^2.

The mean ADC of both the lesion and contralateral ROI were calculated using each b-value and then plotted over time. With a b-value of 110 s/mm^2, there were no significant ($p<0.05$) changes in the ADC of the lesion ROI detected at any time point after the injury and subsequent DMSO injections (Figure 34 A). In addition, there was no significant change in ADC in the contralateral area at any of the time points studied (Figure 34 A). When the ADC of the contralateral and lesion areas was compared, a significant ($p<0.05$) difference was found at 7 days (Table 5).

At a b-value of 350 s/mm^2, there was also no significant decrease in the ADC of the lesion or contralateral area at any time point during the study (Figure 34 B). When the contralateral and lesion ROIs were compared, there was a significant ($p<0.05$) difference in ADC at 3 days after injury and DMSO injection (Table 5).

Using a b-value of 738 s/mm^2, there was no significant decrease in the ADC of the lesion or contralateral ROI at any time after injury, when compared the prescan ADC value (Figure 34 C). However, when the contralateral and lesion areas were compared, there was a significant ($p<0.05$) difference in the ADC after 3 days (Table 5).

5.2.1.3. APTRA-AM Treatment

A third group of animals (n = 8) was injected with APTRA-AM (40 mg/ml) at 1 and 12 hours after cortical devascularization. Two animals were also removed from this study as they both contained incomplete temporal data sets.

The b = 19 s/mm^2 images show a small area of hyper-intensity in the lesion area at 12 hours (Figure 35 D) after injury. With the addition of the diffusion gradients, a

Figure 34: Mean ADC (mm^2/s ±SEM) versus observation time of the contralateral and lesion ROI of DMSO treated animals collected at b = 110 s/mm^2 (A), b = 350 s/mm^2 (B), or b = 738 s/mm^2 (C). At no time was there a statistically significant change in the ADC of the lesion or contralateral ROI, compared to the prescan ADC values. Moreover, increasing the b-value did not uncover any statistically significant changes in ADC.

A

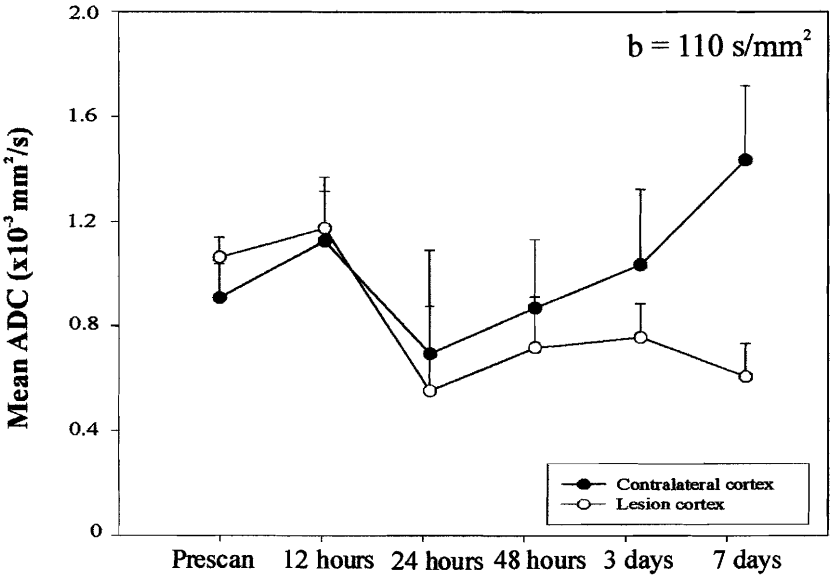
b = 110 s/mm²
Mean ADC (x10⁻³ mm²/s)
2.0
1.6
1.2
0.8
0.4
0
Contralateral cortex
Lesion cortex
Prescan
12 hours
24 hours
48 hours
3 days
7 days

B

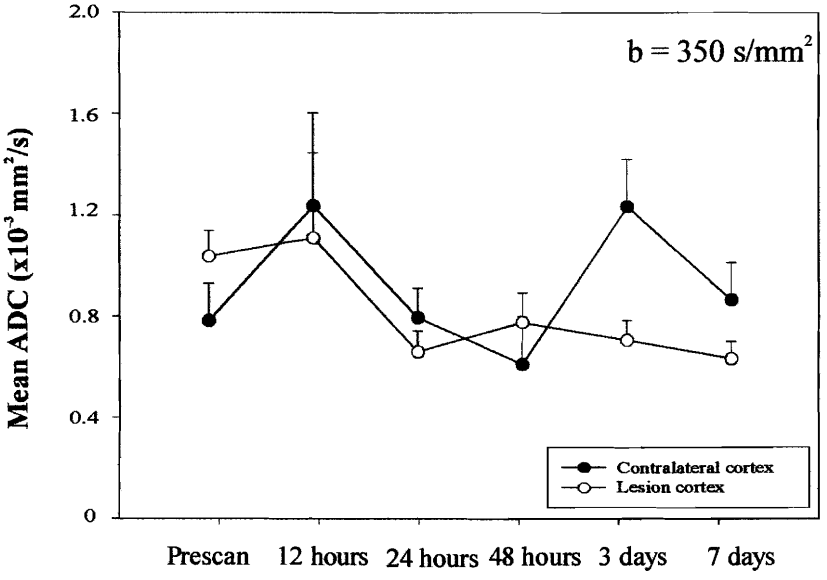
b = 350 s/mm²
Mean ADC (x10⁻³ mm²/s)
2.0
1.6
1.2
0.8
0.4
0
Contralateral cortex
Lesion cortex
Prescan
12 hours
24 hours
48 hours
3 days
7 days

C

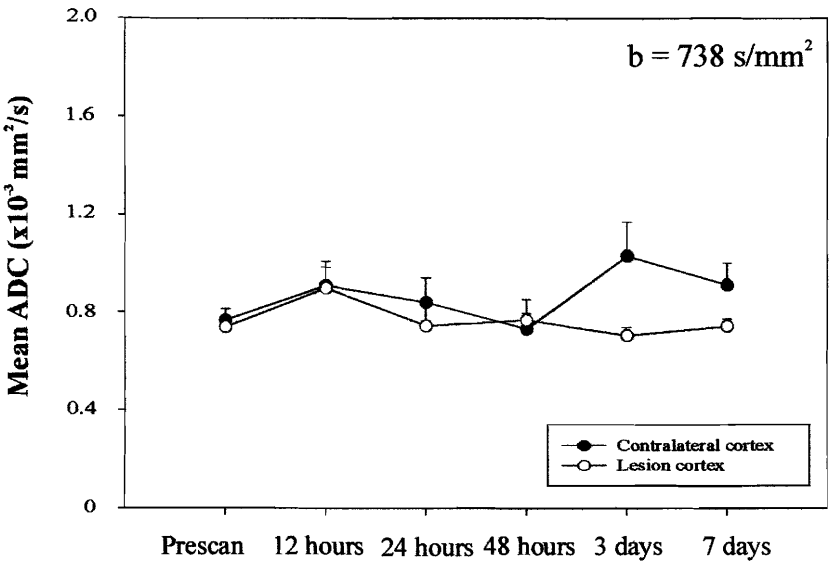
b = 738 s/mm²
Mean ADC (x10⁻³ mm²/s)
2.0
1.6
1.2
0.8
0.4
0
Contralateral cortex
Lesion cortex
Prescan
12 hours
24 hours
48 hours
3 days
7 days

Table 5: Quantitative evaluation of the mean ADC (± SEM) in the lesion and homologous contralateral region of interest in devascularized animals treated with DMSO at different b-values. [1]

DMSO (n = 5)	Mean ADC (± SEM) ($\times 10^{-3}$ mm^2/s)					
	b = 110 s/mm²		**b = 350 s/mm²**		**b = 738 s/mm²**	
Observation Time	**Lesion side**	**Contralateral side**	**Lesion side**	**Contralateral side**	**Lesion side**	**Contralateral side**
Prescan	0.75 ± 0.08	0.55 ± 0.14	0.78 ± 0.07	0.76 ± 0.07	0.74 ± 0.07	0.77 ± 0.05
12 hours	1.10 ± 0.12	1.06 ± 0.20	1.09 ± 0.26	1.19 ± 0.29	0.89 ± 0.09	0.91 ± 0.10
24 hours	0.58 ± 0.45	0.70 ± 0.15	0.74 ± 0.06	0.84 ± 0.09	0.75 ± 0.02	0.84 ± 0.10
48 hours	0.72 ± 0.16	0.85 ± 0.22	0.83 ± 0.09	0.70 ± 0.15	0.77 ± 0.08	0.73 ± 0.06
3 days	0.75 ± 0.11	0.98 ± 0.24	0.77 ± 0.06‡	1.18 ± 0.15‡	0.71 ± 0.03‡	1.03 ± 0.14‡
7 days	0.63 ± 0.10‡	1.32 ± 0.28‡	0.72 ± 0.05	0.90 ± 0.11	0.74 ± 0.03	0.91 ± 0.09

[1]Values in a column followed by an * are significantly different from the prescan value at the 5% level according to a repeated measure one-way ANOVA followed by individual Student-Newman-Keuls comparisons. Values followed by a ‡ are significantly different than the ROI in the opposite hemisphere at a 5% level according to a paired t-test.

Figure 35: Diffusion un-weighted (b = 19 s/mm^2), weighted (b = 350 s/mm^2), and ADC map images of animals injected with APTRA-AM at 1 and 12 hours after cortical devascularization. The un-weighted, weighted and ADC map images are typical for the prescan (A - C) group. A region of increased signal intensity corresponding to the lesion area (arrows) is observed in both the un-weighted and weighted images at 12 hours (D, E). In contrast, the ADC maps show the lesion as an area of decreased signal intensity (arrows) at 12 hours (F). After 12 hours there was no longer an increase in signal intensity in the un-weighted, weighted or ADC map images despite the presence of a small tissue herniation on the surface of the lesion cortex (G- I, J – L). By 3 days the herniation had disappeared and was replaced by a small depression in the cortical surface (P, Q). Scale bar = 1 cm.

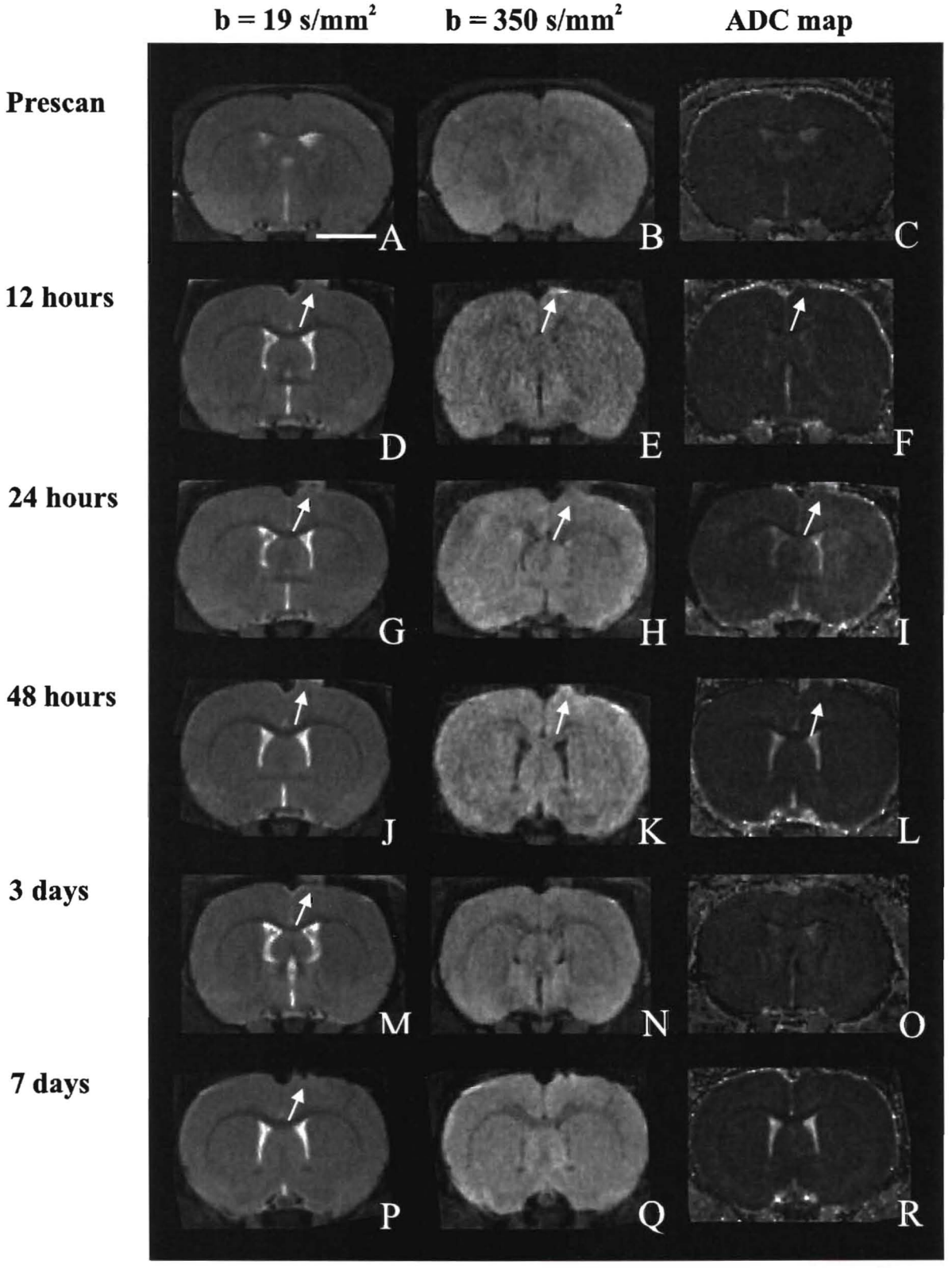
b = 19 s/mm²
b = 350 s/mm²
ADC map
Prescan
12 hours
24 hours
48 hours
3 days
7 days
A
B
C
D
E
F
G
H
I
J
K
L
M
N
O
P
Q
R

very small, superficial area of hyper-intensity was also observed in the lesion area at 12 hours (Figure 35 E). The corresponding ADC maps confirmed that this increase in signal intensity was the result of a decrease in diffusion (Figure 35 F). Interestingly, the b = 19 s/mm^2 images clearly show the beginnings of a tissue herniation within the lesion area beginning at 12 hours and resolving by 3 days (Figure 35 D, G, J, M). After 7 days, the cortical surface appeared to contain a small depression (Figure 35 P, Q). These morphological changes occurred in the absence of any MR detectable diffusion changes. The mean ADC values of each ROI were calculated for each b-value and then plotted over time.

Using a b-value of 110 s/mm^2, there were no significant ($p<0.05$) changes in the ADC of the lesion ROI at any time point after the injury (Figure 36 A). In addition, there was no significant change in ADC of the contralateral ROI at any time point (Figure 36 A).

When the contralateral and lesion ROI were compared, there was a significant ($p<0.05$) difference at 48 hours and a highly significant ($p<0.001$) difference at 3 days after injury and APTRA-AM injections (Table 6).

Using a b-value of 350 s/mm^2, there was also no significant decrease in the ADC of the lesion or contralateral area at any time point after injury and APTRA-AM injection (Figure 36 B). However, when the contralateral and lesion ROIs were compared, there was a significant ($p<0.05$) difference at 3 days (Table 6).

In addition, at the highest b-value (738 s/mm^2), there was no significant decrease in the ADC of the lesion or contralateral ROI at any time after injury, when compared

Figure 36: Mean ADC (mm^2/s ±SEM) versus observation time of the contralatera
lesion ROI of APTRA-AM treated animals collected at b = 110 s/mm^2 (A), b = 35
s/mm^2 (B), or b = 738 s/mm^2 (C). At no time was there a statistically significant c
in the ADC of the lesion or contralateral ROI, compared to the prescan ADC valu
Moreover, increasing the b-value did not uncover any statistically significant chan
ADC.

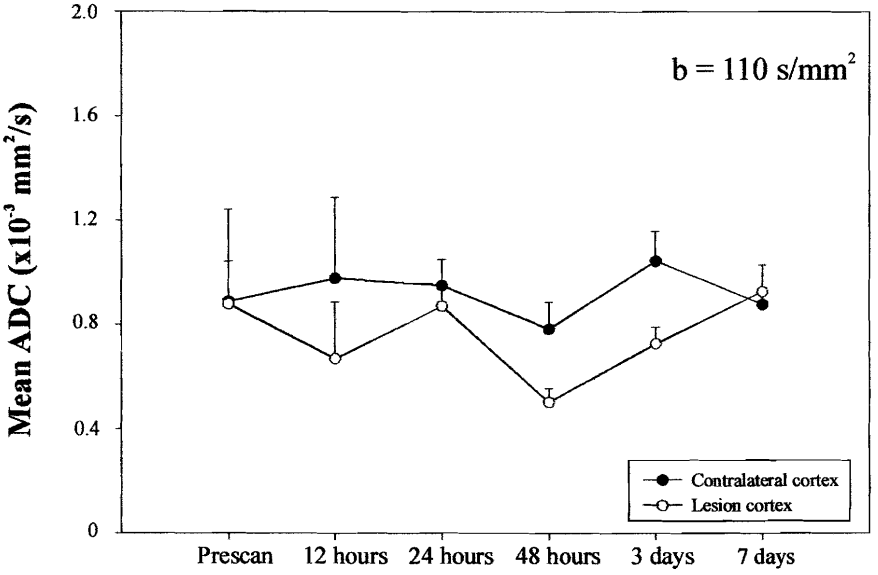
b = 110 s/mm²
Mean ADC (x10⁻³ mm²/s)
2.0
1.6
1.2
0.8
0.4
0
Contralateral cortex
Lesion cortex
Prescan
12 hours
24 hours
48 hours
3 days
7 days

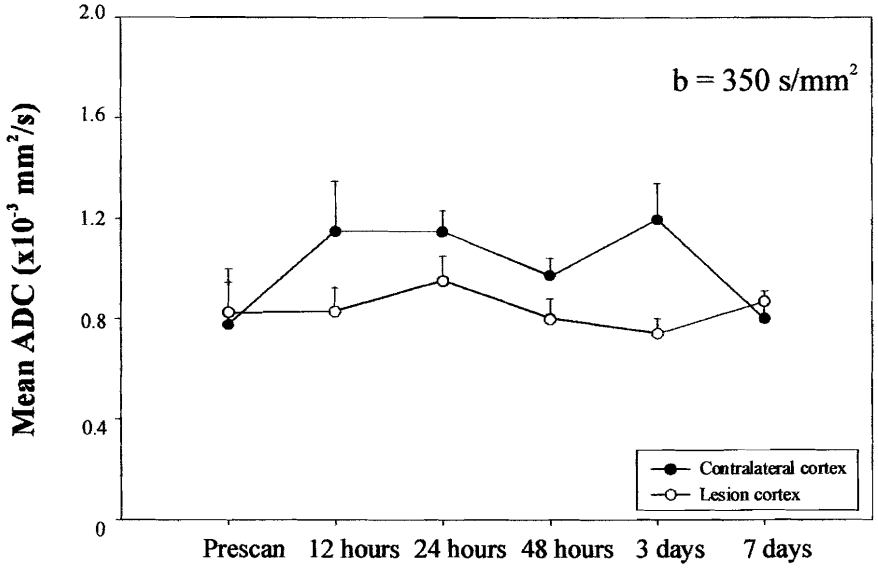
b = 350 s/mm²
Mean ADC (x10⁻³ mm²/s)
2.0
1.6
1.2
0.8
0.4
0
Contralateral cortex
Lesion cortex
Prescan
12 hours
24 hours
48 hours
3 days
7 days

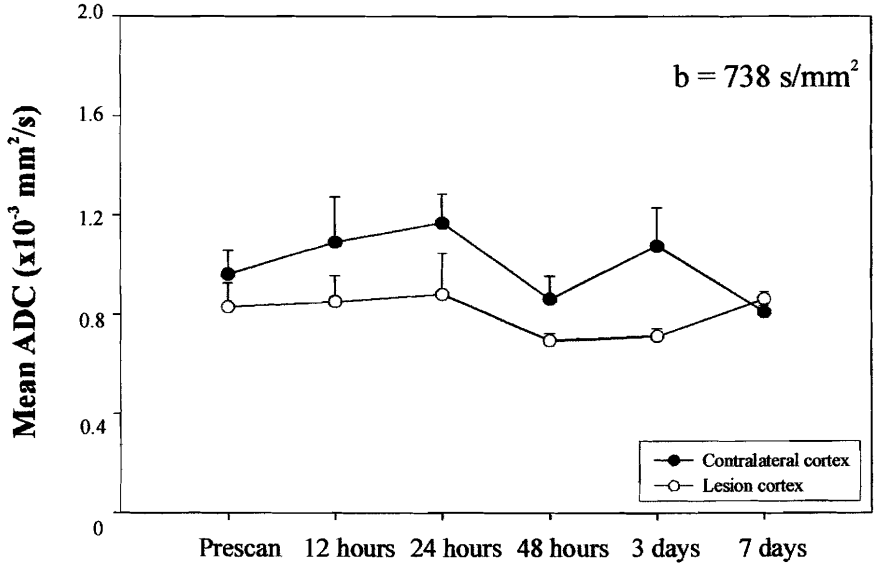
b = 738 s/mm²
Mean ADC (x10⁻³ mm²/s)
2.0
1.6
1.2
0.8
0.4
0
Contralateral cortex
Lesion cortex
Prescan
12 hours
24 hours
48 hours
3 days
7 days

Table 6: Quantitative evaluation of the mean ADC (± SEM) in the lesion and homologous contralateral region of interest in devascularized animals treated with APTRA-AM at different b-values. [1]

APTRA-AM (n = 6)	Mean ADC (± SEM) ($\times 10^{-3}$ mm^2/s)					
	b = 110 s/mm²		**b = 350 s/mm²**		**b = 738 s/mm²**	
Observation Time	**Lesion side**	**Contralateral side**	**Lesion side**	**Contralateral side**	**Lesion side**	**Contralateral side**
Prescan	0.88 ± 0.36	0.89 ± 0.16	0.82 ± 0.09	0.78 ± 0.05	0.96 ± 0.001	0.73 ± 0.06
12 hours	0.67 ± 0.22	0.98 ± 0.31	0.83 ± 0.05	1.15 ± 0.20	1.09 ± 0.18	0.85 ± 0.10
24 hours	0.87 ± 0.18	0.95 ± 0.01	0.95 ± 0.08	1.15 ± 0.08	1.17 ± 0.12	0.88 ± 0.16
48 hours	0.50 ± 0.05‡	0.78 ± 0.10‡	0.80 ± 0.08	0.97 ± 0.07	0.86 ± 0.09	0.70 ± 0.02
3 days	0.73 ± 0.06‡	1.04 ± 0.01‡	0.74 ± 0.06‡	1.2 ± 0.14‡	1.08 ± 0.15‡	0.71 ± 0.03‡
7 days	0.93 ± 0.10	0.88 ± 0.04	0.87 ± 0.04	0.80 ± 0.01	0.81 ± 0.04	0.86 ± 0.03

[1]Values in a column followed by an * are significantly different from the prescan value at the 5% level according to a repeated measure one-way ANOVA followed by individual Student-Newman-Keuls comparisons. Values followed by a ‡ are significantly different than the ROI in the opposite hemisphere at a 5% level according to a paired t-test.

the prescan ADC value (Figure 36 C). However, when the contralateral and lesion ROIs were compared, there was a significant ($p<0.05$) difference in the ADC at the 3 day time point (Table 6).

5.2.1.4 Comparison Between Treatment Groups

The ADC values obtained at each b-value and in each treatment group were compared to determine if these values were significantly ($p<0.05$) different from one another. In the data set collected at b = 110 s/mm^2, the lesion ADC of the saline group was significantly lower than the lesion ADC of the DMSO treatment groups 3 days after injury (Table 7). In addition, the lesion ADC of the saline group was significantly lower than the lesion ADC of the APTRA-AM treatment group at this time point (Table 7). In the data collected at b = 350 s/mm^2, the lesion ADC of the saline group was significantly lower than both the DMSO and APTRA-AM treatment groups 7 days after injury (Table 7). However, in the data collected at 738 s/mm^2, there were no significant differences in the lesion ADC of any treatment groups, at any of the time points studied.

In the contralateral ROI, there was a significant difference between the saline and DMSO groups at the 24 hour time point of the b = 110 s/mm^2 data set (Table 7). At b = 350 s/mm^2, there was also a significant difference between these two treatment groups but at the 3 day time point (Table 7).

5.2.2 Morphological Changes

All morphological assessments examining the efficacy of APTRA-AM treatment were done at 7 days after injury.

Table 7: List of the significantly different comparisons between the individual treatment groups.

b-value	Treatment groups	Time point	Student's t-test *(p)*
b = 110 s/mm^2	Saline vs. DMSO (contralateral ROI) Saline ADC lower than DMSO	24 hour	0.028
	Saline vs. DMSO (lesion ROI) Saline ADC lower than DMSO	3 day	0.024
	Saline vs. APTRA-AM (lesion ROI) Saline ADC lower than DMSO	3 day	0.012
b = 350 s/mm^2	Saline vs. DMSO (contralateral ROI) Saline ADC lower than DMSO	3 day	0.035
	Saline vs. DMSO (lesion ROI) Saline ADC lower than DMSO	7 day	0.019
	Saline vs. APTRA-AM (lesion ROI) Saline ADC lower than APTRA-AM	7 day	0.034
b = 738 s/mm^2	none		

5.2.2.1 Saline Treatment

Cortical devascularization followed by two injections of saline (1 and 12 hours after injury) resulted in the formation of a pan-necrotic infarct that appeared as a large cyst surrounded by tissue containing numerous necrotic cells, vacuolations and inflammatory cells 7 days after injury (Figure 37). The mean area (± SEM) of these lesions was 0.53 ± 0.06 mm^2 (Figure 38).

This observation was consistent with all animals that were untreated after the injury (see Figure 19 D). However, the mean area (± SEM) of these lesions was 1.09 ± 0.16 mm^2 (Figure 38).

Similar to the untreated animals (see section 5.1.2.1), saline injection did not result in ongoing neurodegeneration that could be observed by Fluoro-Jade staining of neurons within, rostral or caudal to the infarct 7 days after injury. However, numerous inflammatory cells and the surrounding infarct debris did stain with the Fluoro-Jade.

The saline treated animals also showed a similar astrocyte and microglial activation profile at 7 days as the untreated ischemic animals (Figure 39 A, B). Specifically, there was extensive GFAP immunoreactivity surrounding the infarct and in the contralateral hemisphere. This included a band of reactive astrocytes immediately adjacent to the infarct. OX-42 immunoreactivity was restricted to the amoeboid microglia and activated macrophages within and surrounding the infarct (Figure 39 B).

As expected, the neuroinflammatory response included numerous ED-1 positive phagocytic cells throughout the infarct debris and peri-infarct areas (Figure 39 C). Neurons of both the ipsilateral and contralateral hemisphere had faint cytoplasmic NF-κB immunoreactivity with an increase in staining intensity and the appearance of nuclear

NF-κB immunoreactivity in cells within and immediately adjacent to the infarct (Figure 39 D).

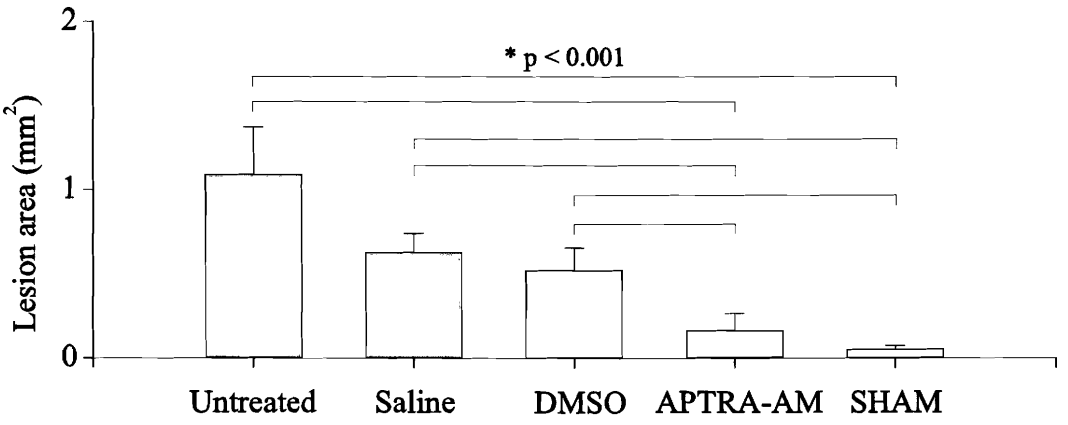

Figure 38: Graph comparing the mean lesion area ($mm^2 \pm$ SEM) in un-treated and sham animals versus those treated with saline, 1% DMSO or APTRA-AM (40 mg/kg). The area was measured on histological sections taken 7 days after the induction of ischemia. The asterisk denotes statistical significance (one way ANOVA, $p<0.001$).

5.2.2.2 DMSO Treatment

Two injections of 1% DMSO at 1 and 12 hours after injury resulted in a 56% reduction in mean lesion volume (0.43 ± 0.07 mm^2) when compared to the un-treated animals (see Figure 38). Despite the reduction in lesion volume, the tissue was also pan-necrotic and contained necrotic nuclei, inflammatory cell infiltrate and vacuolations. However, the lesion involved fewer cortical layers than either the saline injected or un-treated animals (Figure 40). As with the saline treatment group, there was no evidence of ongoing neurodegeneration at 7 days after injury as determined by the absence of Fluoro-Jade stained neurons.

Animals injected with DMSO also displayed significant GFAP immunoreactivity throughout both hemispheres (Figure 41 A) while the OX-42 immunoreactivity was restricted to activated microglia and macrophages within and the area adjacent to the infarct (Figure 41 B). Extensive ED-1 immunoreactivity localized to both macrophages and activated microglia was also observed in the infarct and peri-infarct regions (Figure 41 C). NF-κB immunoreactivity was also found throughout both hemispheres and localized to both the cytoplasm and nuclei of immunoreactive cells (Figure 41 D).

5.2.2.3 APTRA-AM Treatment

Injections of APTRA-AM (40mg/kg) at 1 and 12 hours after injury, significantly ($p<0.001$) reduced the area of the lesion by 85% (0.15 ± 0.05 mm^2) when compared to the un-treated animals (Figure 38). Lesions in the APTRA-AM treated animals contained little or no cell death or inflammatory cell infiltrate (Figure 42, 43). The most

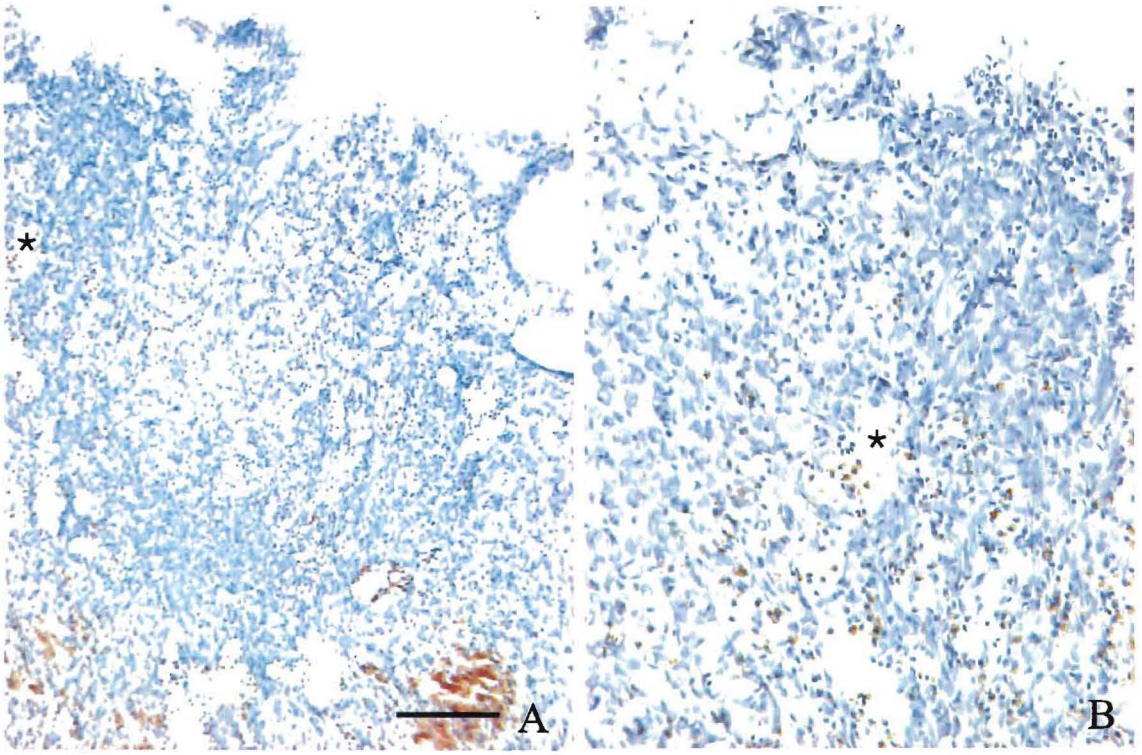

Figure 40: Representative photomicrographs of cresyl violet stained sections from animals injected with 1% DMSO (A, B). Animals were injected at 1 and 12 hours after surgery and show similar morphological changes as the un-treated and saline injected animals. The image on the left (4X) shows a large infarct that involves multiple cortical layers (A) and the image on the right (20X) shows more clearly that the infarct is filled with numerous necrotic nuclei and inflammatory cells (B). The asterisk denotes the area where the higher power image is taken from. Scale bar = 100 μm.

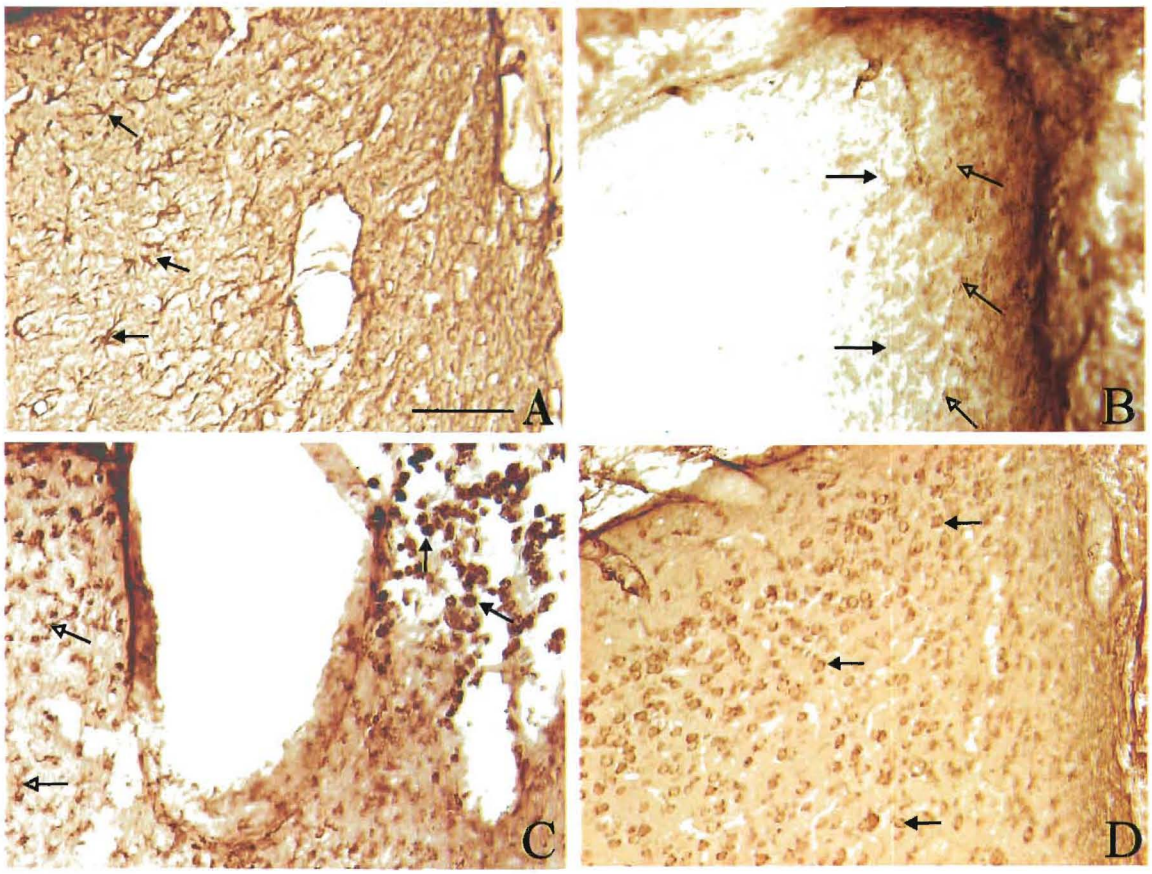

Figure 41: Tissue from the ipsilateral cortex of DMSO treated devascularized animals immunostained for GFAP (A), OX-42 (B) ED-1 (C) and NFκB (p65 sub-unit) (D) 7 days after injury. GFAP immunostaining shows substantial reactive astrogliosis in the area adjacent to the infarct (A, arrows). OX-42 immunoreactivity could be found in both microglial cells (B, closed arrows) and invading macrophages (B, open arrows) within and adjacent to the infarct. Numerous ED-1 positive phagocytic activated microglia (C, open arrows) and macrophages (C, closed arrows) were found within and surrounding the infarct. NFκB immunoreactivity was found in the cytoplasm and nucleus of neurons surrounding the infarct (D, arrows). Scale bar = 100 μm.

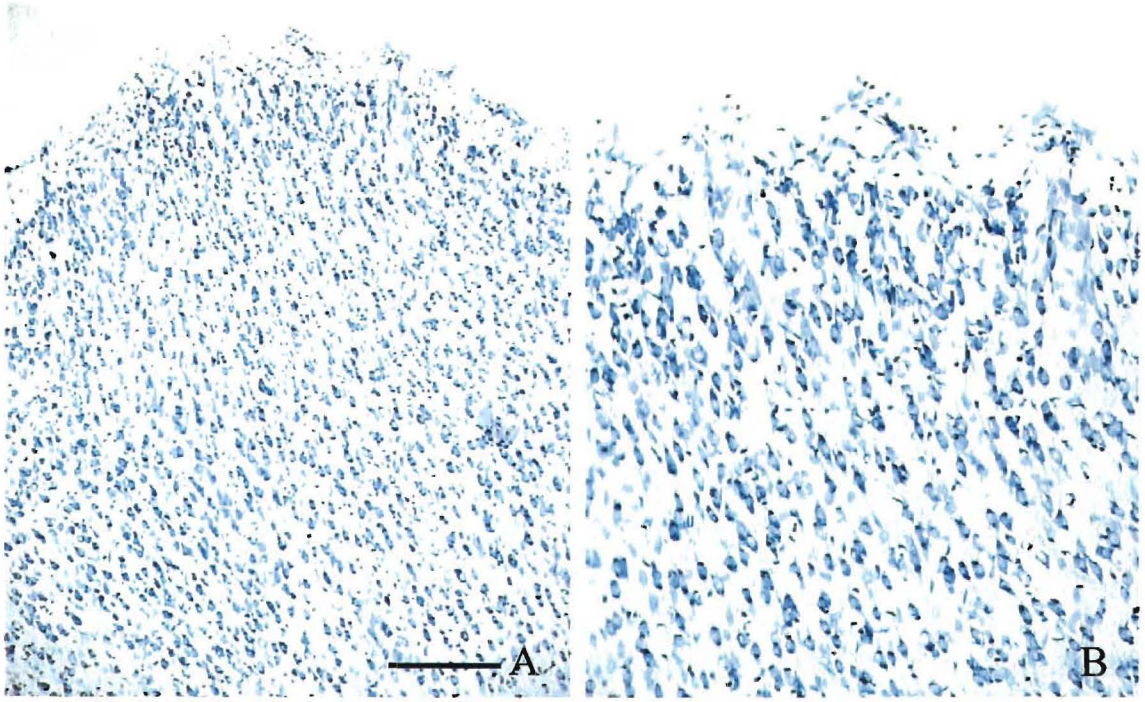

Figure 42. Representative photomicrographs of cresyl violet stained ipsilateral cortex of animals injected with APTRA-AM (40 mg/kg) 7 days after injury. These animals rarely exhibited morphological and pathological changes in the ipsilateral cortex. The image on the left is at a low magnification (4X) to show how the cortex herniated (A) while the higher magnification (20X) image on the right shows the disruption of the outer molecular layer and some minor cell death within the herniated region (B). The amount of damage in these animals is minimal compared to the extensive damage observed in the saline or DMSO treated animals. Scale bar = 100 μm.

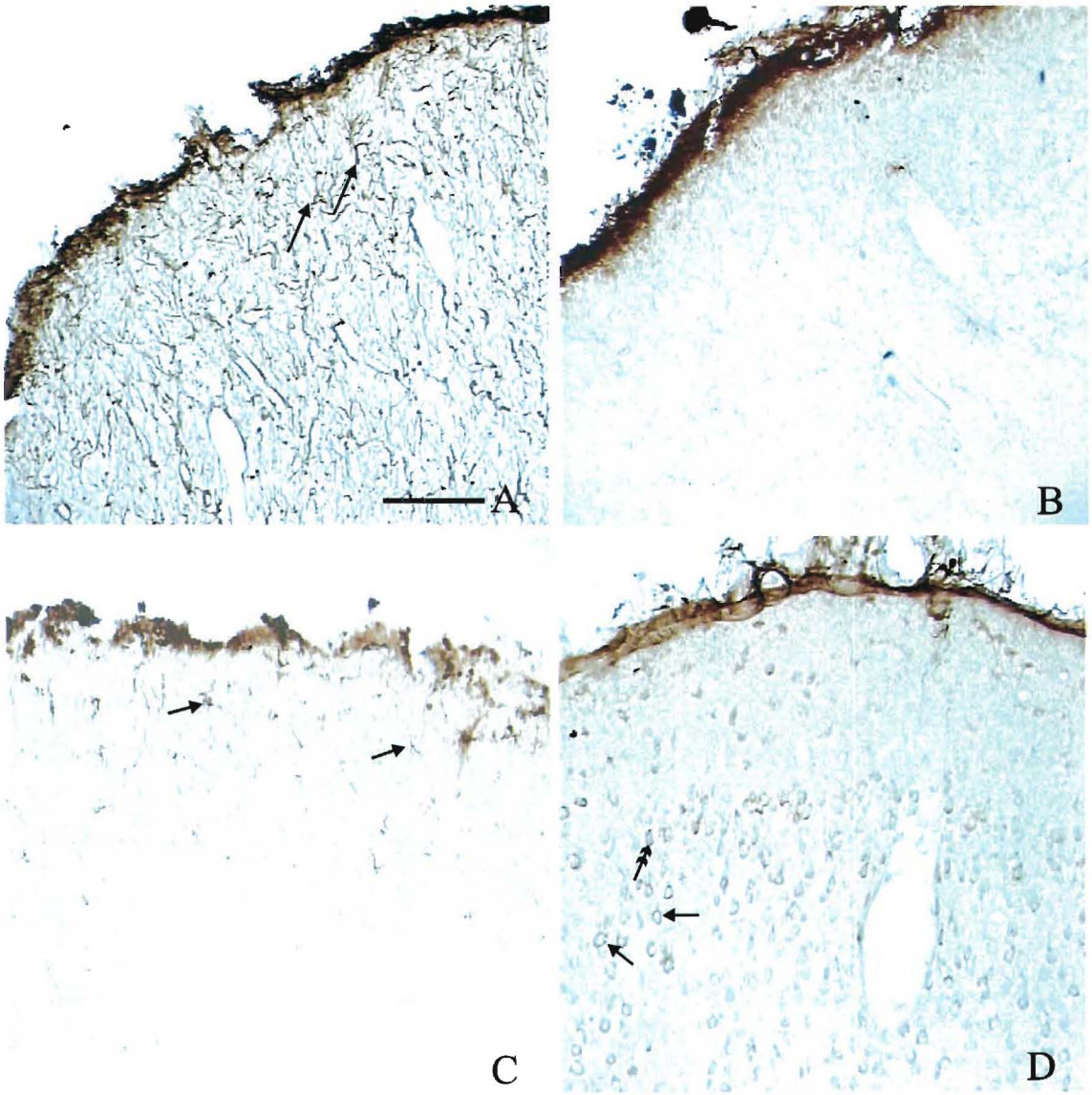

Figure 43. Tissue from the ipsilateral cortex of APTRA-AM treated animals 7 days after injury and immunostained for GFAP (A), OX-42 (B) ED-1 (C) and NF-κB (p65 sub-unit) (D). GFAP immunostaining shows substantial reactive astrogliosis in the area inferior to the injury site (A, arrows). Faint OX-42 immunoreactivity could be found in the microglial cells (B). ED-1 positive activated microglia are found only inferior to the surgery site(C). Note that there are no phagocytes present (C). Both cytoplasmic (D, closed arrows) and nuclear (D, double headed arrows) NF-κB immunoreactivity was observed in the neurons. Scale bar = 100 μm.

significant morphological change consisted of a herniation of the tissue into the surgical opening in the skull (5 out of 10) or some minor disruption of the outer molecular layer (3 out of 10). Again, there was no evidence of neurodegeneration using Fluoro-Jade histochemistry.

Seven days after injury and treatment with APTRA-AM, there was extensive GFAP immunoreactivity observed in both hemispheres. The entire ipsilateral hemisphere including the herniated tissue exhibited reactive astrocytes (Figure 43 A). However, there was only very faint OX-42 immunoreactivity (Figure 43 B). ED-1 immunoreactivity in APTRA-AM rats was also reduced compared to untreated, saline, or DMSO animals and limited to microglial cells within the outer molecular layer of the herniated tissue (Figure 43 C, arrows). In some cases, ED-1 positive macrophages could be found on the surface of the brain. NF-κB immunoreactivity was found in neurons throughout both hemispheres, although it was localized primarily to the cytoplasm of these cells (Figure 43 D).

6.0 Discussion

In the studies reported here, we have characterized the temporal and spatial evolution of a cortical devascularization injury. Notable observations from our studies include 1) that DWI is the preferred method for detecting pathological changes associated with a cortical devascularization injury, 2) changes in tissue diffusion are not restricted to the area affected by the interruption in blood flow but can also be found in remote areas, 3) cortical devascularization results in early glial activation and delayed neuronal cell death, 4) the onset of cell death is accompanied by an inflammatory response that features phagocytes and pro-inflammatory cytokine secretion. In addition, we have used this model to show that the cell permeant calcium buffer APTRA-AM is highly effective in preventing the neuronal cell death and accompanying inflammatory response associated with this injury, even when given after injury. Finally, APTRA-AM treatment also prevented those pathophysiological changes that can be observed by DWI. The following sections discuss these major findings.

6.1 Cortical Devascularization as a Model for Permanent Focal Ischemia

Various models are available to investigate the pathological processes that occur as the result of focal cerebral ischemia. Here we describe a brain injury model that exhibits a progression of events consistent with the development of a permanent focal

ischemic lesion, including cell death and infarct formation, the induction of an inflammatory response, and a decrease in ADC that returns to pre-injury levels.

Cortical devascularization involves the disruption of the microcirculation resulting in a small, cortical infarct. This model has several advantages over other models in that it involves simpler surgical techniques, it is not associated with any post-surgical complications, it produces a small cortical infarct whose size can be determined by the size of the vessel transected, and most importantly, it is highly reproducible. Finally, by completely transecting the vessel we are able to observe the progressive evolution of ischemic injury outside of the complicating effects of reperfusion. While this model is associated with a physical damage to a blood vessel, it should not be characterized as hemorrhagic as only rarely does it result in the accumulation of intracerebral blood.

6.2 MRI Changes Associated with Cortical Devascularization Induced Ischemia

The usefulness of DWI in identifying and localizing damage in animal models of cerebral ischemia is well documented (Moseley et al., 1990); (Benveniste et al., 1992); (Busza et al., 1992); (Minematsu et al., 1992); (van Bruggen et al., 1994); (Hoehn et al., 2001). Early changes in signal intensity on DW images have become the hallmark for the clinical identification of acute ischemia. In characterizing the cortical devascularization model as one of ischemic injury, we used DWI to non-invasively monitor the temporal and spatial evolution of the resultant injury. We also wanted to determine if DWI was sensitive to small ischemic injuries. Our results demonstrate that DWI is very effective and highly sensitive to early diffusional changes caused by this

type of injury. However the evolution of the diffusion changes is different than previously characterized models of ischemia, perhaps reflecting the difference in the amount of territory involved or perhaps the differences in the temporal profile of cellular changes (see section 5.1.2).

Cortical devascularization resulted in a decrease in the ADC of the affected area over the course of several weeks while the sham operated animals showed no significant change in ADC over the same observation period. A decrease in ADC occurs when tissue water experiences decreased mobility/movement. Several possible mechanisms have been proposed including a reduction in extracellular space and/or an increase in tortuosity (size and geometry of the extracellular space). These conditions occur when transmembrane ion shifts and astrocyte hypertrophy (Sykova, Chvatal, 1993); (Sykova, 1997) result in cellular swelling. However, in our model, the largest decrease in ADC was seen at 12 hours after injury prior to any histological evidence of cellular swelling or significant increases in astrocyte hypertrophy within the lesion area.

In addition to changes in tortuosity, ADC changes may reflect more discrete changes in the metabolic state of the tissue underlying the surgical site. Busza et al (1992) found that when using proton spectroscopy imaging, areas with an increased lactate signal, (which is indicative of neuronal death) corresponded to regions with decreased diffusion. Moreover areas of tissue acidosis have also been shown to correspond to areas of decreased ADC, suggesting that these changes may be indicative of tissue metabolic state (Sykova, Chvatal, 1993); (Kohno et al., 1995).

While the devascularization created a permanent lesion, tissue diffusional characteristics returned to pre-surgery levels after two weeks. This observation has been

made in previous DWI studies of ischemia; however, these models of ischemia report a rise in ADC that eventually surpasses that of the tissue ADC prior to injury. These studies suggest that the increase in ADC may be due to a loss of cell membrane integrity allowing for un-restrictive water movement within necrotic and/or fluid filled cystic regions (Gill et al., 1995); (Knight et al., 1994); (Matsumoto et al., 1995); (Rumpel et al., 1997). While the ADC values obtained in our experiments did not surpass the prescan ADC, it is likely that increased ADCs would be due to the formation of a pan-necrotic infarct.

In our study we observed a significant decrease in the ADC of the contralateral ROI, which we speculate is the result of transcallosal diaschisis. Diaschisis is defined as a temporary deactivation of an intact remote brain region connected to an area of damage (Andrews, 1991); (Feeney, Baron, 1986). In order to be considered diaschisis, the criteria set out by Kempinsky (1958) and Andrews (1991) must be met. First, there must be a well-circumscribed injury. Both the MR and histological studies identify a well-defined region of injury resulting from cortical devascularization. Second, diaschisis must occur at a distance from the injury. In this case, the remote area of injury occurs within the contralateral hemisphere in the homologous primary motor cortex. Third, there must be a neuronal basis for the depressive effects and the areas must have an anatomical connection. Both the lesion and the contralateral ROI were located in the frontal area 1 which receives afferents from both the ipsilateral and contralateral secondary motor cortices as well as the opposite primary motor cortex (M1) (Zilles, Wree, 1995). Finally the process must be reversible. This criterion was also met, as the decrease in ADC within the contralateral area was observed at 12 and 24 hours, which

then returned to prescan levels by 48 hours. While the significance of transcallosal diaschisis is unknown, it has been suggested that this phenomenon could be the underlying cause of post-ischemic epilepsy that develops in 14 – 28% of clinical cases (Kotila, Waltimo, 1992). Our animals did not develop focal epileptic seizures during the time they were studied (14 – 21 days). However, we conducted a small *in vivo* electrophysiological study of spontaneous activity in the Fr1 region, which did show some increase in electrical activity within the contralateral ROI after cortical devascularization (data not shown). Thus, transcallosal diaschisis provides an intriguing possible mechanism for the ADC alterations seen in the contralateral cortex. In addition, contralateral changes in ADC have also been reported in rat after a permanent MCA occlusion (Abe et al., 2000) as well as in a rat model of hypoxia-ischemia (D'Arceuil et al., 1999) and in both cases, these changes were similarly attributed to transcallosal diaschisis.

T2WI was used to identify regions affected by ischemic injury, although with much less reliability. Typically, T2WI highlights areas of edema that are thought to be associated with vasogenic edema and the onset of inflammation. However, unlike all other reports of imaging in ischemia (Minematsu et al., 1992); (Pierpaoli et al., 1993); (van Everdingen et al., 1998); (Li et al., 2000), we found no significant change in T2 relaxation at any time after injury, when compared to the images taken before the injury or when compared to the contralateral hemisphere. This suggests that vasogenic edema is likely not a significant part of the evolving pathophysiology of a cortical devascularization injury. While increasing the number of animals examined may have brought the T2 changes to significant levels, it is important to note that we observed a

decrease in T2 relaxation time. This means that within the lesion ROI, there was no significant accumulation of water; in fact the amount of water was reduced compared to both the contralateral hemisphere and the same ROI when examined prior to injury. While the mechanism behind this observation is unknown, we speculate that the decreased water accumulation in the infarct region may be a function of increased tissue viscosity due to a decrease in CSF flow and subsequent tissue alterations as a consequence of removing the meninges to access the pial vasculature. Alternatively, this decrease may be the result of a local accumulation in deoxyhemoglobin, as was proposed by Calamante et al. (1999) and Lythgoe et al. (2000) to explain the early decrease in T2 they observed after both permanent and partial MCA occlusion. This accumulation would create a susceptibility effect which would cause the dephasing of water spins as they diffused through the local field gradient created by the accumulation of deoxyhemoglobin (Calamante et al., 1999). Most importantly, the inability of T2WI to reliably detect changes associated with the formation of an infarct after cortical devascularization suggests that T2WI is severely limited in its ability to identify small, slowly developing permanent ischemic lesions.

A Gd-T1WI study at 24, 48 hours, 3 and 7 days was done to determine if changes in blood-brain barrier permeability contributed to the pathophysiological mechanisms behind a cortical devascularization injury. Our experiment did not reveal the presence of contrast agent within the parenchyma indicating that the parenchymal blood-brain barrier remained intact after a cortical devascularization injury. Interestingly, there was an accumulation of contrast within the meningeal space and cranial vault associated with the surgical site. The accumulation of contrast within these areas is most likely due to

leaky blood vessels associated with the surgical site. Taken together, the lack of T2 relaxation changes and the absence of parenchymal contrast accumulation strongly suggest that vasogenic edema does not contribute to the injury at any point during its temporal and spatial evolution.

MRI has proven useful in the detection of ischemic injury. However, our studies using DWI, T2WI, and Gd-T1WI to study small ischemic injuries suggests that only DWI reliably detects ischemic injury and only within the first 7 days before the ADC begins to normalize. However, the use of multiple imaging sequences provides a much clearer view of the potential physiological changes associated with the injury. For example, after a cortical devascularization injury, DWI identifies areas of decreased mobility that is not accompanied by large-scale changes in water accumulation or blood-brain-barrier permeability changes as assessed by both T2WI and Gd-T1WI. Therefore we are able to more closely focus our attention on processes that affect water mobility as possible causes of injury in this model. Most importantly, despite the fact that MRI, specifically DWI, clearly identifies areas compromised by the injury, what remains incomplete is an understanding of the interplay between evolving cellular pathology and changes in the mobility of water after the injury.

6.3 Histopathological Changes Associate with Cortical Devascularization Induced Ischemia

Cortical devascularization produced a circumscribed, permanent cortical lesion following disruption of a single descending pial vessel. Cresyl violet histochemistry was used to follow the evolution of this type of injury and clearly showed that the formation

of a pan-necrotic infarct was delayed until 48 hours after injury. Prior to this, the area affected by the surgery had only minor disruption of the outer molecular layer and some scattered necrosis. The delay between the time of injury and the onset of cell death is similar to what is observed in the 2-vessel occlusion models of forebrain ischemia where delayed cell death is observed in the selectively vulnerable CA1 region of the hippocampus (Lipton, 1999). However, the permanent interruption in blood flow more closely resembles the photothrombic and permanent MCA occlusion models of ischemia. This suggests that a cortical devascularization injury does not produce significantly large enough local changes in cerebral blood flow to cause immediate cell death. This is most likely the case as the pial network contains numerous anastamoses, which could maintain optimal collateral circulation, thus reducing the severity of the insult and ultimately the size of the infarct.

In an attempt to more carefully examine the time course of neuronal degeneration in this model, tissue from within the infarct as well as the 500 μm both rostral and caudal to the injury from each time point were stained with Fluoro-Jade. This stain has been reported to identify degenerating neurons by staining an as of yet uncharacterized, strongly basic "degeneration molecule" (Schmued et al., 1997). This protocol has been used in numerous animal models of neurotoxic injury (Schmued et al., 1997); (Bishop, Robinson, 2001), global ischemia (Larsson et al., 2001), transient ischemia (Butler et al., 2002), traumatic brain injury (Sato et al., 2001) and epilepsy (Poirier et al., 2000). However, we were unable to identify degenerating neurons within or surrounding the lesion at any time point after a cortical devascularization injury. A possible explanation is that cortical devascularization does not cause neurons to produce the "degeneration

molecule" that this stain binds to. Interestingly, we did observe Fluoro-Jade positive cells scattered throughout the infarct debris and in the surrounding peri-infarct areas that in subsequent immunohistochemistry experiments were determined to be ED-1 positive phagocytes and GFAP positive reactive astrocytes, respectively (Figure 21). Butler et al. (2002) also observed Fluoro-Jade positive astrocytes within the peri-infarct regions 14 and 21 days after transient MCA occlusion and concluded that perhaps the staining of these cells reflected some biochemical alteration as a result of activation or cellular damage.

In addition to characterizing both the morphological changes and pattern of neuronal cell death after a cortical devascularization injury, changes to the glial cell populations were also examined. It is well known that after injury, the CNS responds by activating both astrocytes and microglia. This results in changes to both the morphology and functional abilities of these cells that can be both beneficial and detrimental to recovery. For example, both cells release adhesion molecules and pro-inflammatory cytokines that may initiate an immune response, as well as secreting numerous cytotoxic agents (e.g. reactive oxygen species and proteases) that can mediate neuronal injury (Banati et al., 1993); (Eddleston, Mucke, 1993).

After cortical devascularization both the astrocytes and microglia responded to injury by proliferating and becoming activated. The timing, duration and general location of their activation differed slightly between the two cell types. Specifically, the microglial cells throughout the entire ipsilateral hemisphere and the contralateral medial cingulate gyrus and corpus callosum become activated within the first 12 – 24 hours. After 48 hours, these cells had lost their secondary arborizations and were located within

the edges of the developing infarct and surrounding peri-infarct areas. This was the typical microglia staining pattern in the tissue 3 and 7 days after injury. In contrast, a small amount of astrocyte activation was observed within the first 24 hours. These cells were mostly perivascular and were found scattered throughout both hemispheres. By 48 hours, the entire ipsilateral hemisphere and parts of the contralateral hemisphere contained reactive astrocytes. At later time points, astrocyte reactivity was localized primarily to the peri-infarct region forming a glial scar.

Activation of glial cells prior to infarct development has been previously observed after both permanent and transient MCAO (Clark et al., 1993); (Kato et al., 1996); (Davies et al., 1998); (Abraham, Lazar, 2000). The activation of microglia and perivascular astrocytes prior to significant amounts of neuronal death and inflammation suggest a key role for these cells in initiating the ensuing tissue damage, specifically the onset of an inflammatory response. It is interesting to point out that in many of the these studies the reactive cells were localized to areas that would eventually be incorporated into the infarct or in the area immediately adjacent to the infarct. While similar patterns were observed in our model, we noted glial cell activation throughout the entire ipsilateral hemisphere. We can only speculate why the entire ipsilateral hemisphere responded, but it may reflect the proliferation or signaling of glial cell populations after injury.

We also observed activation of both glial cell types in the contralateral hemisphere. Contralateral increases in both GFAP (Herrera, Cuello, 1992); (Clark et al., 1993) and OX-42 (Kato et al., 1996); (Davies et al., 1998); (Schroeter et al., 1999) immunoreactivity have been previously observed in other models of cerebral ischemia.

In our study, an increase in GFAP and OX-42 immunoreactivity was concentrated in the contralateral medial cingulate area, thalamus and corpus callosum. Thus both astrocytes and microglial activation occurred in areas that are anatomically connected to the injured area suggesting that the glia are responding to a change in activity between these two functionally connected areas (transcallosal diaschisis). Schroeter et al. (1999) suggested that the contralateral activation might be the result of fiber tract degeneration and retrograde cell death.

The purpose of characterizing the histopathological changes associated with a cortical devascularization injury was to correlate these cell structural and functional changes with the observed changes in water mobility (Figure 44). Significant diffusion changes were observed in the lesion ROI within the first 48 hours after which point the ADC began to recover. Histologically, both the microglial and astrocyte cell populations showed increased OX-42 and GFAP immunoreactivity with concomitant morphological changes within the first 48 hours. Taken together this suggests that the early hypertrophy and hyperplasia of both cell types may contribute to the decrease in water mobility observed by DWI. Between 48 hours and 7 days, the ADC began to recover towards pre-injury levels indicating increased water mobility within the lesion area. This increase corresponded to the significant loss of cells and an increase in the extracellular space within the lesion that was observed 48 hours, 3, and 7 days after injury. This suggests that the increase in ADC may be due to a reduction in the number of diffusion barriers (i.e. cell membranes) that occurs during the formation of a pan-necrotic infarct.

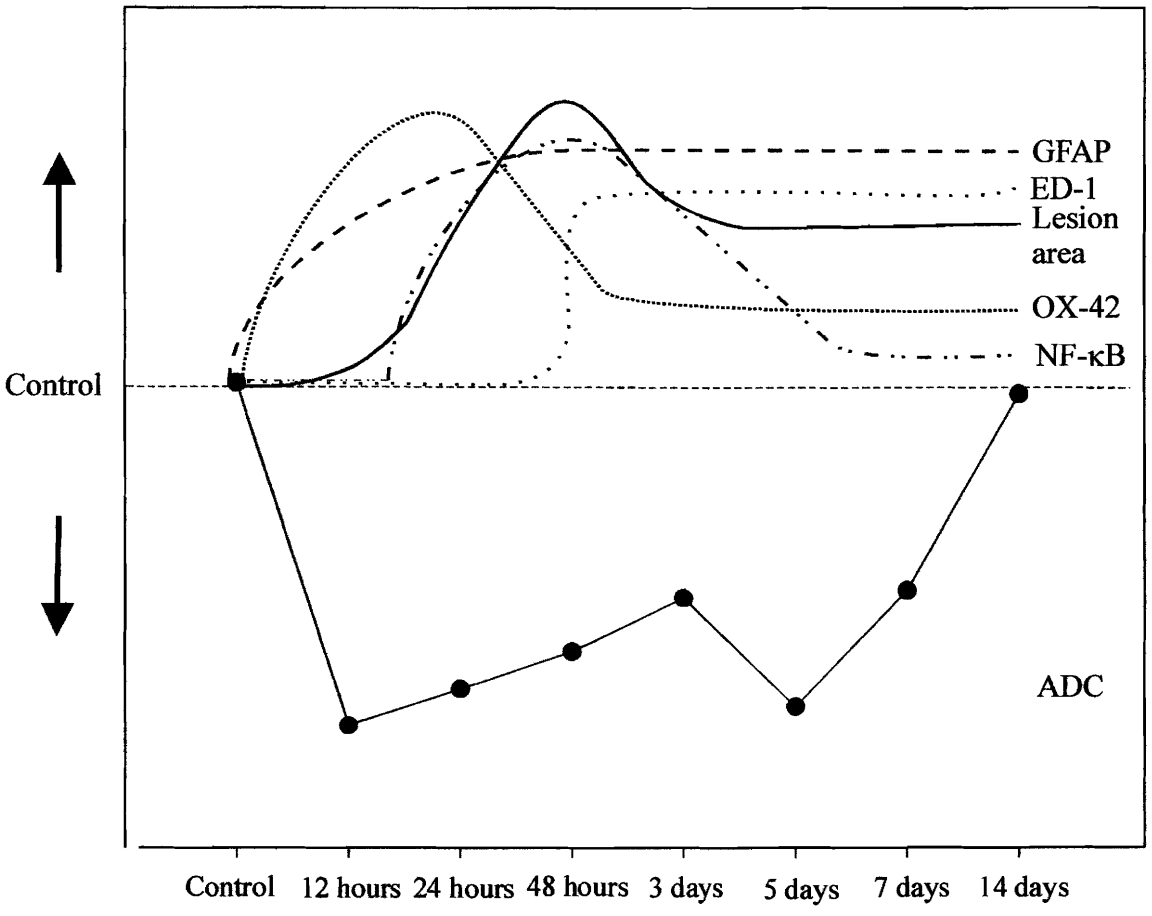

Figure 44: Comparison of the temporal profile of ADC change, lesion area and the onset of glial activation and post-injury inflammation after a cortical devascularization injury. The lower half of the diagram demonstrates the decrease in ADC which is followed by a slow progressive recovery towards control levels. The upper half illustrates the time course of early microglial activation (OX-42) within the entire ipsilateral hemisphere at 24 hours which then decreases and is limited to the peri-infarct region. Astrocyte activation (GFAP) is slower and reaches its maximum at 48 hours. This remained high throughout the length of the experiment. NF-κB immunoreactivity was low until 48 hours, after which time it rapidly increased in phagocytic cells within and surrounding the infarct. ED-1 immunoreactivity was not detected until 48 hours, at which time it was elevated in both phagocytic cells and activated microglia within the infarct and peri-infarct regions. The lesion area is at its maximum at 48 hours which corresponded to time points with increased ED-1 and NF-κB immunoreactivity.

6.4 Role of Inflammation in Cortical Devascularization Induced Ischemia

Some debate exists in assigning the relative contribution of an inflammatory response to permanent ischemic injury. Most would agree that a post-injury inflammatory response contributes to the ischemic injury, as leukocytes and monocytes have been observed during periods of active cell death (Stevens et al., 2002). Moreover, the inflammatory response should include both the activation of resident microglia and the recruitment and trafficking of blood derived leukocytes as both phagocytic microglia and blood derived macrophages respond to injury by the phagocytosis of damaged tissue and the secretion of cytotoxic agents (Kato et al., 1996); (Stoll, Jander, 1999); (Kato, Walz, 2000).

ED-1 immunoreactivity of cells with both a round and an amoeboid cell body indicate that both phagocytic macrophages and microglia are associated with the active formation of a pan-necrotic infarct after cortical devascularization. This confirmed the involvement of an inflammatory response and demonstrated that both the CNS and the immune system are involved.

The first appearance of blood-derived macrophages coincided with the onset of extensive necrosis, vacuolation and edema. Thus, in the 48 hours preceding this observation, there should be an increase in pro-inflammatory cytokine secretion that would allow the movement of these cells into the CNS. Both immunocytochemical and ELISA studies were performed to confirm and quantify pro-inflammatory cytokine secretion as well as uncovering the cellular source of their release. TNF-α was studied as its role as a mediator of inflammation after a permanent focal ischemic injury has

been well characterized (Becker, 1998); (Feuerstein et al., 1998); (del Zoppo et al., 2000). IFN-γ was studied as a small number of reports demonstrate its involvement in permanent focal ischemia (Pantoni et al., 1998); (Li et al., 2001) and *in vivo* hypoxia-ischemia (Lau, Yu, 2001). This molecule is generally associated with the activation of macrophages as well as regulating the antigen presenting cell function of macrophages, microglia and astrocytes (Roitt, 1998). In addition IFN-γ has been shown to induce the expression of other cytokines as well as stimulating the production of interferon regulatory factor-1, a molecule that induces NO synthase mRNA expression (Pantoni et al., 1998). The results of our immunocytochemistry experiments revealed small areas of TNF-α and IFN-γ immunoreactivity that co-localized to ED-1 immunoreactive cells within the developing infarct at 24 and 48 hours. However, only a small portion of the ED-1 positive cells that featured a rounded cell body were TNF-α or IFN-γ positive (Figure 28, 29). At 3 and 7 days the number of TNF-α positive cells had decreased and there were no IFN-γ positive cells (Figure 30). The lack of staining prior to infarct formation suggests that these two cytokines are not involved in the trafficking of inflammatory cells to the area of damage but instead may be involved in the cytotoxic activity of the phagocytes. In addition, the absence of TNF-α and IFN-γ immunoreactivity in activated astrocytes and microglia suggest that these cell types do not participate in the post-injury inflammatory response.

Quantification of TNF-α and IFN-γ levels associated with the development of the infarct was performed using a sandwich ELISA technique. This technique has been used previously to quantitate changes in interleukin levels in the rat brain following both focal ischemia (Legos et al., 2000) and neurotrauma (Fassbender et al., 2000). However, in

our studies we found large variations in the levels of both these cytokines perhaps due to the small lesion and sample size. As a result, we were unable to clearly identify a pattern of activity that corresponded to the histological evidence of inflammation during infarct formation. The small number of TNF-α and IFN-γ immunoreactive cells identified in our immunocytochemistry studies and the difficulty in obtaining a sample that contained only tissue associated with the lesion contributed to the loss of sensitivity in detecting either molecule using this technique.

6.5 DWI Changes after Neuroprotective Treatment

As previously discussed, DWI is a very useful tool to identify pathophysiological changes associated with a cortical devascularization injury. Moreover, DWI has been used to monitor the efficacy of numerous neuroprotective treatments for ischemia (Minematsu et al., 1993); (Lo et al., 1994); (Yenari et al., 1996); (Tatlisumak et al., 1998); (Chandra et al., 1999); (De Ryck et al., 2000); (Tatlisumak et al., 2000). To our knowledge, we are the first to examine the neuroprotective ability of the calcium buffer APTRA-AM, using DWI.

In our studies, treating injured animals with APTRA-AM resulted in a decrease in the area of hyper-intensity within the lesion area. A decrease in ADC was observed only within the first 12 hours after injury, unlike the saline injected animals, where there was a reduction in ADC throughout the first 3 days. While the mechanism responsible for blocking these ADC changes is unknown, it is likely that this observation could reflect the inhibition of cell death and post-injury inflammation associated with the calcium buffering capabilities of APTRA-AM treatment. Another possibility is that the

inhibition of synaptic transmission by APTRA-AM (Spigelman et al., 1998) reduced the occurrence of ischemia-induced depolarizations. In turn, this would result in a decrease in ADC as a result of inhibiting the depolarization-associated ion shifts that accompany intracellular water accumulation.

Injecting injured animals with DMSO also resulted in alterations to the temporal profile of ADC changes in these animals, compared to the saline injected animals. Specifically, DMSO reduced the degree of ADC change; such that the ADC changes observed over time were not significantly different than the ADC values obtained before injury. This is observation is very interesting as DMSO is widely used in research as a solvent for pharmacological agents. A review of the literature uncovered a number of studies that demonstrate that DMSO is neuroprotective (Shimizu et al., 1997); (Phillis et al., 1998); (Greiner et al., 200); (Lu, Mattson, 2001). These studies suggest that this molecule is neuroprotective based on it's numerous biological effects including anti-inflammatory and antioxidant properties. However, a more recent study by Lu and Mattson (2001) has shown that DMSO can prevent excitotoxic death by reducing the calcium influx induced by glutamate or NMDA and AMPA receptor activation. Perhaps in our experiments, DMSO was also able to inhibit the ADC changes in a manner similar to APTRA-AM, specifically the inhibition of the excitotoxic cascade thereby removing one of the factors causing cytotoxic edema.

We employed a multiple b-value DWI sequence to monitor the neuroprotective effect of APTRA-AM. A sequence of this type was used to determine if the b-value used affected our ability to detect diffusion changes after an injury of this type. It is well known that the b-value used determines the sensitivity of the sequence to diffusional

motions. For example, at low b-values there is minimal sensitivity to diffusional motion and T2-weighted contrast will predominate, however at high b-values, the contrast is largely produced by the diffusional properties of the tissue (Beauchamp et al., 1998). Many investigators suggest that the bi-exponential pattern of diffusion observed at higher b-values reflects the individual contributions of the different diffusing populations (Assaf, Cohen, 1998); (Assaf, Cohen, 2000) and it has been suggested that there are two populations representing fast and slow diffusing populations. Some investigators suggest that these populations actually represent the intracellular and extracellular components of water (Assaf, Cohen, 2000). In our study, we employed three different b values (110, 350 and 738 s/mm^2) and subsequent comparisons between these b-values in each treatment group found no difference in the ADC values obtained. It is possible that we were unable to achieve a significant difference between the b-values due to the range of b-values we chose. Alternatively, the small size of the lesion, its global effects (contralateral and ipsilateral) and the slow temporal evolution of changes could have influenced the ability of our experiments to resolve these two populations independently using multiple b-values.

6.6 Reduced Infarct Volume after Treatment with APTRA-AM

It is well accepted that an excitotoxic cascade including an increase in intracellular calcium, plays an important role in mediating cell death after an ischemic event. We hypothesized that treating animals with the cell-permeant calcium buffer APTRA-AM would result in a reduction in the size of the infarct. In a study comparing the maximal area of the infarct in untreated, sham, saline, DMSO and APTRA-AM

treated animals, those animals given the intravenous injections of the calcium buffer APTRA-AM showed an 85% decrease in infarct volume. APTRA-AM has been previously shown to be neuroprotective but only when administered prior to exposing cultured neurons to anoxic/aglycemic conditions (Abdel-Hamid, Tymianski, 1997). Other cell-permeant calcium buffers (e.g. EGTA-AM; BAPTA-AM) have also been shown to be neuroprotective against *in vivo* ischemic injury; however, they were also given prior to the induction of permanent MCA occlusion (Tymianski et al., 1994). This is the first demonstration that cell-permeant calcium buffers, specifically APTRA-AM, offers significant neuroprotection against neuronal death when administered after the onset of ischemia.

The mechanisms associated with the neuroprotective ability of cell-permeant calcium buffers have been suggested to involve an overall increase in a cell's calcium buffering capacity (Tymianski et al., 1993), as well as their ability to pre-synaptically inhibit the release of neurotransmitters (Tymianski et al., 1994); (Tymianski, 1995); (Spigelman et al., 1996). While our experiments did not address the mechanism by which APTRA-AM protects neurons after cortical devascularization, it seems likely that either one or both of the aforementioned mechanisms played a significant role. In our experiments, choosing a double dose strategy extended the calcium buffering capabilities and inhibition of synaptic transmission, effectively increasing the neuroprotective capabilities of this buffer.

More recently, BAPTA-AM was shown to protect cells from apoptotic cell death resulting from peroxynitrite exposure via the inhibition of caspase 3 (Virag et al., 1999). This result is very intriguing in light of the fact that our model features delayed cell

death, which may be indicative of apoptotic cell death. If apoptosis does play a role in infarct development, then perhaps APTRA-AM acts in a similar way to prevent the induction of the apoptotic program and ultimately protects the ischemic tissue from cell death.

Interestingly, when DMSO was given as the vehicle control in these neuroprotection experiments, a 52% decrease in infarct volume was observed when compared to the untreated animals. While this decrease was not statistically significantly, our data adds to the collection of previous studies which have reported that intravenous administration of DMSO can reduce the amount of cell death observed in both transient (Phillis et al., 1998) and permanent MCAO (Shimizu et al., 1997). While the exact mechanism of neuroprotection is unclear, one possibility is that DMSO, a known hydroxyl radical scavenger (Coles et al., 1986), reduces the amount of oxidative stress on neurons within the infarct and adjacent regions. DMSO has also been shown to suppress the Ca^{2+} influx associated with glutamate and NMDA receptor activation, thereby preventing excitotoxic cell death in hippocampal neurons (Lu, Mattson, 2001). Thus, any of these mechanisms likely plays a role in the neuroprotection seen after cortical devascularization. It is important to note that there was a significant reduction in infarct volume when the APTRA-AM group was compared to the DMSO treatment group. This confirms that the neuroprotective ability of APTRA-AM is due to its ability to reduce the intracellular calcium load independent of DMSO.

6.7 Changes in Glial Cell Activation and the Post-Injury Inflammatory Response after Treatment with APTRA-AM

The role of glial cell activation and post-injury inflammation in ischemic injury has previously been discussed (see section 6.3). In this model, both the microglia and astrocytes are activated prior to infarct formation. After 48 hours, the microglia became phagocytic and were found associated within and surrounding the infarct, as were numerous macrophages. Similarly, reactive astrocytes were observed in the peri-infarct areas forming a glial scar. By 7 days, both cell types remained in association with the infarct and had retained their reactive morphologies.

Administering APTRA-AM after cortical devascularization reduced the microglial response to the outer molecular layer immediately inferior to the surgery site while completely inhibiting the phagocytic response when compared to un-treated animals 7 days after injury. One possible explanation is that the buffering of intracellular calcium by APTRA-AM reduced the expression of ionized calcium-binding adapter molecule 1 (Iba1), a molecule involved in calcium signaling pathways responsible for cell mobility and phagocytosis (Ito et al., 2001). In our experiments, NF-κB immunoreactivity remained predominately cytoplasmic, suggesting that the translocation of this transcription factor is blocked by APTRA-AM. This observation supports previous observations where it was noted that both EGTA-AM and BAPTA-AM suppress the activation of NF-κB in cultured Wurzburg and fibroblast cell cultures (Sen et al., 1996) (Shahrestanifar et al., 1999).

APTRA-AM did not inhibit the activation of astrocytes, as highly reactive cells could be found throughout both hemispheres. This observation was in contrast to an

earlier report which demonstrated that the calcium buffer BAPTA-AM reduced GFAP immunoreactivity in astrocyte cultures (Lee et al., 2000).

Despite its reported role as a free radical scavenger, DMSO treatment did not reduce or eliminate NF-κB activation, which is thought to occur in the presence of reactive oxygen species (Flohe et al., 1997). This may be due to the fact that NF-κB activation is most often associated with an increase in H_2O_2, rather than hydroxyl radicals (Christman et al., 2000).

6.8 Concluding Comments

The experiments reported here include a MRI and histological characterization of a novel model of permanent focal cerebral ischemia. In addition, we have used this model to study the effectiveness of the cell permeant calcium buffer, APTRA-AM, as a neuroprotective agent when administered after injury.

In these experiments, it was clearly established that DWI is a sensitive measure of the evolving injury that results from a cortical devascularization injury. When we compare the results of our histology and immunocytochemistry studies to the DWI study, we are confident that the early changes in DWI are the result of changes in the astrocyte and microglial cell populations. After 48 hours, the onset of inflammation and concomitant formation of a pan-necrotic infarct are responsible for the slow return of the ADC values to normal. While the time course differs slightly, these observations are similar to what has been previously observed in other models of ischemia (Pierpaoli et al., 1993); (Gill et al., 1995); {Schroeter, Franke, et al. 2001 ID: 470}. Thus confirming that cortical devascularization is a viable, yet under utilized model of permanent focal

ischemia. Moreover, this work contributes to the body of evidence which points to the reliability of DWI as an early indicator of ischemic pathology.

Once we had completely characterized the model and clearly established the ability of DWI to detect the pathophysiological changes associated with the injury, a second set of experimental objectives were designed to examine the effectiveness of APTRA-AM in preventing ischemic cell death. The histological studies clearly show that APTRA-AM is highly effective when given after an injury, as we observed a significant reduction in infarct area and the accompanying inflammatory response. In addition, we were unable to detect any significant changes in tissue diffusion after APTRA-AM treatment, which validates our approach of using DWI as a method of testing the efficacy of neuroprotective compounds.

Much to our surprise, we also found that DMSO (1%) reduces the infarct volume as well as inhibiting the changes in tissue diffusion that typically accompany a cortical devascularization injury. This finding is significant as DMSO is commonly used as a solvent in pharmacology studies, and our results indicate that its use could potentially complicate the final outcome due to its neuroprotective abilities. However, the lesion area of the APTRA-AM treated animals was significantly different than the DMSO treatment group. Thus we were confident that the neuroprotective effect of APTRA-AM was a result of its pharmacological effects and not compounded by the effect of DMSO. To our knowledge, this is the first study to provide evidence that cell permeant calcium buffers are capable of neuroprotection when given after ischemic injury.

While further research is necessary to clearly define the mechanism by which APTRA-AM acts as a neuroprotectant, this study contributes significantly to the body of

evidence that supports the use of cell-permeant calcium buffers as a neuroprotective therapy in cerebral ischemia.

7.0 Appendices

7.1 Animal Groups

The following tables contain a list of the animals used in each experiment. See Tables 1, 2, 3, 4, 5, and 6 for the number of animals used in each time point.

Table 8: The number of animals used in the experiments to characterize the cortical devascularization model.

Aim	Experiment	Total	Animal Groupings		
Characterization of the cortical devascularization model of ischemia					
			Control	**Sham**	**Ischemia**
	DW and T2W imaging study	37	3	10	24
	GdT1W imaging study	7	0	3	4
	Cresyl violet histochemistry	65	32	27	32
	Lesion volume measurements	22[a]	0	0	22
	Immunohistochemistry	32[b]	3	11	18
	Fluoro-Jade staining	32[b]	3	11	18
Determination of the extent of the inflammatory response					
	Fluorescent immunohistochemistry	32[b]	3	11	18
	Fluoro-Jade staining	32[b]	3	11	18
	ELISA	42	6	18	18

[a] these animals are in addition to the 32 ischemic animals used from the cresyl violet study.

[b] denotes animals that were culled from the same population of animals used in the cresyl violet histology experiment in the characterization study.

Table 9: The number of animals used in the neuroprotection experiments.

Aim	Experiment	Total	Animal Groupings				
APTRA-AM Neuroprotection Study							
			Un-treated	Sham	Saline	DMSO	APTRA-AM
	DW imaging study	23	0	0	8	7	8
	Cresyl violet histology	37	0	0	8	11	9
	Lesion volume measurements	37[a]	4	5	8	11	9
	Immuno-histochemistry	11[b]	0	0	4	3	4
	Fluoro-Jade staining	11[b]	0	0	4	3	4

[a] an additional 11 animals from the original cresyl violet histology study and sham cresyl violet histology were added to the untreated and sham groups to increase their sample size.

[b] denotes animals that were culled from the same population of animals used in the cresyl violet histology experiment in the neuroprotection study.

7.2 Histochemistry: Buffers, Fixatives, and Stains

7.2.1 Buffers

7.2.1.1 Phosphate Buffered Saline

Phosphate buffered saline (PBS) was routinely used as the buffer in all the histochemistry and immunocytochemical procedures. A stock (10X) solution was prepared by dissolving 76.5 g NaCl (Fisher Scientific, Tustin, CA; S271-3), 7.25 g Na_2HPO_4 (Sigma-Aldrich, St. Louis, MO; S2713) and 1.72 g KH_2PO_4 (Fisher Scientific, Tustin, CA; BP362-1) in 700 ml triple distilled water. The volume was brought to 1 L

by adding additional triple distilled water. The PBS was stored at room temperature and diluted as needed.

7.2.1.2 Millonig's Buffer (0.12 mM)

Millonig's buffer was used as the primary buffer for the fixation and preparation of the brains for sectioning. This buffer was prepared by adding 16.88 g NaH_2PO_4 and 3.86 g NaOH (Sigma-Aldrich, St. Louis, MO; S8045) to 1 L of triple distilled water. The solution was adjusted to pH to 7.3, filtered and stored at 4°C.

7.2.1.3 Phosphate Buffer (0.5 M)

This solution was used in the preparation of the cryoprotectant solution used in the storage of cryostat sections. A 100 ml volume was prepared by adding 28 ml of 1 M NaH_2PO_4 (Fisher Scientific, Tustin, CA; S397500) to 72 ml $Na_2HPO_4.7H_20$ (Fisher Scientific, Tustin, CA; S471-3).

7.2.2 Fixatives and Storage Solutions

7.2.2.1 Formaldehyde (4%)

Formaldehyde was used in the perfusion fixation of animals selected for histological analysis and was prepared by adding 40 g paraformaldehyde (Fisher Scientific, Tustin, CA; 04042-500) to 400 ml of 60°C triple distilled water. The solution was cleared by the addition of 2-5 drops of 10 N NaOH. The solution was brought up to 1 L by adding 500 ml of 0.12 mM Millonig's buffer, adjusted to pH 7.3 and filtered

through Whatman #1 filter paper. This solution was stored at 4°C and used within 1 week of preparation.

7.2.2.2 Sucrose (30%)

After the transcardially perfusion with 4% formaldehyde, the brains were removed and placed in a 30% sucrose solution until they sank. This solution was prepared by adding 30 g sucrose (Fisher Scientific, Tustin, CA; S5-500) to 100 ml of PBS.

7.2.2.3 Cryoprotectant Solution

Cryostat sections that were not immediately stained with cresyl violet, including those used for immunocytochemistry and Fluoro-Jade staining were stored in a cryoprotectant solution. This solution was prepared by adding 100 ml glycerol (Fisher Scientific, Tustin, CA; AC410985006) and 120 ml ethylene glycol (Fisher Scientific, Tustin, CA; AC146750010) to 0.5 M phosphate buffer.

7.2.3 Stains

7.2.3.1 Cresyl Violet Acetate (1%)

Cresyl violet is a stain used to visualize Nissl substance in neurons and can be used to differentiate healthy from un-healthy cells. Five hundred milligrams of cresyl violet acetate (Sigma-Aldrich, St. Louis, MO; C5042) was added to 500 ml of distilled water. While stirring, 0.125 g of sodium acetate (Fisher Scientific, Tustin, CA;

BP333500) and 1.5 ml of glacial acetic acid (Fisher Scientific, Tustin, CA; A38212) were added followed by filtration. The stain was stored at room temperature in a glass bottle and re-filtered before use.

7.2.3.1.1 Chloroform - Ether Solution

This solution was used in the cresyl violet staining procedure to remove the lipids prior to re-hydration and emersion in the cresyl violet acetate. The solution was prepared by adding 800 ml of chloroform (Fisher Scientific, Tustin, CA; AC423550040) to 100 ml of ether (Fisher Scientific, Tustin, CA; AC615080010) and 100 ml of 95% alcohol (Fisher Scientific, Tustin, CA; HC-600-1GAL). This solution was stored at room temperature and used until it became cloudy.

7.2.3.1.2 Acetic – Formalin Solution

Emersion in an acetic – formalin solution for 1 –10 minutes was used to remove excess cresyl violet stain. This solution was prepared by adding 40 ml of 37 – 40% formaldehyde solution (Fisher Scientific, Tustin, CA; F75P-4) to 2 ml of glacial acetic acid and 960 ml of distilled water. The solution could be re-used until it was no longer clear.

7.2.3.2 Fluoro-Jade

Fluoro-Jade is an anionic fluorochrome used to selectively stain degenerating neurons in brain sections. A 0.01% stock solution is prepared by dissolving 10 mg Fluoro-Jade in 100 ml of distilled water and stored at room temperature in a dark bottle

for up to 3 months. The 0.001% working solution was prepared immediately before use by adding 10 ml of the stock solution to 90 ml of 0.1% acetic acid in triple distilled water.

8.0 References

Abdel-Hamid KM, Tymianski M (1997) Mechanisms and effects of intracellular calcium buffering on neuronal survival in organotypic hippocampal cultures exposed to anoxia/aglycemia or to excitoxins. J Neurosci 17:3538-3553.

Abe O, Okubo T, Hayashi N, Saito N, Iriguchi N, Shirouzu I, Kojima Y, Matsumoto K, Ohtomo K, Sasaki Y (2000) temporal changes of the apparent diffusion coefficients of water and metabolites in rats with hemispheric infarction: experimental study of transhemispheric diaschisis in the contralateral hemisphere at 7 tesla. J Cereb Blood Flow Metab 20:726-735.

Abraham H, Lazar G (2000) Early microglial reaction following mild forebrain ischemia induced by common carotid artery occlusion in rats. Brain Res 862:63-73.

Akopov SE, Simonian NA, Grigorian GS (1996) Dynamics of polymorphonuclear leukocyte accumulation in acute cerebral infarction and their correlation with brain tissue damage. Stroke 27:1739-1743.

Amedee T, Robert A, Coles JA (1997) Potassium homeostasis and glial energy metabolism. Glia 21:46-55.

Andrews RJ (1991) Transhemispheric diaschisis. A review and comment. Stroke 22:943-949.

Armitage PA, Bastin ME, Marshall I, Wardlaw JM, Cannon J (1998) Diffusion anisotropy measurements in ischaemic stroke of the human brain. MAGMA 6:28-36.

Arvin B, Neville LF, Barone FC, Feuerstein GZ (1996) The role of inflammation and cytokines in brain injury. Neurosci Biobehav Rev 20:445-452.

Assaf Y, Cohen Y (1998) Non-mon0-exponential attenuation of water and N-acetyl aspartate signals due to diffusion in brain tissue. J Magn Reson 131:69-85.

Assaf Y, Cohen Y (2000) Assignment of the water slow-diffusing component in the central nervous system using q-space diffusion MRS: implications for fiber tract tracing. Magn Reson Med 43:191-199.

Baeuerle PA, Henkel T (1994) Function and activation of NF-κB in the immune system. Annu Rev Immunol 12:141-179.

Banati RB, Gehrmann J, Schubert P, Kreutzberg GW (1993) Cytotoxicity of microglia. Glia 7:111-118.

Bartnik BL, Kendall EJ, Obenaus A (2001) Cortical devascularization: quantitative diffusion weighted magnetic resonance imaging and histological findings. Brain Res 915:133-142.

Bauer J, Sminia T, Wouterlood FG, Dijkstra CD (1994) Phagocytic activity of macrophages and microglial during the course of acute and chronic relapsing experimental autoimmune encephalomyelitis. J Neurosci Res 38:365-375.

Beauchamp NJ, Ulug AM, Passe TJ, van Zijl PCM (1998) MR diffusion imaging in stroke: reviews and controversies. Radiographics 18:1269-1283.

Becker KJ (1998) Inflammation and acute stroke. Curr Opin Neurol 11:45-49.

Benveniste H, Hedlund LW, Johnson GA (1992) Mechanism of detection of acute cerebral ischemia in rats by diffusion weighted magnetic resonance microscopy. Stroke 23:746-754.

Berezovskaya O, Maysinger D, Feeney DM (1996) Colony stimulating factor-1 potentiates neuronal survival in cerebral cortex ischemic lesion. Acta Neuropathol (Berl) 92:479-486.

Biernaskie J, Corbett D, Peeling J, Wells J, Lei H (2001) A Serial MR study of cerebral blood flow changes and lesion development following endothelin-1 induced ischemia in rats. Magn Reson Med 46:827-830.

Bishop GM, Robinson SR (2001) Quantitative analysis of cell death and ferritin expression in response to cortical iron: implications for hypoxia-ischemia and stroke. Brain Res 907:175-187.

Botchkina GI, Geimonen E, Bilof ML, Villarreal O, Tracey KJ (1999) Loss of NF-κB activity during cerebral ischemia and TNF cytotoxicity. Mol Med 5:372-381.

Braun JS, Jander S, Schroeter M, Witte OW, Stoll G (1996) Spatiotemporal relationship of apoptotic cell death to lymphomonocytic infiltration in photochemically induced focal ischemia of the rat cerebral cortex. Acta Neuropathol (Berl) 92:255-263.

Burdette JH, Elster AD, Ricci PE (1999) Acute cerebral infarction: quantification of spin-density and T2 shine-through phenomena on diffusion-weighted MR images. Radiology 212:333-339.

Busza AL, Allen KL, King MD, van Bruggen N, Williams SR, Gadian DG (1992) Diffusion-weighted imaging studies of cerebral ischemia in gerbils. Stroke 23:1602-1612.

Butler TL, Kassed CA, Sanberg PR, Willing AE, Pennypacker KR (2002) Neurodegeneration in the rat hippocampus and striatum after middle cerebral artery occlusion. Brain Res 929:252-260.

Calamante F, Lythgoe MF, Pell GS, Thomas DL, King MD, Busza AL, Sotak CH, Williams SR, Ordidge RJ, Gadian DG (1999) Early changes in water diffusion, perfusion, T1, and T2 during focal cerebral ischemia in the rat studied at 8.5 T. Magn Reson Med 41:479-485.

Callaghan PT (1995) The Measurement of Motion Using Spin Echoes. In: Principles of Nuclear Magnetic Resonance Imaging (Callaghan PT ed), pp 328-370. Oxford: Oxford University Press.

Carroll JE, Hess DC, Howard EF, Hill WD (2000) Is nuclear factor-κB a good treatment target in brain ischemia/reperfusion injury? Neuroreport 11:R1-R4

Chandra J, Samali A, Orrenius S (2000) Triggering and modulation of apoptosis by oxidative stress. Free Radic Bio Med 29:323-333.

Chandra S, White RF, Everding D, Feuerstein GZ, Coatney RW, SArkar SK, Barone FC (1999) Use of diffusion-weighted MRI and neurological deficit scores to demonstrate beneficial effects of isradipine in a rat model of focal ischemia. Pharmacology 58:292-299.

Chen J, Graham SH, Chan PH, Lan J, Zhou RL, Simon RP (1995) bcl-2 is expressed in neurons that survive focal ischemia in the rat. Neuroreport 6:394-398.

Choi DW (1988) Calcium-mediated neurotoxicity: relationship to specific channel types and role in ischemic damage. Trends Neurosci 11:465-469.

Choi DW (1992) Excitotoxic cell death. J Neurobio 23:1261-1276.

Choi DW (1996) Ischemia-induced neuronal apoptosis. Curr Opin Neurol 6:667-672.

Christman JW, Blackwell TS, Juurlink BHJ (2000) Redox regulation of nuclear factor kappa B: therapeutic potential for attenuating inflammatory responses. Brain Pathol 10:153-162.

Clark RK, Lee EV, Fish CJ, White RFPWJ, Jonak ZL, Feuerstein GZ, Barone FC (1993) Development of tissue damage, inflammation and resolution following stroke: an immunohistochemical and quantitative planimetric study. Brain Res Bull 31:565-572.

Clark WM, Rinker LG, Lessov NS, Hazel K, Eckenstein F (1999) Time course of IL-6 expression in experimental CNS ischemia. Neurol Res 21:287-292.

Clemens JA (2000) Cerebral ischemia: gene activation, neuronal injury, and the protective role of antioxidants. Free Radic Bio Med 28:1526-1531.

Clemens JA, Stephenson DT, Dixon EP, Smalstig EB, Mincy RE, Rash KS, Little SP (1997) Global cerebral ischemia activates nuclear factor-κB prior to evidence of DNA fragmentation. Mol Brain Res 48:187-196.

Coles JC, Ahmed SN, Mehta HU, Kaufmann JCE (1986) Role of free radical scavenger in protection of spinal cord during ischemia. Ann Thorac Surg 41:551-556.

Conner JM, Hoener MC, Varon S (1998) Partial cortical devascularization results in elevations of cortical nerve growth factor and increases nerve growth factor protein within basal forebrain cholinergic neurons. Neuroscience 83:1003-1011.

D'Arceuil HE, de Crespigny AJ, Rother J, Moseley M, Rhine W (1999) Serial magnetic resonance diffusion and hemodynamic imaging in a neonatal rabbit model of hypoxic-ischemic encephalopathy. NMR Biomed 12:505-514.

Damoiseaux JG, Dopp EA, Calame W, Chao D, MacPherson GG, Dijkstra CD (1994) Rat macrophage lysosomal membrane antigen recognized by monoclonal antibody ED1. Immunology 83:140-147.

Davies CA, Loddick SA, Stroemer RP, Hunt J, Rothwell NJ (1998) An integrated analysis of the progression of cell responses introduced by permanent focal middle cerebral artery occlusion in the rat. Exp Neurol 154:199-212.

Davis JN, Antonawich FJ (1997) Role of apoptotic proteins in ischemic hippocampal damage. Ann N Y Acad Sci 835:309-320.

De Ryck M, Verhoye M, van der Linden A-M (2000) Diffusion-weighted MRI of infarct growth in a rat photochemical stroke model: effect of lubeluzole. Neuropharmacology 39:691-702.

del Zoppo GJ, Ginis I, Hallenbeck JM, Iadecola C, Wang X, Feuerstein GZ (2000) Inflammation and stroke: putative role for cytokines, adhesion molecules, and iNOS in brain response to ischemia. Brain Pathol 10:95-112.

Dijkstra CD, Dopp EA, Joling P, Kraal G (1985) The heterogeneity of mononuclear phagocytes in lymphoid organs: distinct macrophage subpopulations in the rat recognized by monoclonal antibodies ED1, ED2 and ED3. Immunology 54:589-599.

Dirnagl U, Iadecola C, Moskowitz MA (1999) Pathobiology of ischaemic stroke: an integrated view. Trends Neurosci 22:391-397.

Dixon EP, Stephenson DT, Clemens JA, Little SP (1997) Bcl-X short is elevated following severe global ischemia in rat brains. Brain Res 776:222-229.

Ebisu T, Tanaka C, Umeda M, Kitamura M, Fukunaga M, Aoki I, Sato H, Higuchi T, Naruse S, Horikawa Y, Ueda S (1997) Hemorrhagic and nonhemorrhagic stroke: diagnosis with diffusion-weighted and T2-weighted echo planar MR imaging. Radiology 203:823-828.

Eddleston M, Mucke L (1993) Molecular profile of reactive astrocytes - implications for their role in neurologic disease. Neuroscience 54:15-36.

Fassbender K, Schneider S, Bertsch T, Schlueter D, Fatar M, Ragoschke A, Kuhl S, Kischka U, Hennerici M (2000) Temporal profile of release of interleukin-1beta in neurotrauma. Neurosci Lett 284:135-138.

Feeney DM, Baron J-C (1986) Diaschisis. Stroke 17:817-830.

Feuerstein GZ, Wang X, Barone FC (1997) Inflammatory gene expression in cerebral ischemia and trauma. Ann N Y Acad Sci 825:179-193.

Feuerstein GZ, Wang X, Barone FC (1998) Cytokines in brain ischemia - the role of TNF-α. Cell Mol Neurobiol 18:695-701.

Flohe L, Brigelius-Flohe R, Saliou C, Traber MG, Packer L (1997) Redox regulation of NF-kappa B activation. Free Radic Bio Med 22:1115-1126.

Gabriel C, Justicia C, Camins A, Planas AM (1999) Activation of nuclear factor-κB in the rat brain after transient focal ischemia. Mol Brain Res 65:61-69.

Garcia JH, Liu K-F, Yoshida Y, Lian J, Chen S, del Zoppo GJ (1994) Influx of leukocytes and platelets in an evolving brain infarct (wistar rat). Am J Pathol 144:188-199.

Germano IM, Pitts LH, Berry I, Moseley M (1989) Magnetic resonance imaging and P31 magnetic resonance spectroscopy for evaluating focal cerebral ischemia. J Neurosurg 70:612-618.

Ghirnikar RS, Lee YL, Eng LF (1998) Inflammation in traumatic brain injury: role of cytokines and chemokines. Neurochem Res 23:329-340.

Ghosh S, May MJ, Kopp EB (1998) NF-κB and REL proteins: evolutionary conserved mediators of immune responses. Ann Rev Immunol 16:255-260.

Gill R, Sibson NR, Hatfield RH, Burdett NG, Carpenter TA, Hall LD, Pickard JD (1995) A comparison of the early development of ischemic damage following permanent middle cerebral artery occlusion in rats as assessed using magnetic resonance imaging and histology. J Cereb Blood Flow Metab 15:1-11.

Gluckman P, Klempt N, Guan J, Mallard C, Sirimanne E, Dragunow M, Klempt M, Singh K, Williams C, Nikolics K (1992) A role for IGF-1 in the rescue of CNS neurons following hypoxia-ischemic injury. Biochem Biophys Res Comm 182:593-599.

Gonzalez-Scaano F, Baltuch G (1999) Microglia as mediators of inflammatory and degenerative diseases. Ann Rev Neurosci 22:219-240.

Gourmala NG, Limonta S, Bochelen D, Sauter A, Boddeke HWGM (1999) Localization of macrophage inflammatory protein: macrophage inflammatory protein-1

expression in rat brain after peripheral administration of lipopolysaccharide and focal cerebral ischemia. Neuroscience 88:1255-1266.

Graeber MB, Streit WJ (1990) Perivascular microglia defined. Trends Neurosci 13:366

Gregersen R, Lambertsen K, Finsen B (2000) Microglia and macrophages are the major source of tumor necrosis factor in permanent middle cerebral artery occlusion in mice. J Cereb Blood Flow Metab 20:53-65.

Greiner C, Schmidinger A, Hulsmann S, Moskopp D, Wolfer J, Kohling R, Speckmann E-J, Wassmann H (200) Acute protective effect of nimodipine and dimethyl sulfoxide against hypoxic and ischemic damage in brain slices. Brain Res 887:316-322.

Guerrini L, Blasi F, Denis-Donini S (1995) Synaptic activation of NF-κB by glutamate in cerebellar granule neurons in vitro. Proc Natl Acad Sci USA 92:9077-9081.

Hallenbeck JM (1996) Significance of the inflammatory response in brain ischemia. Acta Neurochir Suppl 66:27-31.

Harris NG, Zilkha E, Houseman J, Symms MR, Obrenovitch TP, Williams.S.R. (2000) The relationship between the apparent diffusion coefficient measured by magnetic resonance imaging, anoxic depolarization, and glutamate efflux during experimental cerebral ischemia. J Cereb Blood Flow Metab 20:28-36.

Harris RJ, Symon L (1984) Extracellular pH, potassium, and calcium actvities in progressive ischaemia of rat cortex. J Cereb Blood Flow Metab 4:178-186.

Harris RJ, Symon L, Branston NM, Bayhan M (1981) Changes in extracellular calcium activity in cerebral ischaemia. J Cereb Blood Flow Metab 1:203-209.

Hashemi RH, Bradley WG (1997) MRI, the basics. Baltimore: Williams and Wilkins.

Hazlewood CF (1995) Diffusion in Biological Tissues. In: Diffusion and Perfusion Magnetic Resonance Imaging. Applications to Functional MRI (Le Bihan D Ed), pp 123-126. New York: Raven Press.

Helperen JA, Ordidge RJ, Knight RA, Jiang Q (1995) Brain Ischemia. Mechanisms and Predictive Value of the Decrease in Water Diffusion in Cerebral Ischemia. In: Diffusion and Perfusion Magnetic Resonance Imaging. Applications to Functional MRI. (Le Bihan D Ed), pp 173-179. New York: Raven Press.

Hensley K, Robinson KA, Gabbita SP, Salsman S, Floyd RA (2000) Reactive oxygen species, cell signaling, and cell injury. Free Radic Bio Med 28:1456-1462.

Herrera DG, Cuello AC (1992) Glial fibrillary acidic protein immunoreactivity following cortical devascularizing lesion. Neuroscience 49:781-791.

Hoehn M, Nicolay K, Franke C, van der Sanden B (2001) Application of magnetic resonance to animal models of cerebral ischemia. J Magn Reson Imaging 14:491-509.

Hossman K-A (1998) Experimental models for the investigation of brain ischemia. Cardiovasc Res 39:106-120.

Iadecola C (1997) Bright and dark sides of nitric oxide in ischemic brain injury. Trends Neurosci 20:132-139.

Iadecola C, Alexander M (2001) Cerebral ischemia and inflammation. Curr Opin Neurol 14:89-94.

Iadecola C, Ross ME (1997) Molecular pathology of cerebral ischemia: delayed gene expression and strategies for neuroprotection. Ann N Y Acad Sci 835:203-217.

Iadecola C, Zhang F, Casey R, Clark HB, Ross ME (1996) Inducible nitric oxide synthase gene expression in vascular cells after transient focal cerebral ischemia. Stroke 27:1373-1380.

Iadecola C, Zhang F, Casey R, Ross ME (1995) Inducible nitric oxide synthase gene expression in brain following cerebral ischemia. J Cereb Blood Flow Metab 15:378-384.

Isemann S, Stoll G, Schroeter M, Krajewski S, Reed JC, Bahr M (1998) Differential regulation of Bax, Bcl-2, and Bcl-X proteins in focal cortical ischemia in the rat. Brain Pathology 8:49-62.

Ito D, Tanaka K, Suzuki S, Dembo T, Fukuuchi Y (2001) Enhanced expression of Iba1, ionized calcium-binding adapter molecule 1, after transient focal cerebral ischemic in rat brain. Stroke 32:1208-1215.

Jander S, Pohl J, Gillen C, Schroeter M, Stoll G (1996) Vascular cell adhesion molecule-1 mRNA is expressed in immune-mediated and ischemic injury of the rat nervous system. J Neuroimmunol 70:75-80.

Jiang N, Chopp M, Chahwala S (1998) Neutrophil inhibitory factor treatment of focal cerebral ischemia in the rat. Brain Res 788:25-34.

Kandel ER, Schwartz JH (1991) Directly gated transmission at central synapses. In: Principles of Neural Science (Kandel ER, Schwartz JH, Jessell TM eds), pp 153-172. New York: Elsevier.

Kastrup A, Engelhorn T, Beaulieu C, de Crespigny A, Moseley ME (1999) Dynamics of cerebral injury, perfusion, and blood-brain barrier changes after temporary and permanent middle cerebral artery occlusion in the rat. J Neurol Sci 166:91-99.

Kato H, Kogure K, Liu X-H, Araki T, Itoyama Y (1996) Progressive expression of immunomolecules on activated microglia and invading leukocytes following focal cerebral ischemia in rats. Brain Res 734:203-212.

Kato H, Walz W (2000) The initiation of the microglial response. Brain Pathol 10:137-143.

Kettunen MI, Grohn OHJ, Lukkarinen JA, Vainio P, Silvennoinen MJ, Kauppinen RA (2000) Interrelations of T1 and diffusion of water in acute cerebral ischemia of the rat. Magn Reson Med 44:833-839.

Kim H-Y, Vaughan DK, Ghosh S (1998) Pathways of cerebral calcium accumulation in a model of focal ischemia in rats. Neurol Res 20:169-177.

Knight RA, Dereski MO, Helperen JA, Ordidge RJ, Chopp M (1994) Magnetic resonance imaging assessment of evolving focal cerebral ischemia. Stroke 25:1252-1262.

Kochanek PM, Hallenbeck JM (1992) Polymorphonuclear leukocytes and monocytes/macrophages in the pathogenesis of cerebral ischemia and stroke. Stroke 23:1367-1379.

Kohno K, Hoehn-Berlage M, Mies G, Back T, Hossman K-A (1995) Relationship between diffusion-weighted MR images, cerebral blood flow, and energy state in experimental brain infarction. Magn Reson Imaging 13:73-80.

Kotila M, Waltimo O (1992) Epilepsy after stroke. Epilepsia 33:495-498.

Kristian T, Siesjo BK (1998) Calcium in ischemic cell death. Stroke 29:705-718.

Kubes P, Ward PA (2000) Leukocyte recruitment and the acute inflammatory response. Brain Pathol 10:127-135.

Kuchel PW, Coy A, Stilbs P (1997) NMR "diffusion-diffraction" of water revealing alignment of erythrocytes in a magnetic field and their dimensions and membrane transport characteristics. Magn Reson Med 37:637-643.

Larsson E, Lindvall O, Kokaia Z (2001) Sterelogical assessment of vulnerability of immunocytochemically identified striatal and hippocampal neurons after global cerebral ischemia in rats. Brain Res 913:117-132.

Lau LT, Yu ACH (2001) Astrocytes produce and release interleukin-1, interleukin-6, tumor necrosis factor alpha and interferon-gamma following traumatic and metabolic injury. J Neurotrauma 18:351-359.

Lawson LJ, Perry VH, Dri P, Gordon S (1990) Heterogeneity in the distribution and morphology of microglia in the normal adult mouse brain. Neuroscience 29:151-170.

Le Bihan D (1995) Diffusion Imaging: Diffusion NMR Imaging with Spin Echoes. In: Diffusion and Perfusion Magnetic Resonance Imaging: Applications to Functional MRI (Le Bihan D ed), pp 19-28. New York: Raven Press.

Le Bihan D, Basser PL (1995) Principles of Diffusion MRI and Spectroscopy. In: Diffusion and Perfusion Magnetic Resonance Imaging. Applications to Functional MRI. (Le Bihan D Ed), pp 5-17. New York: Raven Press.

Le Bihan D, Breton E, Lallemand D, Grenier P, Cabanis E, Laval-Jeantet M (1986) MR imaging of intravoxel incoherent motions: application to diffusion and perfusion in neurologic disorders. Radiology 161:401-407.

Lee YB, Du S, Rhim HW, Lee EB, Markelonis GJ, Oh TH (2000) Rapid increase in immunoreactivity to GFAP in astrocytes in vitro induced by acidic pH is mediated by calcium influx and calpain I. Brain Res 864:220-229.

Legos JJ, Whitmore RG, Erhardt JA, Parsons AA, Tuma RF, Barone FC (2000) Quantitative changes in interleukin proteins following focal stroke in the rat. Neurosci Lett 282:189-192.

Li F, Liu K-F, Silva MD, Omae T, Sotak CH, Fenstermacher JD, Fisher M (2000) Transient and permanent resolution of ischemic lesions on diffusion-weighted imaging after brief periods of focal ischemia in rats. Stroke 31:946-954.

Li F, Liu K-F, Silva MD, Omae T, Sotak CH, Fenstermacher JD, Fisher M (2000) Transient and permanent resolution of ischemic lesions on diffusion weighted imaging after brief periods of focal ischemia in rats. Correlation with histopathology. Stroke 31:946-954.

Li H-L, Kostulas N, Huang Y-M, Xiao B-G, van der Meide P, Kostulas V, Giedraitas V, Link H (2001) IL-17 and IFN-γ mRNA expression is increased in the brain and systemically after permanent middle cerebral artery occlusion in the rat. J Neuroimmunol 116:5-14.

Li Y, Sharov VG, Jiang N, Zaloga C, Sabbah HN, Chopp M (1995) Ultrastructural and light microscopic evidence of apoptosis after middle cerebral artery occlusion in the rat. Am J Pathol 146:1045-1051.

Lin W, Paczynski RP, Venkatesan R, He YY, Powers WJ, Hsu CY, Haacke EM (1997) Quantitative regional brain water measurement with magnetic resonance imaging in a focal ischemia model. Magn Reson Med 38:303-310.

Lipton P (1999) Ischemic cell death in brain neurons. Physiol Rev 79:1431-1568.

Liu D, Smith CL, Barone FC, Ellison JA, Lysko PG, Li K, Simpson IA (1999) Astrocytic demise precedes delayed neuronal death in focal ischemic rat brain. Mol Brain Res 68:29-41.

Liu T, Clark RK, McDonnell PC, Young PR, White RF, Barone FC, Feuerstein GZ (1994) Tumor necrosis factor-α expression in ischemic neurons. Stroke 25:1481-1488.

Lo EH, Matsumoto K, Pierce AR, Garrido L, Luttinger D (1994) Pharmacological reversal of acute changes in diffusion-weighted magnetic resonance imaging in focal cerebral ischemia. J Cereb Blood Flow Metab 14:597-603.

Longa EZ, Weinstein PR, Carlson SCR (1989) Reversible middle cerebral artery occlusion without craniectomy in rats. Stroke 20:84-91.

Lu C, Mattson MP (2001) Dimethyl sulfoxide suppresses NMDA- and AMPA-induced ion currents and calcium influx and protects against excitotoxic death in hippocampal neurons. Exp Neurol 170:180-188.

Lyden P, Wahlgren NG (2000) Mechanisms of action of neuroprotectants in stroke. J Stroke Cerebrovasc Dis 9:9-14.

Lythgoe MF, Thomas DL, Calamante F, Pell GS, King MD, Busza AL, Sotak CH, Williams SR, Ordidge RJ, Gadian DG (2000) Acute changes in MRI diffusion, perfusion, T1, and T2 in a rat model of oligemia produced by partial occlusion of the middle cerebral artery. Magn Reson Med 44:706-712.

Mabuchi T, Kitagawa K, Ohtsuki T, Kuwabara, Yagita Y, Yanagihara T, Hori M, Matsumoto K (2000) Contribution of microglia/macrophages to expansion of infarction and response of oligodendrocytes after focal cerebral ischemia in rats. Stroke 31:1735-1743.

Magiera Dunithan AJ, Cox LA, Long BW (1998) Detection of acute stroke with diffusion-weighted MRI. Radiol Technol 69:559-565.

Martin LJ, Al-Abdulla NA, Brambrink AM, Kirsch JR, Sieber FE, Portera-Cailliau C (1998) Neurodegeneration in excitotoxicity, global cerebral ischemia, and target deprivation: a perspective on the contributions of apoptosis and necrosis. Brain Res Bull 46:281-309.

Martiney JA, Cuff C, Litwak M, Berman J, Brosnan CF (1998) Cytokine-induced inflammation in the central nervous system revisited. Neurochem Res 23:349-359.

Matsumoto K, Lo EH, Pierce AR, Wei H, Garrido L, Kozlowski P (1995) Role of vasogenic edema and tissue cavitation in ischemic evolution on diffusion weighted imaging: comparison with multiparameter MR and immunohistochemistry. AJNR Am J Neuroradiol 16:1107-1115.

Matsuo Y, Onodera H, Shiga Y, Nakamura M, Ninomiya M, Kihara T, Kogure K (1994) Correlation between myeloperoxidase-quantified neutrophil accumulation and

ischemic brain injury in the rat. Effects of neutrophil depletion. Stroke 25:1469-1475.

Merten CL, Knitelius HO, Assheuer J, Bergmann-Kurz B, Hedde JP, Bewermeyer H (1999) MRI of acute cerebral infarcts: increased contrast enhancement with continuous infusion of gadolinium. Neuroradiology 41:242-248.

Minematsu K, Fisher M, Li L, Davis MA, Knapp AG, Cotter RE, McBurney RN, Sotak CH (1993) Effects of a novel NMDA antagonist on experimental stroke rapidly and quantitatively assessed by diffusion-weighted MRI. Neurology 43:397-403.

Minematsu K, Li L, Fisher M, Sotak CH, Davis MA, Fiandaca MS (1992) Diffusion-weighted magnetic resonance imaging: rapid and quantitative detection of focal brain ischemia. Neurology 42:235-240.

Mitchell DG (1999) MRI Principles. Philadelphia: W.B. Saunders.

Moseley M, Kucharczyk J (1995) Brain Ischemia. Diffusion in Brain Ischemia. In: Diffusion and Perfusion in Magnetic Resonance Imaging. Apllications to Functional MRI (Le Bihan D Ed), pp 159-168. New York: Raven Press.

Moseley ME, Mintorovitch J, Chileuitt L, Shimizu H, Kucharczyk J, Wendland MF, Weinstein PR (1990) Early detection of regional cerebral ischemia in cats: comparison of diffusion and T2 weighted MRI and spectroscopy. Magn Reson Med 14:330-346.

Neeman M, Freyer JP, Sillerud LO (1995) b Factor. In: Diffusion and Perfusion Magnetic Resonance Imaging: Applications to Functional MRI (Le Bihan D ed), pp 73-98. New York: Raven Press.

Nicholson C (1995) Diffusion of Ions and Macromolecules in the Brain. In: Diffusion and Perfusion Magnetic Resonance Imaging. Applications to Functional MRI (Le Bihan D ed), pp 127-131. New York: Raven Press.

Niendorf T, Dijkhuizen RM, Norris DG, van Lookeren Campagne M, Nicolay K (1996) Biexponential diffusion attenuation in various states of brain tissue: implications for diffusion-weighted imaging. Magn Reson Med 36:847-857.

Nogawa S, Zhang F, Ross ME, Iadecola C (1997) Cyclo-Oxygenase-2 gene expression in neurons contributes to ischemic brain damage. J Neurosci 17:2746-2755.

Pantoni L, Sarti C, Inzitari D (1998) Cytokines and cell adhesion molecules in cerebral ischemia. Experimental bases and therapeutic perspectives. Arterioscler Thromb Vasc Biol 18:503-513.

Park HK, Fernandez L, Dujovny M, Diaz FG (1999) Experimental animal models of traumatic brain injury: medical and biomechanical mechanism. Crit Rev Neurosurg 9:44-52.

Peters A, Palay SL, Webster Hd (1991) The Fine Structure of the Nervous System. New York: Oxford University Press.

Phillis JW, Estevez AY, O'Regan MH (1998) Protective effects of the free radical scavengers, dimethyl sulfoxide and ethanol, in cerebral ischemia in gerbils. Neurosci Lett 244:109-111.

Pierpaoli C, Righini A, Linfante I, Tao-Chung JH, Alger JR, Di Chiro G (1993) Histopathologic correlates of abnormal water diffusion in cerebral ischemia: diffusion weighted MR imaging and light and electron microscopic study. Radiology 189:439-448.

Poirier JL, Capek R, de Koninck Y (2000) Differential progression of dark neuron and fluoro-jade labelling in the rat hippocampus following pilocarpine-induced status epilepticus. Neuroscience 97:59-68.

Raivich G, Jones LL, werner H, Bluthmann H, Doetschmann T, Kreutzberg GW (1999) Molecular signals for glial activation: pro- and anti-inflammatory cytokines in the injured brain. Acta Neurochirica Suppl 73:21-30.

Reith W, Forsting M, Vogler H, Heiland S, Sartor K (1995) Early MR detection of experimentally induced cerebral ischemia using magnetic susceptibility contrast agents: comparison between gadopentetate dimeglumine and iron oxide particles. AJNR Am J Neuroradiol 16:53-60.

Roitt I, Brostoff J, Male D (1998) Cell cooperation in the antibody response. In: Immunology (Roitt I, Brostoff J, Male D Eds), pp 8.1-8.16New York: Mosby.

Rothlein R, Czajkowski M, O'Neill MM, Marlin SD, Mainolf E, Merluzzi VJ (1988) Induction of intercellular adhesion molecule 1 on primary and continuous cell lines by pro-inflammatory cytokines. J Immunol 141:1665-1669.

Rumpel H, Nedelcu J, Aguzzi A, Martin E (1997) Late glial swelling after acute cerebral hypoxia-ischemia in the neonatal rat: a combined magnetic resonance and histochemical study. Pediat Res 42:54-59.

Sato M, Chang E, Igarashi T, Noble LJ (2001) Neuronal injury and loss after traumatic brain injury: time course and regional variability. Brain Res 917:45-54.

Sattler R, Tymianski M (2002) Molecular mechanisms of calcium-dependent excitotoxicity. J Mol Med 78:3-13.

Schmued LC, Albertson C, Slikker W (1997) Fluoro-Jade: a novel fluorochrome for the sensitive and reliable histochemical localization of neuronal degeneration. Brain Res 751:37-46.

Schroeter M, Franke C, Stoll G, Hoehn M (2001) Dynamic changes of magnetic resonance imaging abnormalities in relation to inflammation and glial responses

after photothrombic cerebral infarction in the rat brain. Acta Neuropathol (Berl) 101:114-122.

Schroeter M, Jander S, Witte OW, Stoll G (1999) Heterogeneity of the microglial response in photochemically induced focal ischemia of the rat cerebral cortex. Neuroscience 89:1367-1377.

Seegers H, Grillon E, Trioullier Y, Vath A, Verna J-M, Blum D (2000) Nuclear factor kappa B activation in permanent intraluminal focal cerebral ischemia in the rat. Neurosci Lett 288:241-245.

Sen CK, Roy S, Packer L (1996) Involvement of intracellular Ca^{2+} in oxidant-induced NF-κB activation. FEBS Letters 385:58-62.

Shahrestanifar M, Fan X, Manning DR (1999) Lysophosphatidic acid activates NF-κB in fibroblasts. J Biol Chem 274:3828-3833.

Shimizu K, Veltkamp R, Busija DW (2000) Characteristics of induced spreading depression after transient focal ischemia in the rat. Brain Res 861:316-324.

Shimizu S, Simon RP, Graham SH (1997) Dimethylsufoxide (DMSO) treatment reduces infarction volume after permanent focal cerebral ischemia in rats. Neurosci Lett 239:125-127.

Siesjo BK (1992) Pathophysiology and treatment of focal cerebral ischemia. J Neurosurg 77:337-354.

Silver IA, Erecinska M (1990) Intracellular and extracellular changes of $[Ca^{2+}]$ in hypoxia and ischemia in rat brain in vivo. J Gen Physio 95:837-866.

Small DL, Morley P, Buchan AM (1999) Biology of ischemic cerebral cell death. Prog Cardiovasc Dis 42:185-207.

Sonn J, Mayevsky A (2000) Effects of brain oxygenation on metabolic, hemodynamic, ionic and electrical responses to spreading depression in the rat. Brain Res 882:212-216.

Sonnewald U, Westergaard N, Schousboe A (1997) Glutamate transport and metabolism in astrocytes. Glia 21:56-63.

Spigelman I, Obenaus A, Mazarati A, Wasterlain CG (1998) Intravenously administered cell-permeant calcium buffer decreases evoked synaptic potentials in rat dentate gyrus in vivo. Brain Res 810:269-273.

Spigelman I, Tymianski M, Wallace CM, Carlen PL, Velumian AA (1996) Modulation of hippocampal synaptic transmission by low concentrations of cell-permeant Ca^{2+} chelators: effects of Ca^{2+} affinity, chelator structure and binding kinetics. Neuroscience 75:559-572.

Stejskal EO, Tanner JE (1965) Spin diffusion measurements: spin echoes in the presence of a time-dependent field gradient. J Chem Phys 42:288-292.

Stephens PH, Cuello AC, Sofroniew MV, Pearson RCA, Tagari P (1985) Effect of unilateral decortication on choline acetyltransferase activity in the nucleus basalis and other areas of the rat brain. J Neurochem 45:1021-1026.

Stephenson D, Yin T, Smalstig EB, Hsu MA, Panetta J, Little S, Clemens J (2000) Transcription factor nuclear factor-kappa B is activated in neurons after focal cerebral ischemia. J Cereb Blood Flow Metab 20:592-603.

Stevens SL, Bao J, Hollis J, Lessov NS, Clark WM, Stenzel-Poore MP (2002) The use of flow cytometry to evaluate temporal changes in inflammatory cells following focal cerebral ischemia in mice. Brain Res 932:110-119.

Stoll G, Jander S (1999) The role of microglia and macrophages in the pathophysiology of the CNS. Prog Neurobiol 58:233-247.

Stoll G, Jander S, Schroeter M (1998) Inflammation and glial responses in ischemic brain lesions. Prog Neurobiol 56:149-171.

Sweeney MI, Yager JY, Walz W, Juurlink BHJ (1995) Cellular mechanisms involved in brain ischemia. Can J Physiol Pharmacol 73:1525-1535.

Sykova E (1997) The extracellular space in the CNS: its regulation, volume and geometry in normal and pathological neuronal function. Neuroscientist 3:28-41.

Sykova E, Chvatal A (1993) Extracellular ionic and volume changes: the role in glia-neuron interaction. J Chem Neuroanat 6:247-260.

Szafer A, Zhong J, Gore JC (1995) Theoretical model for water diffusion in tissues. Magn Reson Med 33:697-712.

Tansey FA, Farooq M, Cammer W (1991) Glutamine synthetase in oligodendrocytes and astrocytes: new biochemical and immunocytochemical evidence. J Neurochem 56:266-272.

Tatlisumak T, Carano RAD, Takano K, Meiler MR, Li F, Sotak CH, Arndts D, Pschorn U, Fisher M (2000) Broad-spectrum cation channel inhibition by LOE 908 MS reduces infarct volume in vivo and postmortem in focal cerebral ischemia in the rat. J Neurol Sci 178:107-113.

Tatlisumak T, Carano RAD, Takano K, Opgenorth TJ, Sotak CH, Fisher M (1998) A novel endothelin antagonist, A-127722, attenuates ischemic lesion size in rats with temporary middle cerebral artery occlusion. Stroke 29:850-858.

Touzani O, Boutin H, Chuquet J, Rothwell NJ (1999) Potential mechanisms of interleukin-1 involvement in cerebral ischemia. J Neuroimmunol 100:203-215.

Trushin SA, Pennigton KN, Algeciras-Schimnich A, Paya CV (1999) Protein kinase C and calcineurin synergize to activate IκB kinase and NF-κB in T lymphocytes. J Biol Chem 274:22923-22931.

Tymianski M (1995) Neuroprotection in vitro and in vivo by cell membrane-permeant Ca^{2+} chelators. Clin Exp Pharmacol Physiol 22:299-300.

Tymianski M (1996) Cytosolic calcium concentrations and cell death in vitro. Adv Neurol 71:85-105.

Tymianski M, Spigelman I, Zhang L, Carlen PL, Tator CH, Charlton MP, Wallace CM (1994) Mechanism of action and persistence of neuroprotection by cell-permeant Ca^{2+} chelators. J Cereb Blood Flow Metab 14:911-923.

Tymianski M, Tator CH (1996) Normal and abnormal calcium homeostasis in neurons: a basis for the pathophysiology of traumatic and ischemic central nervous system injury. Neurosurgery 38:1176-1195.

Ueda T, Yuh WTC, Taoka T (1999) Clinical application of perfusion and diffusion MR imaging in acute ischemic stroke. J Magn Reson Imaging 10:305-309.

van Bruggen N, Roberts TPL, Cremer JE (1994) The application of magnetic resonance imaging to the study of experimental cerebral ischemia. Cerebrovasc Brain Metab Rev 6:180-210.

van Everdingen KJ, van der Grond J, Kappell LJ, Ramos LMP, Malisza KL (1998) Diffusion weighted MRI in acute stroke. Stroke 29:1783-1790.

van Gelderen P, de Vleeschouwer MHM, DesPres D, Pekar J, van Zijl PCM, Moonen CTW (1994) Water diffusion and acute stroke. Magn Reson Med 31:154-163.

Virag L, Scott GS, Antal-Szalmas P, O'Connor M, Ohshima H, Szabo C (1999) Requirement of intracellular calcium mobilization for peroxynitrite-induced poly (ADP-ribose) synthetase activation and cytotoxicity. Mol Pharmacol 56:824-833.

Wahl F, Obrenovitch TP, Hardy AM, Plotkine M, Boulu R, Symon L (1994) Extracellular glutamate during focal cerebral ischemia in rats: time course and calcium dependency. J Neurochem 63:1003-1011.

Wallach D (1997) Cell death induction by TNF: a matter of self-control. Trends Biochem Sci 22:107-109.

Watson BD, Dietrich WD, Busto R, Wachtel MS, Ginsberg MD (1985) Induction of reproducible brain infarction by photochemically initiated thrombosis. Ann Neurol 17:497-504.

Woodroofe MN (1995) Cytokine production in the central nervous system. Neurology 45:S6-S10

Woodward P (2002) MRI for Technologists. San Francisco: McGraw-Hill.

Xing D, Papadakis NG, Huang CLH, Lee VM, Carpenter TA, Hall LD (1997) Optimized diffusion-weighted for measurement of apparent diffusion coefficient (ADC) in human brain. Magn Reson Med 15:771-784.

Yamasaki Y, Itoyama Y, Kogure K (1996) Involvement of cytokine production in pathogenesis of transient cerebral ischemic damage. Keio J Med 45:225-229.

Yenari MA, Palmer JT, Sun GH, de Crespigny A, Moseley ME, Steinberg GK (1996) Time-course and treatment response with SNX-111, an N-type calcium channel blocker, in a rodent model of focal ischemia using diffusion-weighted MRI. Brain Res 739:36-45.

Zabel.U., Henkel T, Silva MS, Baeuerle PA (1993) Nuclear uptake control of NF-kappa B by MAD-3, an I kappa B protein in the nucleus. EMBO J 12:201-211.

Zhang RL, Chopp M, Chen H, Garcia JH (1994) Temporal profile of ischemic tissue damage, neutrophil response, and vascular plugging following permanent and transient (2H) middle cerebral artery occlusion in the rat. J Neurol Sci 125:3-10.

Zilles K, Wree A (1995) Cortex: areal and laminar structure. In: The rat nervous system (Paxinos G ed), pp 649-685. Toronto: Academic Press.